metals

IMPACT FACTOR 2.695

CITESCORE 3.8

Review

A Review on Material Extrusion Additive Manufacturing of Metal and How It Compares with Metal Injection Moulding

Chanun Suwanpreecha and Anchalee Manonukul

MDPI

https://doi.org/10.3390/met12030429

metals

MDPI

Review

A Review on Material Extrusion Additive Manufacturing of Metal and How It Compares with Metal Injection Moulding

Chanun Suwanpreecha and Anchalee Manonukul *

National Metal and Materials Technology Center (MTEC), National Sciences and Technology Development Agency (NSTDA), 114 Thailand Science Park, Klong Luang, Pathumthani 12120, Thailand; chanun.suw@ncr.nstda.or.th

* Correspondence: anchalm@mtec.or.th

Abstract: Material extrusion additive manufacturing of metal (metal MEX), which is one of the 3D printing processes, has gained more interests because of its simplicity and economics. Metal MEX process is similar to the conventional metal injection moulding (MIM) process, consisting of feedstock preparation of metal powder and polymer binders, layer-by-layer 3D printing (metal MEX) or injection (MIM) to create green parts, debinding to remove the binders and sintering to create the consolidated metallic parts. Due to the recent rapid development of metal MEX, it is important to review current research work on this topic to further understand the critical process parameters and the related physical and mechanical properties of metal MEX parts relevant to further studies and real applications. In this review, the available literature is systematically summarised and concluded in terms of feedstock, printing, debinding and sintering. The processing-related physical and mechanical properties, i.e., solid loading vs. dimensional shrinkage maps, sintering temperature vs. relative sintered density maps, stress vs. elongation maps for the three main alloys (316L stainless steel, 17-4PH stainless steel and Ti-6Al-4V), are also discussed and compared with well-established MIM properties and MIM international standards to assess the current stage of metal MEX development.

Keywords: material extrusion; 3D printing; fused filament fabrication; metal injection moulding; debinding; sintering; mechanical property

Citation: Suwanpreecha, C.; Manonukul, A. A Review on Material Extrusion Additive Manufacturing of Metal and How It Compares with Metal Injection Moulding. *Metals* **2022**, *12*, 429. https://doi.org/10.3390/met12030429

Academic Editor: Matteo Benedetti

Received: 6 February 2022
Accepted: 25 February 2022
Published: 28 February 2022

1. Introduction

From the ISO/ASTM 52900, additive manufacturing (AM), usually known as 3D-printing, is a process of joining materials to make parts from 3D model data, usually layer by layer, as opposed to subtractive manufacturing and formative manufacturing methodologies [1]. This process has become increasingly popular for various material fabrications, such as ceramic, polymer and metal [2–5]. Many metal AM processes, such as powder bed fusion (PBF), direct energy deposition (DED) and materials extrusion (MEX) can successfully fabricate various metals, e.g., stainless steel [6–9], titanium alloys [10–13], nickel alloys [14–18], cobalt [19,20] and aluminium alloys [21–25]. AM can also provide a high degree of freedom, lightweight design with almost unlimited shape, complexity and a varied range of sizes depending on the printing process [26]. In addition, the AM parts are not only limited to prototyping, but can be applied in various technologies, including modelling, pattern-making, tool-making and end-use parts productions with very high growth rates [27]. Hence, AM parts can be served in many industries, e.g., biomedical, aerospace and energy applications [3,28]. Among the several techniques of metal AM, metal MEX utilises low-cost equipment with simplicity and safety, as neither loose metal powder nor a high-power source is required when compared to other common metal AM processes, i.e., laser powder bed fusion (LPBF) and electron beam powder bed fusion (EPBF) [9,29]. During the last decade, this metal MEX process has attracted more attention due to the

as-mentioned advantages and the familiarities with conventional polymer 3D printing, which is the metal-fused filament fabrication process (FFF), usually called fused deposition modelling (FDM). Figure 1 shows the number of publications relating to metal MEX per year and the cumulative number. From 1996 to 2015, there are very few publications per year. However, the number has significantly increased since 2015. It is noted that publications were searched mainly from several databases, e.g., Web of Science, Scopus and Google Scholar, using several searching keywords, e.g., "metal material extrusion", "metal fused deposition modelling", "metal fused filament fabrication" and "Ultrafuse 316L", including the references of related articles. The three prior review articles focusing on metal MEX [4,5,30] provide a good overall review of the subject but do not address the achievable mechanical properties in detail.

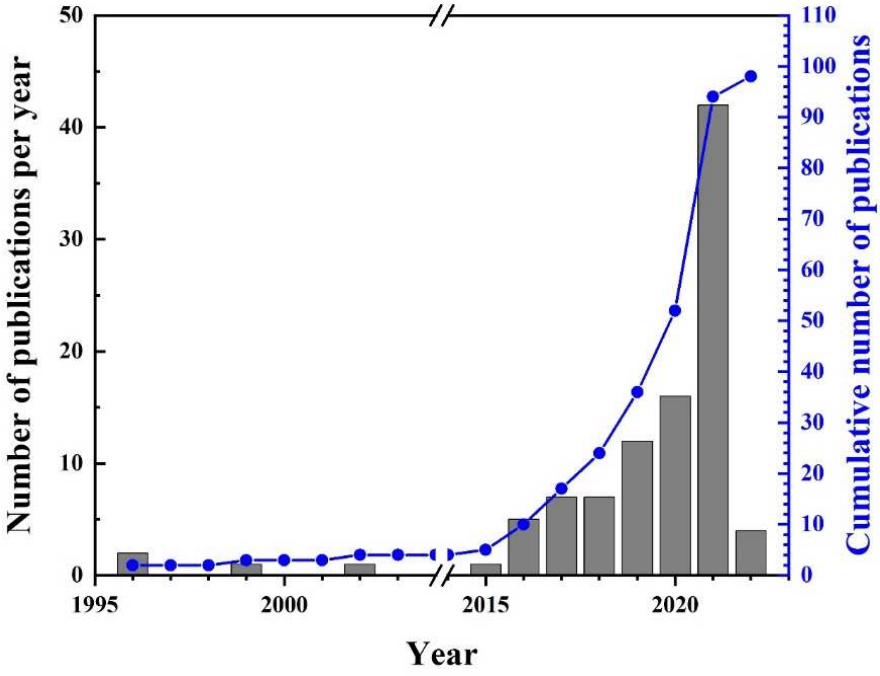

Figure 1. Number of publications relating to the metal MEX from 1996 to February 2022. Data from [4,5,8,9,29–123].

The nature of metal MEX is very similar to the conventional metal injection moulding (MIM) [124,125]. The overall MIM and metal MEX processing steps are presented in Figure 2a,b,d,e and Figure 2a,c,d,e, respectively. The MIM process starts with the mixing of sinterable metal powder with suitable polymeric binders and then granulating the metal-binder mixture into feedstock Figure 2a. The feedstock is subsequently injected into a mould to create the injected part, commonly called a "green part" (Figure 2b). The polymeric binders are then removed by solvent (optional) and thermal debinding (Figure 2d) before the debound parts are sintered in a controlled atmosphere, e.g., H_2, N_2, Ar or vacuum atmosphere, to densify the parts (Figure 2e). During sintering, necks are formed to bond between adjacent powder particles, consolidation takes place and voids are closed. This causes shrinkage of the sintered part, which in theory should be uniform. However, in practice, the uniformity of shrinkage depends on several factors, e.g., the homogeneity of feedstock and the resultant green parts, geometry, gravity and friction between the parts and sintering tray. Typical MIM shrinkage lies within the range of 12–20% [125–127]. Hence, the mould cavity needs to be oversized to compensate for the shrinkage. After sintering, the density of the MIMed specimen can reach up to 99% of the theoretical density. Hot isostatic pressing (HIP) can be applied, if high mechanical property and density are required. For the metal MEX, instead of forming the green part by the injection moulding process, it is printed layer by layer (the process in Figure 2b

is replaced by that in Figure 2c) with various forms of feedstock, i.e., granule, bar and filament, depending on the printer. After printing, the subsequent debinding and sintering steps (Figure 2d,e) may be slightly different from the MIM process due to the differences in compositions of binders and the metal powder fraction (usually named "solid loading"), metal powder size and its distribution. The shrinkage of the sintered metal MEX part is generally higher than for MIM parts because the metal MEX feedstock usually has higher binder content (lower solid loading) than MIM so that the metal MEX feedstock is printable and can be easily handled. Therefore, dimensions of the CAD model need to be carefully compensated to acquire the required dimension after sintering. The sintered density and mechanical properties of the metal MEX part are theoretically lower than those of MIM due to the voids between deposited paths generated during printing [8]. Thereby, the print strategy, which can generate not only such voids but also deflection and incomplete weld in polymer 3D-print parts [128–130], needs to be carefully controlled for metal MEX before progressing to the debinding and sintering.

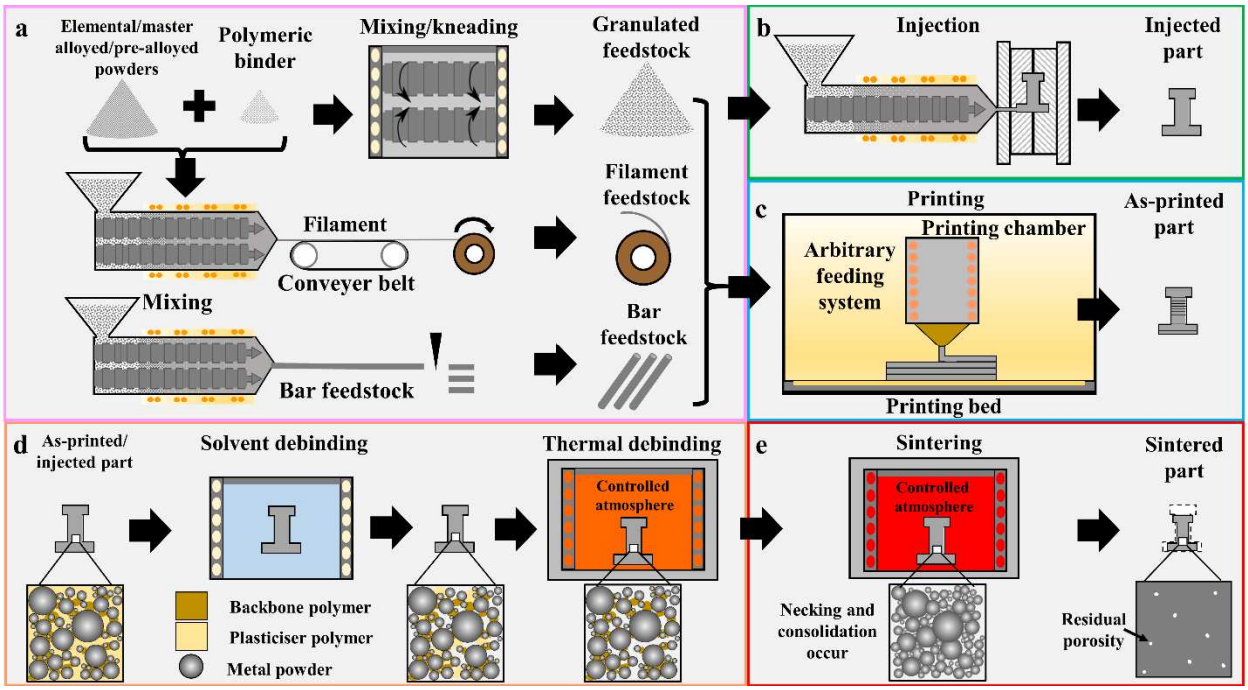

Figure 2. Comparison of material extrusion additive manufacturing of metal (**a**,**c**,**d**,**e**) and metal injection moulding (**a**,**b**,**d**,**e**).

The objectives of this review are to systematically summarise and present the current status and available data on metal MEX, including feedstock, printing, debinding, sintering and physical and mechanical properties. The available metal MEX data are compared to the conventional MIM process and MIM international standards. The topics of this review are presented in five sections, which are Section 1—Introduction; Section 2—Material extrusion additive manufacturing of metal, which reports on types of metal MEX and process variables, i.e., printer equipment, alloy and powder, feedstock, printing, debinding and sintering; Section 3—Effects of processing parameters on physical and mechanical properties of metal MEX parts and comparison with MIM parts and MIM standards; Section 4—Secondary processes, which can improve the properties of metal MEX parts; Section 5—Current, prospective applications and future direction of metal MEX development and Section 6—Summary. In sub-sections of Section 2, MIM will be introduced first and then metal MEX will be discussed because MIM is better well established. In Section 3, the MIM international standards are used because there is currently no international standard for metal MEX. The MIM standards are the Metal Powder Industries

Federation (MPIF) Standard 35 Metal Injection Moulding Materials for stainless steels and Japan Powder Metallurgy Association (JPMA) Standard Metal Injection Moulding Materials for Ti-6Al-4V. The information from this review will not only be useful for researchers, who work in the fields of 3D printing and powder metallurgy, metal MEX and MIM, but also will promote the development of the metal MEX to be widely commercialised.

2. Material Extrusion Additive Manufacturing of Metal (Metal MEX)

In metal MEX, the feedstock composing of metal powder and polymeric binders is heated until the filament is softened and can be extruded through a printing nozzle. The printed material is then deposited on the printing bed, which is heated to increase adhesion between the printed parts and the printing bed so that the 3D part is created layer-by-layer following the CAD model [131]. This metal MEX process can also fabricate multi-material 3D parts, when a printer has more than one printing head or feeding system. Depending on the feeding system of the printer, the metal MEX process can be classified into three types, as presented in Figure 3, which are (a) screw-based, (b) plunger-based and (c) filament-based types [132]. After printing, the as-printed parts require to be debound and sintered in a similar manner to those in the MIM processing steps, as presented in Figure 2d,e.

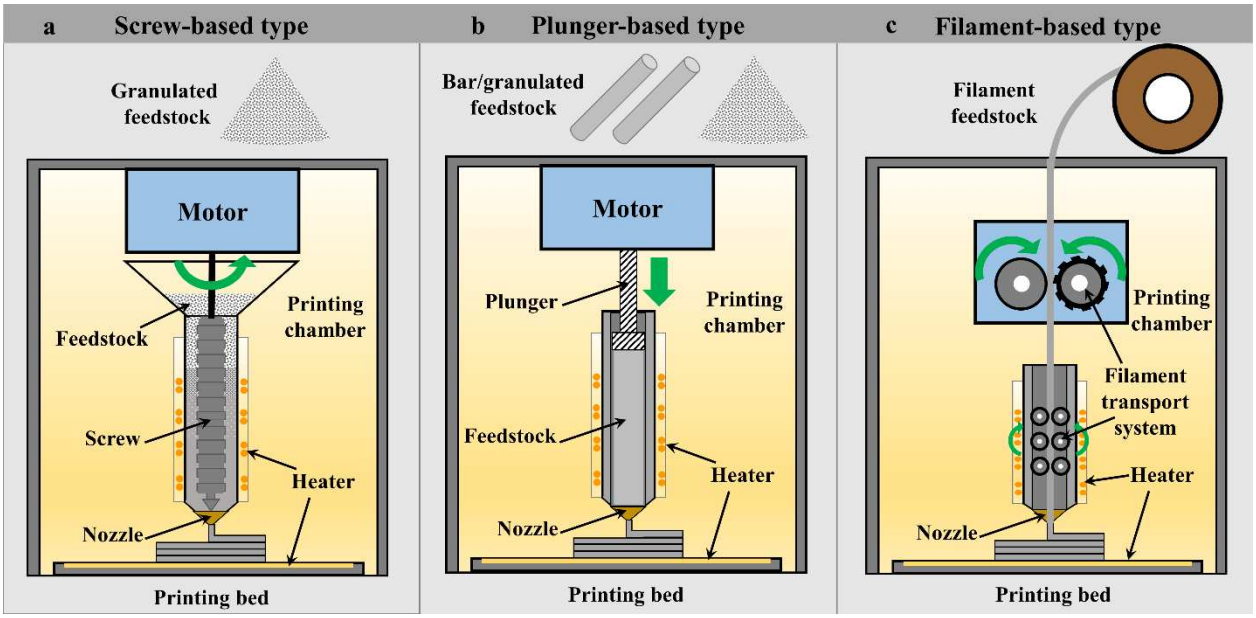

Figure 3. Types of material extrusion additive manufacturing classified by feeding system: (**a**) screw-based, (**b**) plunger-based and (**c**) filament-based types.

- **Screw-based MEX (SB)**

High quality metal filament and bar feedstocks are still very limited in alloy selection. Hence, screw-based MEX is currently the most versatile material extrusion system in term of material selection. Screw-based MEX uses the granulated feedstock in a similar form as MIM, hence all alloys for MIM feedstocks are applicable. The feedstock will be transported by screw rotation [132] and simultaneously heated by heating elements to a temperature above the glass transition temperature of the polymer binder. The softened material will be deposited through the nozzle in a pattern that follows the CAD design, as presented in Figure 3a. The advantages of this type over the latter two processes, which are plunger- (Figure 3b) and filament- (Figure 3c) based types are high productivity due to a continuous filling system and no requirement for an additional processing step for bar or filament preparation. In addition, high solid loading equivalent to that employed in MIM can be used. This process provides the best available feedstock filling system, which can continuously feed without interruption during printing, as the feedstock in the

system is replenished. This results in printing time reduction, as neither printing stoppage during feedstock replenishment nor feedstock re-heating to the printing temperature is mandatory. There is also no need for additional equipment for bar or filament preparation and know-how to produce and handle feedstocks, especially filament feedstock, which is commonly brittle and difficult to handle. The size of the granulated feedstock needs to be controlled (<5 mm) to obtain stability during printing and reduce printing defects generated by air entrapment [133]. As reported by Singh et al. [85], the granule feedstock, sized from 3 to 5 mm, can provide relative sintered density up to 94% after sintering. Likewise, Lieberwirth et al. [41] reported that a granule size of 3 mm could be readily printed, yielding good appearance. Too large granulated feedstock may not be evenly and properly softened in the feeding system. Too small granulated feedstock may cause blocking at the hopper. Any printed mono-material green parts with defects or mistakes can be easily re-used by crushing and sieving before feeding back into the printer hopper, similar to the re-use of MIM injected parts with defects and all runner systems [134]. The other two types of printing systems need an additional bar or filament preparation step. The stabilisation of the screw system is still challenging to fabricate the 3D part, as it is difficult to control the flow rate of the material to be constant due to the trapped air inside the softened material. Moreover, the strength and stability of the printing system are also required during printing due to the high viscosity of the feedstock. The well-known commercially available screw-based MEX systems are proposed by AIM3D GmbH with a "ceramic extrusion modelling" system (CEM) [135] and Pollen AM, Ltd. With a "pallet additive manufacturing" system (PAM) [136], in which multi-material parts, such as both ceramic and metal, can be fabricated by using general powder injection moulding feedstocks. Figure 4a shows the AIM3D printer and the schematic representing the printing, while Figure 4b shows the feedstock and the microstructure of the feedstock utilised for the AIM3D printer. Recently, pallet extrusion system has been introduced by Direct3D, which supplies both a screw-based printer and only a screw-based print head that can be applied with a suitable 3D printer [137]. In addition, most MIM manufacturers will prefer to use their current MIM feedstock so that they can use their current debinding and sintering systems. Hence, the implementation of metal MEX will be easier, smoother, faster and more economical for MIM manufacturers.

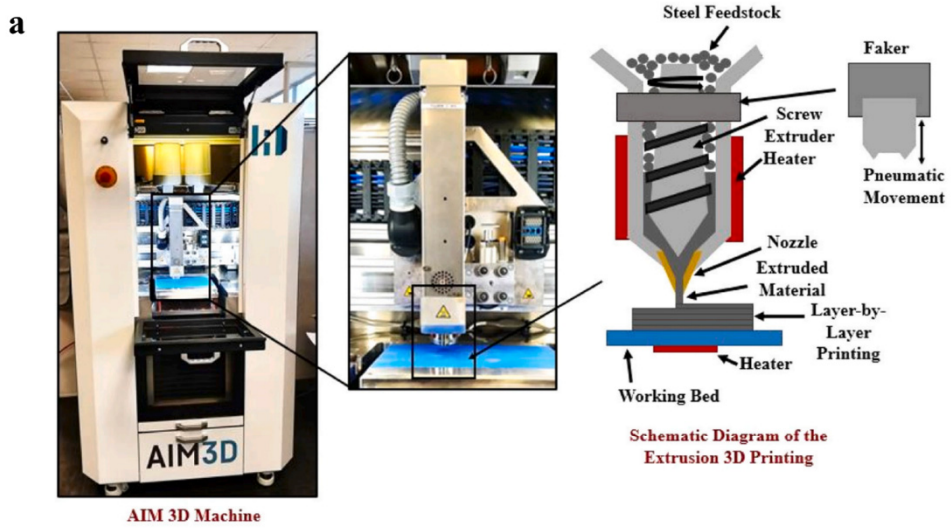

Figure 4. *Cont.*

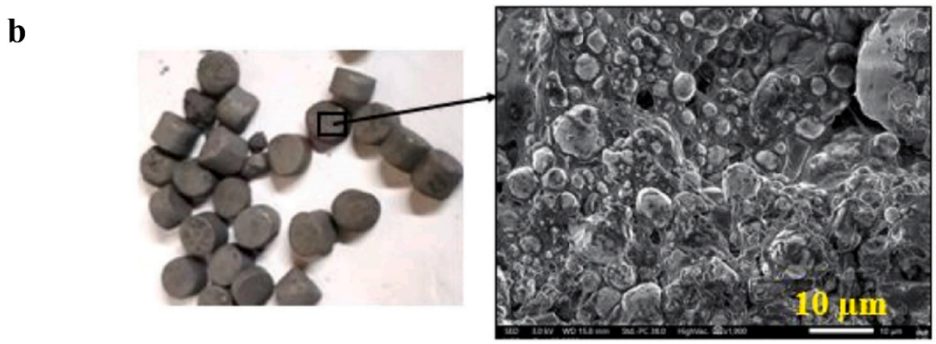

Figure 4. (**a**) AIM3D printer and the schematic representing the printing and (**b**) low and high magnification of the 17-4PH stainless steel granulated feedstock utilised for the printer (adapted from [92]).

- **Plunger-based MEX (PB)**

The plunger-based MEX utilises bar or granulated feedstock to feed to the nozzle of the plunger system. Desktop Metal, Inc. [138] proposes the plunger-based system using circular-bar feedstock, called "bound deposition modelling" (BMD), in which the bar feedstock will be fed by a cartridge into a heated sleeve. The feedstock is then pushed through the nozzle for layer-by-layer printing by the plunger following the CAD design as presented in Figure 3b. One of the main advantages of this system is the high material handling ability, which is significantly easier than the filament feedstock. Besides, the solid loading of the bar feedstock can be higher than the filament-based printers and comparable to the MIM feedstock. However, one of the main disadvantages of the plunger-based system when compared to the screw-based one is the additional step of bar feedstock preparation. The bar feedstock can be prepared by extruding the mixture of metal powder and polymer binders and cut to size, as shown in Figure 2a. Furthermore, print discontinuity occurs when the feedstock is required to be replenished. To overcome this disadvantage, Giberti et al. proposed an in-house developed machine, as shown in Figure 5a, combining a screw-based to feed the MIM feedstock and plunger system to push the feedstock through the nozzle [36]. However, at the end of the plunger stroke, the plunger still requires reversing to receive the softened feedstock from the screw-based plasticiser. Hence, the discontinuity is minimised but remained. As the injection unit is stationary, the deposited path will be printed on the printing bed of a 5-axes parallel kinematics machine (PKM). Hence, parts can be printed with minimal support materials. In 2020, Waalkes et al. proposed an in-house plunger-based printer, as presented in Figure 5b, which can fabricate the 3D part of Ti-6Al-4V using commercial MIM feedstock [61]. This in-house system successfully fabricates the as-printed parts with a good appearance and high stability. Moreover, the production cost of the machine is claimed to be close to the open polymer filament-based systems (5–10 k€) [61]. These in-house developed plunger-based printers provide the ability to use MIM feedstock. This increases the flexibility in material selection. In addition, there is no need for further feedstock preparation into filament form.

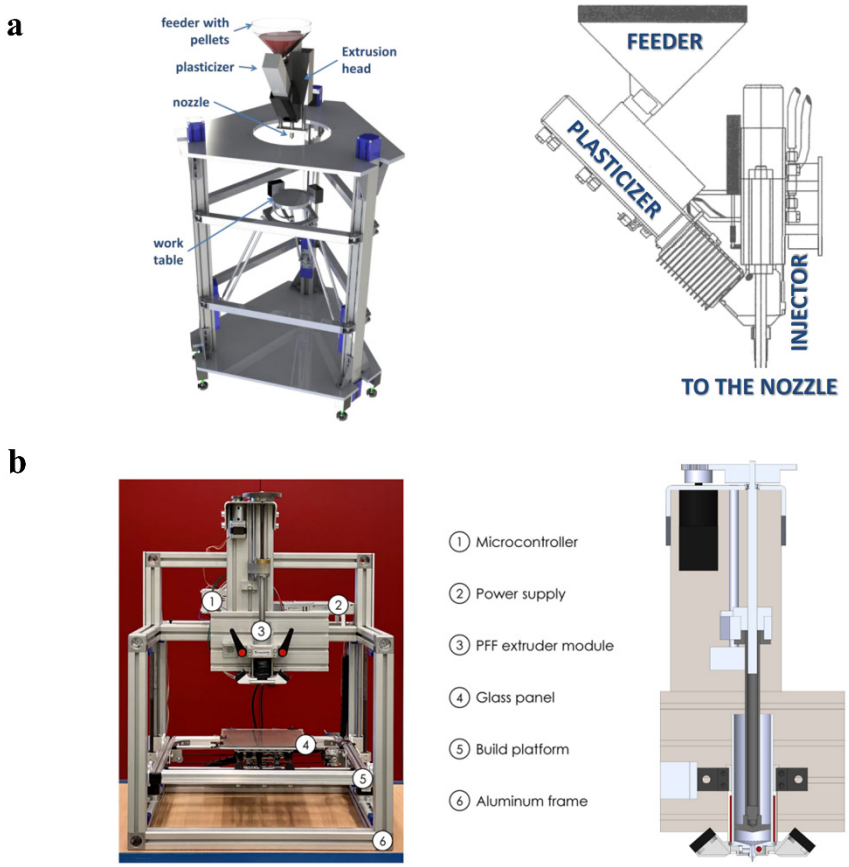

Figure 5. (**a**) In-house developed machine and their components with the extrusion unit combining a screw-based (plasticiser) to feed the feedstock and plunger system to inject the feedstock through the nozzle (adapted from [36]) and (**b**) in-house developed plunger-based printer and their components with the schematic of the extruder unit (Reprinted with permission from [61]. Copyright 2020, Additive Manufacturing, Elsevier).

- **Filament-based MEX (FB)**

Filament-based type is the most popularly and widely used metal MEX process. It is known by many terms, such as "fused deposition modelling" (FDM), first developed by Stratasys, Ltd. (Eden Prairie, MN, USA and Rehovot, Israel) for polymer [139]; "fused filament fabrication" (FFF) or "atomic diffusion additive manufacturing" (ADAM) proposed by Markforged, Inc., Watertown, MA, USA [140]. At the beginning, this process was usually used for rapid prototyping; however, it can currently be used for tooling and end-user part fabrication [50,140,141]. The filament of metal MEX composed of the metal powder and polymeric binder is fed by the filament transport system to the heating element and heated nozzle so that the filament will be softened and extruded to the printing bed layer-by-layer following the CAD design as illustrated in Figure 3c. The advantages of this filament-based process are safety, simplicity and familiarity of the process, and its low-cost equipment because the general desktop polymer 3D printer is used with the metal MEX filament. The high volume fraction of metal in the filament results in a high wear rate of the printing nozzle; hence, a special ruby or hardened steel nozzle should be utilised to produce a stable flow of the filament, prolong the nozzle life [142] and reduce contamination. The main disadvantage of this process is the need for filament production, which requires single/twin screws or plunger extrusion equipment for filament fabrication [34,52], plus special know-how, e.g., the selection of appropriate binder types, suitable mixing procedure and the filament fabrication technique [31]. The filament properties are very important to the final shape, size, dimension and properties in both as-printed and as-sintered stages.

Appropriate binders must be selected to provide the desired properties in the filament. The filament should have high strength and stiffness so that the filament can be driven by the roller or gear without breaking and bulking [31,143,144]. The high bonding strength of the metal powder and binders of the filament can provide strong weldability between deposit paths. In addition, the filament should have high flexural strength and stiffness so that the filament can be spooled and handled with ease [31]. The filament will be brittle if too-high solid loading is used [145]. Very careful handling of the filament is needed with an extra heater to reduce the brittleness of the filament and to reset the memory shape [56,64,146]. The filament must have no porosity, shape consistency and uniform distribution of the metal powder, including as high as possible of solid loading to minimise shrinkage [94]. The above factors directly influence the printing, debinding and sintering processes, which can be prone to generate many defects. High quality sintered parts can be achieved if these factors and the processes are correctly controlled. Examples of commercially available filaments are Ultrafuse 316L® by BASF SE [147], Filamet® by Virtual foundry [146] and 316L metal filament by Anycubic [148], which provide high-quality metal filaments, together with the suggested suitable range of processing parameters. The cross section of commercially available filament by BASF (Figure 6a), Virtual foundry (Figure 6b), including the filament specially developed for MetalX by Markforded, Inc. (Figure 6b) shows high fraction of the metal powder. It is noted that the Ultrafuse 316L filament uses polymer skin (Figure 6a) to case the filament to increase the flexibility of the filament [4], while the Filamet and Anycubic filament use binder with high flexibility and lower solid loading [48,146].

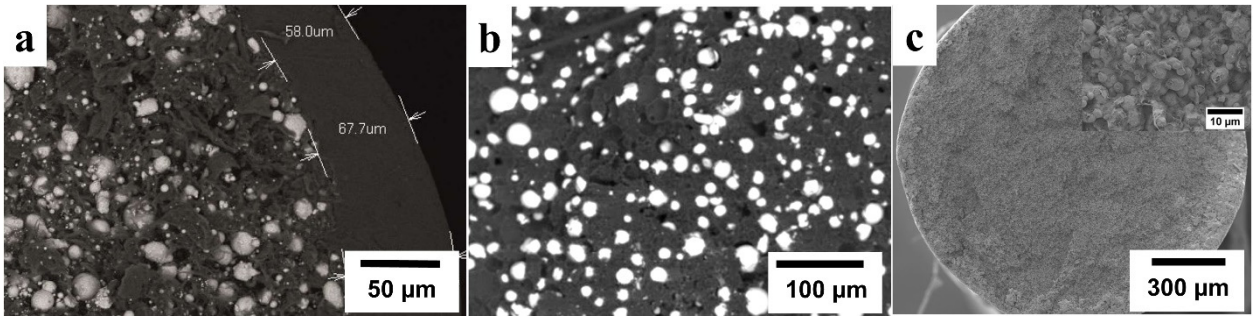

Figure 6. Cross-sectional view of the commercial filaments—(**a**) Ultrafuse by BASF (adapted from [4]), showing polymer skin surrounding mixing of polymer and metal powder, (**b**) 316L metal filament by Virtual foundry (adapted from [72]) and (**c**) 17-4PH stainless steel filament for MetalX system by Markforged, Inc. (Reprinted with permission from ref. [8]. Copyright 2021, Metallurgical and Materials Transactions A, Springer).

2.1. Printer

As previously mentioned, the metal MEX process can be classified into three types based on feeding systems, which are screw-, plunger- and filament-based. The available information on printers that have been utilised to fabricate metal MEX parts is reported in Table 1. There are few studies using the screw- and plunger-based printer systems. Some in-house built printers have been used both types of printer systems, even though there are commercially available printers, e.g., ExAM 255 printer by AIM3D (screw-based printer) and Desktop Metal Studio+ system (plunger-based printer). From Table 1, it is worth reinforcing that the filament-based system is the most popular type with various printer models being utilised for this system. These filament-based printers can be classified into three groups, which are (1) in-house built printers, (2) general polymer FDM printers and (3) special purposed and closed metal printers. The general polymer FDM printers are the most popular, as they are readily available in the workplace. Both commercially available and self-prepared metal filaments have been used for general polymer FDM and in-house built printers. A few studies [42,47,65] have used a special purposed metal printer, which is closed, more expensive but providing excellent and consistent printing quality.

Table 1. 3D printers classified by feeding system and printer model as reported in the literature.

Type of Printer	Printer Model	Ref.
Screw-based	1. In-house built printers	[41,132]
	2. ExAM 255 printer	[50,84,85,92]
Plunger-based	1. In-house built printers	[36,61,68,87,109,113–121]
	2. Special purposed and closed metal printer	
	• Desktop Metal Studio+ system	[62,108]
Filament-based	1. General polymer FDM printers	
	• 3D Modeler™	[32]
	• Apium P155	[45]
	• Apium P220	[97]
	• Axiom Dual, Airwolf	[100]
	• Crane Quad 3D machine	[72]
	• Duplicator i3 v2 FFF	[38,43,44,49]
	• Flashforge Dreamer	[9]
	• Funmat HT	[53]
	• German RepRap X500	[98]
	• German RepRap X1000	[90]
	• HAGE 3Dp-A2	[37,40]
	• Hephestos 2	[106]
	• L-DEVO M2030TP	[56,64]
	• MakerBot Replicator 2	[82]
	• Modified Hage 3D-72L	[35]
	• PrintBox3D	[71]
	• Prusa i3 Mk2	[52,102]
	• Prusa i3 Mk3	[48,54,83,86]
	• Prusa i3 Mk3s	[93]
	• Prusa Steel Black Edition Mark II	[96]
	• Pulse 3D from MatterHackers	[59,60,77–79,88,95]
	• Renkforce 1000 printer	[63]
	• Raised 3D pro2	[99]
	• TAZ6	[70,107]
	• Ultimaker 2	[29,46,51,89]
	• Ultimaker 3	[66,91,94]
	• Ultimaker S5	[73,99,101]
	• WANHAO Duplicator 4S	[105]
	• Zmorph 2S	[75]
	• Zortrax M200	[80]
	2. Special purposed and close metal printer	
	• Markforged MetalX	[8,42,47,58,65,67,69,110]
	• CoLiDo metal 3D printer	[57]

2.2. Feedstock

In this subsection, the feedstock of metal MEX will be discussed in terms of metal powder and binder as raw materials. The details of the MIM feedstock will be comparatively discussed to provide insight and understanding of the similarities and differences between the two processes.

As metal MEX is developed based on the principle of MIM, the range of available materials for metal MEX is rather similar to MIM. The materials that are usually fabricated by the MIM process are the sinterable materials, e.g., stainless steel, copper, titanium and its alloys and nickel-base superalloys [149]. Similarly, the main materials utilised in the metal MEX process are stainless steel and titanium alloys, as presented in Figure 7. The utilisation of the materials that have been fabricated by metal MEX can be ranked from the highest to lowest as 316L stainless steel (41.57%), 17-4PH stainless steel (or AISI 630, 17.98%), Ti-6Al-4V (13.48%), Cu (12.36%), WC-Co (4.49%), bronze (2.25%) and high-C iron, H13 tool steel, M2 high speed steel, AZ91 magnesium alloys, CP-Ti, Ni-Cu and Inconel 625 (1.12% each), respectively. For 316L stainless steel, more than one-third of the studies used the commercial 316L filament

feedstock from BASF SE, namely as Ultrafuse 316L (UF-316L). It is noted that at the time of writing, the 17-4PH stainless steel filament by BASF [150] has just been launched and there is still no available study. The availability of commercial and high-quality metal filament that can be printed using a general polymer FDM printer, debound and sintered using available MIM equipment, can accelerate the acceptant and utilisation of metal MEX. Interestingly, although the AZ91 Mg alloy (recognized as a material that is difficult to sinter) can be fabricated by metal MEX [87], its mechanical properties still need to be improved by solving the problem of magnesium oxide formation, which prevents proper sintering.

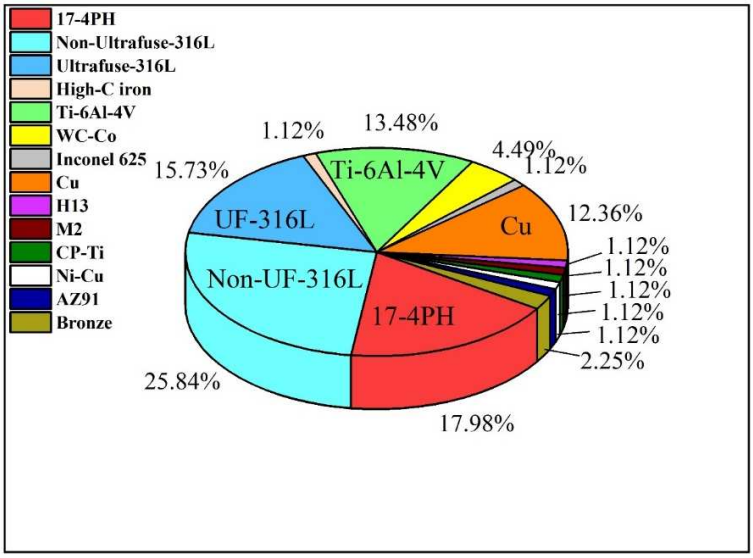

Figure 7. Alloys utilised to fabricate 3D parts by material extrusion additive manufacturing processes (UF-316L is Ultrafuse-316L and Non-UF-316L is the 316L studies that are fabricated using other filaments). Data from [8,9,29,31,32,34–46,48–53,56,57,59,61,63–68,70,72–76,78,79,81–83,85–102,104–116,119–123].

The raw material utilised in the metal MEX is in the form of pre-alloyed metal powders. There is no study reporting the utilisation of more economical elemental, master or/and HDH-Ti powders having an irregular particle shape, which are commonly employed in the MIM process [151–156]. However, these lower cost powders are likely to be investigated in the future to reduce the feedstock cost, especially for the screw-based and plunger-based type metal MEX for which MIM feedstock can be applied. For metal MEX, the preferable characteristics of powder are having a spherical shape, fine size and suitable size distribution similar to that of MIM [40,149]. These characteristics not only provide high printability but also enhance part density after sintering [78]. The high solid loading can be achieved with fine powder [105]. Besides, the use of fine powder sizes can provide thinner layer thickness; thus, higher surface quality and smaller features can be achieved. The powder characteristics utilised in MIM and metal MEX are presented in Tables 2 and 3, respectively. The powder sizes used as raw materials in metal MEX tend to be smaller than those for MIM. The suitable range of powder size for MIM is less than 20 μm for most stainless steels and less than 45 μm for titanium alloys because of the powder cost. Earlier studies of stainless steel MIM used the mean powder size (D_{50}) of around 10 μm [134,157–161]. Because of the advancement in powder production, smaller sized powders, especially for stainless steel, are available at similar cost to earlier larger powder sizes for the MIM industry. This is also beneficial for metal MEX. Smaller stainless steel powders will enhance densification especially for metal MEX, where the packing pressure is not as high as MIM.

The binder is one of the critical components that determine the quality of MIM parts [4,149,162]. The binder in MIM processing has multiple components, consisting of (1) plasticiser, (2) backbone polymer and (3) additives. The plasticiser is a low molecular weight polymer and is the main component with generally 50 to 90 vol.% in the binder

system. Paraffin and carnauba wax for wax-based or polyethylene glycol for water-soluble based are commonly used as presented in Table 2. The role of the plasticiser is to provide strength, wetability and to increase the fluidity of the feedstock so that the mould cavity can be completely filled. The backbone polymer is a higher molecular weight polymer with usually up to 50 vol.% in the binder system. Several grades of polymer can be utilised, as presented in Table 2, such as PA [158], PP [159], PE [161] and EVA [163,164]. The role of the backbone polymer is to provide the strength and to maintain the shape of parts after debinding before sintering. The additives (0 to 10 vol.% in the binder system) consist of surfactant and lubricant to modify the properties of the feedstock [149,165]. As presented in Table 2, stearic acid (SA) is the most commonly used. The type and fraction of the binders can also be varied depending on the required properties. The acrylic resin and cyclohexyl methacrylate (CHMA) [159] or Atactic Polypropylene (APP) polymers [163] can be used as a part of the binder. The desirable properties of the binder are having a low softening temperature, rapid solidification, good adhesion with powder, non-reactive with the metal powder, low viscosity at the moulding temperature, easy to be debound, having high strength and stiffness at room temperature and, last but not least, safe and environmentally acceptable [149,166,167].

There is very limited information regarding the grade of the polymer and the exact percentage of binder for metal MEX, as summarised in Table 3. This is understandable, as it is one of the most confidential pieces of information, similar to MIM binders or feedstock (Table 2). Most metal MEX binders are based on multiple components of polymer, similar to MIM binders. Considering the screw-and plunger-based metal MEX, the binder requirement is not as demanding as that for the filament-based type, as the granulated MIM feedstock, which has already been fully developed, can be successfully used [36,41,61,68,84,85,87]. However, the filament feedstock requires high flexibility so that it can be easily spooled, handled and printed. To achieve this characteristic, the binder must be highly elastic, such as the thermoplastic elastomer, TPE, which is usually employed in the in-house built filament feedstock [31,32,39,50,52,96,102,106], as presented in Table 3. The usage of high flexibility polymer as a part of the binder system, such as PA [29], PLA [51,89] and PO [37,96,102,168] can also be helpful. Otherwise, special features, such as a heating chamber, are required to reduce the brittleness of the filament during feeding [56,64]. For the well-known commercial filament; Ultrafuse 316L, the high flexibility of the skin case is utilised to enhance the filament flexibility [4]. Moreover, for the metal MEX feedstock, a tackifier is also used to enhance the adhesion with the previous layers and the flexibility [31,32,168]. The desirable properties of the metal MEX binder are rather similar to MIM. However, low viscosity is not as important as that of MIM, as it uses printing instead of injection. Furthermore, high strength, stillness and flexibility are mandatory to the metal MEX, especially for the filament-based type [4]. Even though the binder system is rather confidential, Wagner et al. has developed and initiated the binder system with two types of soluble polymers. The developed binder system can be easily modified to achieve the required physical and mechanical properties [106].

Although general filament feedstock utilised multi-component material, Sadaf et al. have successfully used a single component binder system (LDPE) to fabricate 316L stainless steel with good surface finish and density [75]. This is possible because of the presence of some intrinsic porosity associated with metal MEX acting as a "relief valve" for the release of volatile products from thermal degradation of the binder [75]. However, the elongation to failure is only about 9%, which is relatively low for sintered 316L stainless steel. Further discussion about the binders will be in the next sections for printing and debinding.

Table 2. Selected MIM information categorised by alloys and used for comparison in this study (ND is no detail; SD is solvent debinding; TD is thermal debinding, MPIF35 is Metal Powder Industries Federation Standard 35 Metal Injection Moulding Materials; JPMA is Japan Powder Metallurgy Association Standard Metal Injection Moulding Materials; * typical values).

Alloys	Powder Characteristics	Solid Loading (Vol.%)	Binder Detail	Debinding Process	Sintering Process	Shrinkage (%)	Relative Density (%)	UTS and % El	Ref.
17-4PH	- Water atomised (W), 10.3 μm - Gas atomised (G), 12 μm	93 wt.%	PW, SA, PE	- SD in heptane at 45 °C for 8 h - TD in H_2 at 500 °C for 2 h	- Pre-sintering at 1000 °C for 15 min - Sintering in partial pressure of Ar at 1350 °C for 2 h	ND	97 98	$W_{as\text{-}sintered}$ = 1000 MPa, 8.8% W_{900} = 1280 MPa, 8% W_{1100} = 1100 MPa, 11.5% $G_{as\text{-}sintered}$ = 1050 MPa, 8% G_{900} = 1300 MPa, 10% G_{1100} = 1080 MPa, 14%	[157]
17-4PH	Water-atomised powder D_{50} = 9.77 μm	60	PA-based, Mould Research, Co., Ltd., Japan	- Only TD	ND	15.7	97.5	896 MPa, 9.9%	[158]
17-4PH	Water-atomised powder D_{50} = 9.77 μm	ND	ND	- Only TD	- Sintering in Ar at 1325 °C for 2 h	13.03–15.64	98.8–99	900 MPa, 6%	[134]
17-4PH (MPIF 35)	-	-	-	-	-	12–20 (* 15–18)	96.7	790 MPa, 4% (* 900 MPa, 6%)	[169]
17-4PH Heat treat 900 °F (MPIF 35)	-	-	-	-	-	12–20 (* 15–18)	96.7	1070 MPa, 4% (* 1190 MPa, 6%)	[169]
316L	Irregular powder, D_{50} = 10.21 μm	93wt. (62 vol.%)	LDPE, HDPE, PW, SA	- SD in heptane at 60 °C for 6 h - TD in Ar at 600 °C for 1 h	- Pre-sintering at 1050 °C - Sintering in vacuum 1380 °C for 3 h	14.84–19.43	95.4–97.2	ND	[159]
316L	GA powder (80% < 22 μm)	60	Acrylic resin and cyclohexyl methacrylate (CHMA)	- TD in air at 450 °C for 1 h	- Sintering in Ar at 1350 °C for 1 h	ND	95	450 MPa, 30%	[160]
316L	- Pre-alloyed (PA) powder (−16 and −22 μm) - Master-alloyed (MA) powder (−16 and −22 μm)	65	50% PW, 40% PP, 10% linear LDPP	- SD in heptane at 60 °C for 4 h - TD between 200 to 500 °C	- Pre-sintering at 1000 °C - Sintering at 1340 and 1360 °C for 1 h	ND	PA-16, 1340 °C, 95.45 PA-22, 1340 °C, 97.8 PA-16, 1360 °C, 97.9 PA-22, 1360 °C, 99.1 MA-16, 1340 °C,98.35 MA-22, 1340 °C,97.72 MA-16, 1360 °C, 98.2 MA-22, 1360 °C, 97.7	581.1 MPa, 57.2% 587.0 MPa, 60.6% 581.3 MPa, 56.3% 582.5 MPa, 60.2% 541.0 MPa, 44.2% 527.7 MPa, 43.6% 534.2 MPa, 56.1% 536.5 MPa, 54.3%	[161]

Table 2. *Cont.*

Alloys	Powder Characteristics	Solid Loading (Vol.%)	Binder Detail	Debinding Process	Sintering Process	Shrinkage (%)	Relative Density (%)	UTS and % El	Ref.
316L (MPIF 35)	-	-	-	-	-	12–20 (* 15–18)	96.6	450 MPa, 40% (* 520 MPa, 50%)	[169]
Ti-6Al-4V	GA powder, D_{50} = 31.43 µm	65	69% PW, 10% CW, 10% APP, 10% EVA, 1% DBP	- SD in heptane at 48 °C for 5 h - TD in Ar at 600 °C for 1 h	- Sintering in vacuum 1350 °C, 4 h	ND	96	910 MPa, 15%	[170]
Ti-6Al-4V	GA powder, D_{50} = 28.8 µm	65	69% PW, 10% CW, 10% APP, 10% EVA, 1% DBP	- SD in heptane - ND of TD	- Sintering in vacuum at 1350 °C, 4 h	ND	97.4	840 MPa, 15%	[163]
Ti-6Al-4V	GA powder, D_{50} = 28.8 µm	65	69% PW, 10% CW, 10% APP, 10% EVA, 1% DBP	- SD in heptane - ND of TD	- Sintering in vacuum at 980 °C, 96 h	ND	98.8	925 MPa, 18%	[163]
Ti-6Al-4V	GA powder, <45 µm	65	60% PW, 35% EVA, 5% SA	- SD in heptane at 40 °C for 20 h - ND of TD	1250 °C, 2 h	ND	96.4	824 MPa, 13.4%	[164]
Ti-6Al-4V	GA powder, <45 µm	69	60% PW, 35% EVA, 5% SA	- SD in heptane at 40 °C for 20 h - ND of TD	1250 °C, 2 h	ND	96.6	806 MPa, 13.7%	[164]
Ti-6Al-4V	GA powder, <45 µm	68	PW, PE, SA	- SD in heptane at 40 °C for 20 h - ND of TD	1250 °C, 2 h	ND	96.5	800 MPa, 15%	[171]
Ti-6Al-4V (JPMA)	-	-	-	-	-	-	95	800 MPa, 5%	[172]

Table 3. Metal MEX feedstocks and debinding processes: alloys, powder characteristics, solid loading, binder and its debinding process, classified by feeding system (ND is no detail; SP is spherical powder; IP is irregular powder; SD is solvent debinding; TD is thermal debinding; HR is heating rate).

Type of Printing	Alloys	Powder Characteristics	Solid Loading	Binder	Feedstock	Debinding Process	Ref.
Screw-based	17-4PH	SP (2 to 10 μm)	93.5 wt.%	PEG and wax	MIM feedstock (PolyMIM)	- SD in a water for 12 h at 60 °C for 12 h - TD in He-4% H_2 at 500 °C for 1 h (HR of 1 °C/min)	[41,92]
Screw-based	316L	ND	55 vol.%	Thermoplastic	MIM feedstock (3 mm granule size)	- TD holding at 450 °C and 600 °C	[41]
Screw-based	WC-Co	ND	ND	TPE and PP	MIM feedstock	- SD in a mixture of H_2O with 2% inhibitor at 60 °C for 48–72 h - TD in H_2/N_2 atmosphere at 600–800 °C	[50]
Screw-based	Cu	Mean size = 5.9 μm	93.5 wt.%	PEG and wax	MIM feedstock (polyMIM Cu999 from PolyMIM)	- SD in a water at 60 °C for 48–72 h - TD in He-4% H_2 at 500 °C for 1 h (HR of 1°C/min)	[84,85,87]
Plunger-based	17-4PH	ND	79 vol.%	Water-soluble PEG	MIM feedstock	- SD in water at 60 °C for 10 h	[36]
Plunger-based	316L	Sandvik Osprey	63 vol.%	Water-soluble Embemould K83 binder	In-house prepare (granulated feedstock)	- SD in agitated water at 40 °C for 48 h - TD at 145 °C for 4 h (HR of 20 °C/h) and at 300 °C for 2 h (HR of 10 °C/h)	[68]
Plunger-based	Ti-6Al-4V	D_{90} = 19 μm	66 vol.%	Element 22 binder system	MIM feedstock (<2 and <9 mm in granule size)	- No action	[61]
Plunger-based	AZ91	<45 μm	64 vol.%	ND	ND	- SD in Hexane at 40 °C for 15 h - TD at 350 °C to 460 °C (HR of 0.5 °C/min) in Ar + 5 vol.% H_2 and at 350 °C in vacuum	[61,87]
Filament-based	17-4PH	D_{50} = 3.97 μm	63 vol.%	Polymeric blended binder	1.75 mm diameter	- SD > 12 h - TD at 450 °C for 1.7 h	[8,110]

Table 3. *Cont.*

Type of Printing	Alloys	Powder Characteristics	Solid Loading	Binder	Feedstock	Debinding Process	Ref.
Filament-based	17-4PH	SP (22 μm (3.9 to 44 μm)) IP (10 μm (2.8 to 44 μm))	58 vol.%	In-house developed binder (ECG2)	In-house prepared (1.78 mm diameter of die)	ND	[34]
Filament-based	17-4PH	325 mesh size	60 vol.%	30 wt.% wax, 35 wt.% polymer, 15 wt.% tackifier, and 20 wt.% elastomer	In-house prepared (1.78 mm diameter)	ND	[31,32]
Filament-based	17-4PH	10 μm	60 vol.%	POM, PP and PW (Taisei Kogyo, Co., Ltd., Tokyo, Japan)	In-house prepared (1.73 mm diameter)	- TD at 600 °C for 2 h in N_2 atmosphere	[64]
Filament-based	17-4PH	D_{10} = 4.2, D_{50} = 12.3, D_{90} = 28.2 μm, Sandvik Osprey, Ltd., Neath, UK	55 vol.%	Multicomponent binder system	In-house prepared (1.75 mm diameter of die)	- SD in cyclohexane at 23, 40, 60 and 75 °C - TD at 650 °C in N_2/H_2 atmosphere	[38,43]
Filament-based	17-4PH	SP, D_{50} = 12.3 μm	55 vol.%	Two-component binder	In-house prepared (1.75 mm diameter of die)	- SD in cyclohexane at 60 °C - TD by OBE (Ohnmacht & Baumgaertner GmbH & Co. KG, Ispringen, Germany)	[44]
Filament-based	17-4PH	D_{10} = 4.2, D_{50} = 12.3, D_{90} = 28.2 μm, Sandvik Osprey, Ltd.	55 vol.%	TPE and PO	In-house prepared (1.75 mm diameter)	- SD in cyclohexane at 70 °C - TD at 600 °C in H_2 atmosphere (HR = 120 °C/h)	[49]
Filament-based	316L	D_{50} = 30.8 μm and D_{50}=10 μm	50 vol.%	PP, SEBS, PW and SA	ND	- SD in cyclohexane at 60 °C for 18 h or 70 °C for 6 h - TD 350-440 °C for 1–4 h in H_2 or H_2 + Ar	[105]
Filament-based	316L	D_{50} = 2.8 μm, Sandvik Osprey, Ltd.	50 vol.%	LDPE, TPE and SA	In-house prepared (1.75 mm diameter)	- SD in cyclohexane at 60 °C - TD at 370–470 °C in H_2	[106]
Filament-based	316L	SP, D_{50} = 6.9 μm	50 and 55 vol.%	PA	In-house prepare	- TD at 200–450 °C	[29]

Table 3. *Cont.*

Type of Printing	Alloys	Powder Characteristics	Solid Loading	Binder	Feedstock	Debinding Process	Ref.
Filament-based	316L	ND	60 vol.%	POM and PW (Taisei Kogyo, Co., Ltd., Tokyo, Japan)	In-house prepared (1.73 mm diameter)	- TD at 600 °C for 2 h in N_2 atmosphere	[56]
Filament-based	316L	ND	55 vol.%	Thermoplastic binder	ND	- SD in cyclohexane 60 °C for 10.5 h	[35]
Filament-based	316L	Epson-Atmix Corporation	55 vol.%	TPE, three types of PO and two types of compatibiliser	In-house prepared (2 mm diameter of die)	ND	[37]
Filament-based	316L	D_{10} = 6.1, D_{50} = 15.1 µm, D_{90} = 25.5, Carpenter Powder Technologies AB	55 vol.%	Multicomponent binder system	In-house prepared (1.75 mm diameter of die)	- SD in cyclohexane at 23, 40, 60 and 75 °C - TD at 550 °C in Ar + 5% H_2 atmosphere	[38]
Filament-based	316L	SP, D_{50} = 6.05 µm	55 vol.%	TPE, PO and compatibilizer	In-house prepared	- SD in cyclohexane at 60 °C for 3 to 12 h	[39]
Filament-based	316L	SP, D_{50} = 8.6 µm	55 vol.%	Two-component binder	In-house prepared (1.75 mm diameter of die)	- SD in cyclohexane at 60 °C - TD by OBE (Ohnmacht & Baumgaertner GmbH & Co. KG, Ispringen, Germany)	[44]
Filament-based	316L	ND	83 wt.%	Two types of binder	Virtual foundry (1.75 mm diameter)	- TD at 450 °C in H_2 atmosphere (HR = 5 °C/min)	[48]
Filament-based	316L	Mean size = 17.7 µm, Carpenter technologies	55 vol%	TPE and PO	In-house prepared	- SD in cyclohexane at 65 °C for 0.5 to 57 h. - TD at 750 °C for 1.5 h in vacuum (HR = 5°C/min)	[52]
Filament-based	316L	30–50 µm	>88 wt.%	POM, PP, DOP, DBP and ZnO	Ultrafuse 316LX filament (1.75 mm)	- Catalytic debinding	[9]
Filament-based	316L	30–50 µm	>88 wt.%	POM, PP, DOP, DBP and ZnO	Ultrafuse 316LX filament (1.75 mm)	- Catalytic debinding in acidic gases at 120 °C - TD in H_2 at 600 °C for 1 h (HR = 5 °C/min)	[45]

Table 3. *Cont.*

Type of Printing	Alloys	Powder Characteristics	Solid Loading	Binder	Feedstock	Debinding Process	Ref.
Filament-based	316L	30–50 µm	80 wt.%	POM, PP, DOP, DBP and ZnO	Ultrafuse 316LX	- Catalytic debinding in HNO_3 gases at 110°C - TD in H_2 at 600 °C for 1 h (HR = 5 °C/min)	[53]
Filament-based	316L	30–50 µm	88 wt.%	POM, PP, DOP, DBP and ZnO	Ultrafuse 316LX	- Catalytic debinding at 120 °C under HNO_3 - TD in H_2 at 600 °C for 2 h (HR = 5 °C/min)	[57]
Filament-based	316L	30–50 µm	80 wt.%	ND	Ultrafuse 316LX filament (2.85 mm)	- Catalytic debinding at 120 °C for 8 h under HNO_3 (1 L/h) - TD in in H_2 at 600 °C for 1 h (HR = 5 °C/min)	[66]
Filament-based	316L	30–50 µm	88 wt.%	POM, PP, DOP, DBP and ZnO	Ultrafuse 316LX filament (2.85 mm)	- Catalytic debinding in acidic gases at 120 °C (1–2 mm/h) - TD in H_2 at 450 and 600 °C for 1 h (HR = 5 °C/min)	[70]
Filament-based	316L	30–50 µm	88 wt.%	POM, PP, DOP, DBP and ZnO	Ultrafuse 316L filament	- Catalytic debinding in HNO_3 gases - TD in H_2 at 450 and 600 °C for 1 h (HR = 5 °C/min)	[107]
Filament-based	316L	30–50 µm	90 wt.%	POM, PP, DOP, DBP and ZnO	Ultrafuse 316L filament (2.85 mm)	- Catalytic debinding in acidic gases at 120 °C (1–2 mm/h)	[73]
Filament-based	316L	30–50 µm	90 wt.%	POM, PP, DOP, DBP and ZnO	Ultrafuse 316LX filament (1.75 mm)	- Catalytic debinding in HNO_3 gases at 110–140 °C (2 mm/h) - TD in H_2 at 600 °C for 1 h (HR = 5 °C/min)	[98]
Filament-based	316L	3–15 µm (AEM Ltd., Changsha, China)	80 wt.%	92 vol.% PE and 8 vol.% SA	In-house prepared (0.75 mm diameter)	- TD at 200 °C for 2 h and 425 °C for 1 h (HR = 5 °C/s)	[81]

Table 3. *Cont.*

Type of Printing	Alloys	Powder Characteristics	Solid Loading	Binder	Feedstock	Debinding Process	Ref.
Filament-based	316L	0.872–76 µm (D_{50} = 32.7 µm)	83.5 wt.%	Filamet filament (PLA)	Virtual foundry	- TD in Ar atmosphere (0.28 l/min)	[72]
Filament-based	316L	Nitrogen atomised 20–53 µm, Hoganas (AM 316L)	65 vol.%	LDPE RIBLENE MV 10 R ENI Versalis	In-house prepared (1.75 mm diameter of die)	- TD at 500 °C for 1.5 h in a controlled O_2-free atmosphere (H_2 partial pressure 0.4 bar; HR = 5 °C/min)	[75]
Filament-based	316L	D_{10} = 4.6, D_{50} = 9.4, D_{90} = 16 µm	60 vol.%	POM, TPE, ULDPE	In-house prepared	- TD at 500 °C in H_2 atmosphere	[83]
Filament-based	Ti-6Al-4V	SP (<20 µm)	0–65 vol.%	27.5 wt.% PVA, 45 wt.% PP-PE, 22.5 wt.% PIB and 5 wt.% SA	In-house prepared	- No action	[91]
Filament-based	Ti-6Al-4V	SP, D_{50} = 14.97 µm	55 vol.%	TPE, PO and compatibiliser	In-house prepared	- SD in cyclohexane at 60 °C for 3 to 12 h	[39]
Filament-based	Ti-6Al-4V	SP, D_{50} = 14.97 µm	55 vol.%	Two-component binder	In-house prepared (1.75 mm diameter of die)	- SD in cyclohexane at 60 °C - TD by OBE (Ohnmacht & Baumgaertner GmbH & Co. KG, Ispringen, Germany)	[44]
Filament-based	Ti-6Al-4V	Fine SP (D_{10} = 7, D_{50} = 13, D_{90} = 21 µm) Coarse SP (D_{10} = 2, D_{50} = 30, D_{90} = 44 µm)	59 vol.%	Several polymeric components	In-house prepared (1.75 mm diameter of die)	- No action	[59,76]
Filament-based	Ti-6Al-4V	D_{10} = 1.8, D_{50} = 6.7, D_{90} = 6.8 µm, American Elements	55-59 vol.%	Polyolefin-based binder system	In-house prepared (2.85 mm diameter)	- SD in acetone at 60 °C for 24 h - TD at 300 (HR = 5 °C/min) and 550 (HR = 2 °C/min)	[63]
Filament-based	Ti-6Al-4V	Fine SP, D_{50} = 13 µm Coarse SP, D_{50} = 30 µm	59 vol.%	ND	In-house prepared (1.75 mm diameter)	ND	[78]

Table 3. *Cont.*

Type of Printing	Alloys	Powder Characteristics	Solid Loading	Binder	Feedstock	Debinding Process	Ref.
Filament-based	Ti-6Al-4V	Coarse SP, D_{50} = 30 µm	59 vol.%	ND	In-house prepared (1.75 mm diameter)	- SD in n-heptane solution at 64 °C for 4 h - TD in partial vacuum at 250 °C for 3 h, 330 °C for 3 h, 440 °C for 4 h and 550 °C for 4 h	[79]
Filament-based	CP-Ti	Mean size = 23.4 µm	55 vol.%	Styrene-based TPE and insoluble grafted polyolefin	In-house prepared (1.75 mm)	- SD in 99.5% cyclohexane - TD in Ar or vacuum at 170 to 450 °C (HR = 0.2 °C/min)	[102]
Filament-based	WC-10% Co	ND	50 vol.%	TPE and PP	In-house built (1.75 mm)	- SD in a mixture of H_2O with 2% inhibitor at 60 °C for 48–72 h - TD in H_2 or N_2 atmosphere at 600–800 °C	[50]
Filament-based	WC-Co	ND	<50 vol.%	30 wt.% wax, 35 wt.% polymer, 15 wt.% tackifier, and 20 wt.% elastomer (1% of Oleyl alcohol)	In-house prepared (1.78 mm diameter)	ND	[31,32]
Filament-based	High carbon-Fe	1.45–756 µm (D_{50} = 129 µm)	80 wt.%	Filamet filament (PLA)	Virtual foundry	- TD in Ar atmosphere (0.28 L/min)	[72]
Filament-based	M2	SP, D_{50} 26.93 µm	50–60%	TPE and PO	In-house prepared (1.75 mm)	- SD in cyclo-alkane at 65 °C - TD in N_2 atmosphere at 450 for 1 h °C (HR = 1 °C/min)	[96]
Filament-based	Cu	ND	ND	PLA based	Virtual foundry filament (2.85 mm diameter)	- SD at 150 °C in H_2 for 1.25 h and 400 °C (HR = 1.25 °C/min)	[51,89]
Filament-based	Cu	D_{50} = 46.6 µm D_{50} = 16.2 µm D_{50} = 6.67 µm	61 vol.%	Polyolefin waxes, ethylenic polymers and TPE	In-house prepared	- TD at 500 °C in Ar + 5 vol.% H_2 (HR = 1 °C/min)	[51,86]
Filament-based	Cu	SP, D_{10} = 6.8, D_{50} = 16 and D_{90} = 33.6 µm.	55 vol.%	TPE and PP	In-house prepared (1.75 mm)	- SD in cyclohexane at 60 °C up to 24 h - TD in H_2 atmosphere at 450 °C for 2 h	[90]

Regarding the solid loading of feedstock used in the MIM process (Table 2), it lies in the range of 60 to 69 vol.%, with the common range of 60 to 65 vol.%. The higher solid loading of the feedstock provides a higher density with lower dimensional shrinkage after sintering [149]. However, the higher solid loading of the feedstock results in higher viscosity, which is thus difficult to inject. For the metal MEX process, comparable or higher solid loading of granule or bar feedstock can be utilised in the screw-based and plunger-based type, as presented in Table 3. The solid loading can reach up to 79 vol.% [36]. It must be noted that the filament feedstock has lower solid loading (50 to 60 vol.%) than feedstocks for MIM or for screw-based and plunger-based types. This is due to the brittleness of the filament feedstock associated with high solid loading, which makes handling and spooling difficult [37]. The sensitivity of the solid loading content on the brittleness of the filament is presented by Gonzalez-Gutierrez et al. [4], shown in Figure 8. A 5% increment from 55 to 60 vol.% solid loading can significantly induce the brittleness of the 316L and $Fe_{12}O_{19}Sr$ filaments. However, to achieve as high as possible solid loading of filament, a multi-component binder with high elasticity must be used or additional heaters are required to reduce brittleness.

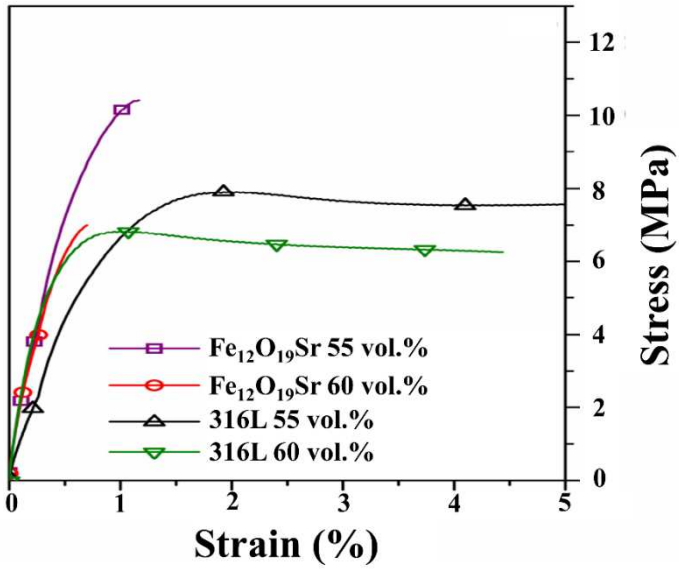

Figure 8. Tensile curves of and $Fe_{12}O_{19}Sr$ and 316L filament with different solid loading, showing the reduction in strain with 5% increment of solid loading (adapted from [4]).

2.3. Printing

The MEX printing process fabricates the as-printed or "green" part after the CAD model has been sliced, the printing path generated and the fundamental printing parameters optimised. An as-printed part is illustrated in Figure 9, showing the printing path in the top (Figure 9b) and side views (Figure 9c).

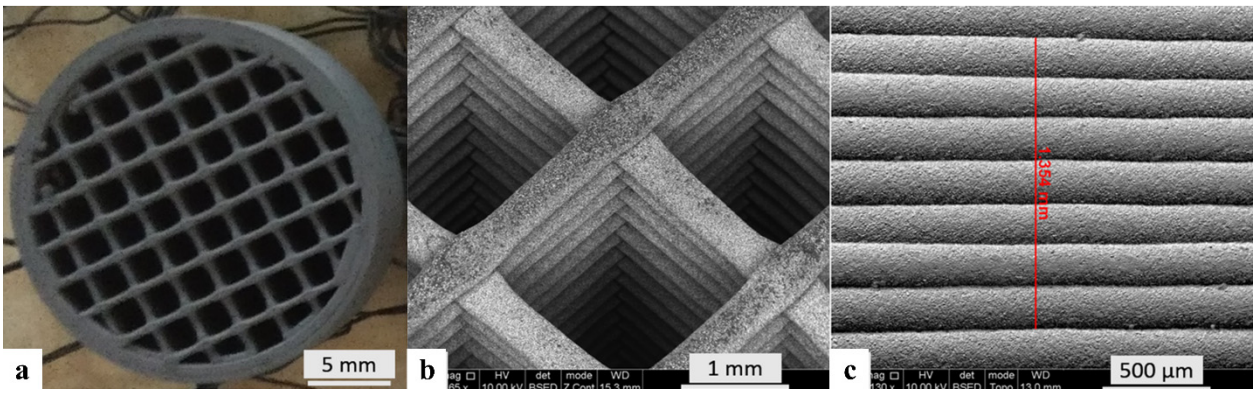

Figure 9. An as-printed part fabricated by metal MEX process, using an in-house developed 316L filament: (**a**) overview of the as-printed part, (**b**) top view and (**c**) side view (adapted from [83]).

To achieve satisfactory sintered parts, i.e., defect-free and having the highest relative sintered density, the printing parameters must be carefully controlled [43,54]. Practically, the printing parameters must be optimised case by case depending on the printer system, feedstock and the shape and size of the printed part. Although there are several adjustable printing parameters, some of these are more critical in determining the final properties of the green part and as such have been commonly studied, e.g., printing and/or printing bed temperature, number of perimeters, infill pattern and density, printing speed of perimeter and/or infill, flow rate multiplier and layer thickness, as shown in Table 4. The nature of the binder, metal powder, solid loading and printing speed determine the printing temperature, which lies in the range of 80 to 260 °C, similar to injection moulding temperature for MIM. Similar to MIM, the most important factor influencing shape formation is the binder. Feedstock with water-soluble binder [68] requires lower printing temperature than those with solvent and/or thermal debinding, e.g., TPE and PO [49,52,54], PA [29], POM [9,53,56,57,66,70], PLA [72] or PE [75,81] based binders. The printing bed is heated in the range of 40 to 100 °C to increase the adhesion and reduce warping defects generated by the shrinkage during solidification [77,173]. This is a common practice in polymer FDM. The printing bed temperature is suggested to be slightly lower than the glass transition temperature of the binder [173]. Apart from the heated printing bed, adhesive coatings, e.g., blue painters tape, water-soluble glues, hair sprays, polyimide, polypropylene, polypropylene film, polyetherimide and special coatings, are commonly applied on the printing bed to increase the adhesion [43,66,93,102,173,174]. To avoid this warpage issue, the commercial closed systems, MetalX by Markforged, Inc. and Studio+ System by Desktop Metal, Inc., utilise a raft, which is printed layers between the part and the printing bed to improve the adhesion [47,62,93]. The raft is the same material as the printed part and is separated from the part by printed ceramic layers (called an "interface" by Desktop Metal, Inc. and "ceramic release" by Markforged, Inc.). The ceramic printing head is a special feature of both commercial closed systems. The ceramic layers will allow the raft or support to be manually removed after sintering. The raft has a larger base area than the printed part and can sometime be a large portion of the printed green set, especially for small parts. In practice, the raft should be minimised or eliminated. In addition, the ceramic layers can be used to prevent two printed movable surfaces/parts to fuse together during sintering. In some cases [7,49,57], the printing chamber is also heated to increase the flexibility of the filament. Printing with a perimeter is optional and the number of perimeters is varied. To obtain high quality green parts, at least a few perimeters are highly recommended. The infill patterns, which are commonly investigated, are rectilinear, zig-zag and concentric with 100% infill density.

Table 4. Printing parameters reported in the literature classified by feeding system corresponding to Table 3 (ND is no detail; VF is Virtual Foundry filament; UF is Ultrafuse filament).

Printer Type	Alloys	Binder (Solid Loading, %)	Printer	Nozzle Diameter (mm)	Feedstock Size (mm)	Printing Temperature (°C)	Printing Bed Temperature (°C)	Number of Perimeters	Infill Pattern	Infill Density (%)	Printing Speed: Perimeter/Infill (mm/s)	Flowrate Multiplier (%)	Layer Thickness (mm)	Ref.
Plunger-based	316L	Water-soluble Binder (63)	In-house built	0.8	ND	135	ND	0	Rectilinear	100	7.5, 12.5, 17.5	ND	0.3, 0.4, 0.5	[68]
	316L	DM feedstock (ND)	Studio+ system	0.4	Diameter = 6, length = 150	175	65	2	Rectilinear	100	30	ND	0.15	[108]
	Ti-6Al-4V	(66)	In-house built	0.4	ND	95	60	ND	Rectilinear	100	20	100	0.2	[109]
	Ti-6Al-4V	(66)	In-house built	0.4	<2, <9	80	60	3	Rectilinear	100	4.09, 8.18, 12.27	ND	0.2	[61]
Screw-based	17-4PH	PEG and wax (93.5 wt.%)	ExAM 255	0.4	ND	196	60	ND	ND	100	20	120	0.05	[84,92]
	Cu	PEG and wax (93.5 wt.%)	ExAM 255	0.4	ND	180–220	60	ND	Rectilinear	100	20–100	90–150	0.05–0.25	[84]
	Cu	PEG and wax (93.5 wt.%)	ExAM 255	0.4	ND	196	60	ND	Rectilinear	100	20	120	0.05	[85]
Filament-based	17-4PH	Polymeric-blended binder (63)	ND	0.3	1.75	220	75 (Chamber 70)	3	Rectilinear	100	20	ND	0.144	[8,110]
	17-4PH	ND	MetalX	ND	1.75	ND	ND	ND	Rectilinear	100	ND	ND	0.05, 0.125	[47]
	17-4PH	ND	MetalX	ND	1.75	ND	ND	4	Rectilinear	100	ND	ND	0.125	[65]
	17-4PH	ND	MetalX	ND	1.75	ND	ND	ND	Rectilinear	100	ND	ND	0.2	[67]
	17-4PH	ND	MetalX	ND	1.75	ND	ND	3	Rectilinear	100	ND	ND	ND	[69]
	17-4PH	TPE and PO	Duplicator i3 v2	0.6	1.75	235	100	1	Rectilinear	100	60/80	175	0.2	[49]
	17-4PH	TPE and PO	Prusa i3 MK3	0.4	ND	210–250	100	ND	Rectilinear	100	35	200 (first layer), 95–127	0.12, 0.15, 0.20, 0.25, 0.28	[54]
	17-4PH	POM, PP and PW (60)	L-DEVO M2030TP	0.4	1.73	170	70 (Chamber 80)	ND	Rectilinear	100	0.17	ND	0.1	[64]
	316L	PA (50)	Ultimaker 2	0.8	ND	235–240	ND	ND	ND	ND	14	ND	0.4, 0.1	[29]
	316L(VF)	ND	Prusa MK3 i3 FDM based	0.6	1.75	210	55	2	Rectilinear	100	50	90	0.1	[48]
	316L(UF)	POM (62)	Flashforge Dreamer FDM-based 3D printer	ND	1.75	235	ND	ND	ND	ND	60	ND	0.2	[9]
	316L(UF)	POM (62)	Funmat HT	ND	ND	235	60	ND	Rectilinear	25–125	ND	ND	0.2	[53]
	316L(UF)	POM (62)	Ultimaker 3	0.6	2.85	230	100	ND	Concentric	100	15	ND	0.1	[66]
	316L(UF)	POM PP DOP DBP ZnO (62)	CoLiDo metal 3D printer	ND	ND	230	-	ND	Rectilinear	ND		ND	0.2	[57]
	316L(UF)	POM PP DOP DBP ZnO (62)	TAZ6	0.5	2.85	240	100	ND	ND	100	30	ND	0.2	[70]

Table 4. *Cont.*

Printer Type	Alloys	Binder (Solid Loading, %)	Printer	Nozzle Diameter (mm)	Feedstock Size (mm)	Printing Temperature (°C)	Printing Bed Temperature (°C)	Number of Perimeters	Infill Pattern	Infill Density (%)	Printing Speed: Perimeter/Infill (mm/s)	Flowrate Multiplier (%)	Layer Thickness (mm)	Ref.
Filament-based	316L(UF)	POM (62)	Prusa i3 Mk3s	0.25, 0.4	1.75	ND	120	ND	Rectilinear	ND	20–34	ND	0.125, 0.2	[93]
	316L(UF)	POM (62)	GermanRepRap X500	0.4	1.75	240	90–140	4	Hexagonal	25, 50, 75, 100	25	100-200	0.2	[98]
	316L(UF)	POM PP DOP DBP ZnO (62)	Ultimaker S5	0.6	2.85	170, 240	100	3	Concentric, rectilinear	100	20, 50	ND	0.1, 0.4	[73]
	316L(UF)	POM (62)	TAZ6	0.5	ND	240	100	ND	ND	100	30	ND	0.2	[107]
	316L	TPE and PO (55)	Prusa i3 MK2	0.6	ND	ND	ND	2	Rectilinear	100	ND	125 (first layer)/105	0.2	[52]
	316L	POM and PW (60)	L-DEVO M2030TP	0.4	1.73	170	70 (Chamber 80)	ND	Rectilinear	100	0.17	ND	0.1, 0.3	[56]
	316L	PLA (83.5 wt.%)	Crane Quad 3D	0.8	ND	210	60	ND	ND	100	15	ND	0.53 (first layer)/0.2	[72]
	316L	LDPE (65)	Zmorph 2S	0.6	1.75	220	60	2	Rectilinear	100	80	ND	0.2	[75]
	316L	92 vol.% PE and 8 vol.% SA (80 wt.%)	ND	0.5	0.75	230	ND	ND	Zig-zag	100	30	ND	0.2	[81]
	316L	POM, TPE, ULDPE (60)	Prusa i3	0.4	1.75	210	ND	2	Grid	40	10	140	0.2	[83]
	316L	PP, SEBS, PW, SA (50)	Wanhao duplicator 4S	0.8	ND	220	110	ND	Line	ND	10	ND	0.1	[105]
	316L	LDPE, TPE, SA	Hephestos 2	0.25, 0.4, 0.6, 0.8	1.75	230	70	-	-	-	6	-	0.25	[106]
	17-4PH, 316L and Ti-6Al-4V	Multi-component binder (55)	Duplicator i3 v2 FFF machine	0.6	1.75	210, 220, 230, 240, 250, 260	60	1, 2	Rectilinear	100	60/80	100, 150, 200	0.15, 0.2 (first layer)	[43,44]
	Cu (VF)	PLA	Ultimaker 2	0.6	2.85	225	40	4	Rectilinear	100	10, 20	110	0.15, 0.225, 0.3	[46,51,89]
	Cu	TPE and PO (55)	German RepRap X1000	0.6	1.75	240	90	3	Hexagonal, diagonal, linear	25, 50, 75, 100	30	ND	0.3	[90]
	M2	TPE and PO (55)	Prusa Steel Black Edition Mark II	0.4	1.75	245	70	ND	ND	100	15	110	0.2	[96]
	Ti-6Al-4V	Several polymeric components (59)	Pulse 3D	0.4	1.75	ND	ND	ND	ND	ND	0.5–16 2.5–7.6	ND	ND	[59]
	Ti-6Al-4V	Polyolefin-based binder system (55–59)	Renkforce 1000 printer	0.4	2.85	190–210	60	2	Linear	100	50	90	0.1	[63]

Table 4. *Cont.*

Printer Type	Alloys	Binder (Solid Loading, %)	Printer	Nozzle Diameter (mm)	Feedstock Size (mm)	Printing Temperature (°C)	Printing Bed Temperature (°C)	Number of Perimeters	Infill Pattern	Infill Density (%)	Printing Speed: Perimeter/Infill (mm/s)	Flowrate Multiplier (%)	Layer Thickness (mm)	Ref.
Filament-based	Ti-6Al-4V	Several polymeric components (59)	ND	ND	1.75	240	65	ND	No infill (0/90°) zig-zag, Linear	100	10	ND	0.2	[76]
	Ti-6Al-4V	(59)	Pulse 3D	ND	1.75	240	65	3	(0/90°) zig-zag	100	10	90, 105, 120	0.15, 0.225, 0.3	[78]
	Ti-6Al-4V	(59)	Pulse 3D	0.4	1.75	240	65	3	(0/90°) zig-zag	100	10	ND	0.15	[79]
	Ti-6Al-4V	(59)	Pulse 3D	0.4, 0.35	1.75	240	65	ND	Zigzag, concentric	ND	15, 5	112.5, 90	0.15, 0.1	[88]
	CP-Ti	TPE and PO	Prusa i3 Mk2	0.6	1.75	280	80	ND	Alternating rectilinear, concentric	100	10	120	0.2	[102]

The printing speed and flow rate multiplier, which are known to have the greatest effect on the quality of the green parts, should be carefully adjusted [78]. For metal MEX, the feedstock is highly viscous when compared to general polymers, such as ABS, PLA and PA. Hence, a lower speed than general polymer FDM is suggested [76]. Singh et al. suggested printing speeds in the range of 5 to 15 mm/s, with a preferable speed of 10 mm/s. As reported by Singh et al., it is found that decreases in printing speed provide higher as-printed density [84]; however, slow printing speed increases the printing time [76]. Nevertheless, the printing speed can be increased, if the other related printing parameters, e.g., flowrate multiplier and printing temperature, are suitably adjusted [43]. It can be observed from Table 4 that the printing speed utilised according to the literature can reach up to 80 mm/s. Therefore, the printing speed should be as high as possible, with appropriate printing parameters to achieve defect-free as-printed parts. In addition, the higher flowrate multiplier significantly increases green density, which has been observed in Ti-6Al-4V [78], 17-4PH stainless steel [43] and Cu [84]. The layer thickness that has been used in the literature lies in the range of 0.05 to 0.4 mm, which is dependent on the capability of the printer system and also on the required production rate and surface roughness. Increased layer thickness generates higher surface roughness [84]. Furthermore, the cooling system is also critical for the metal MEX printing process [48,52]. The effects of these printing parameters on the properties will be discussed in Section 3.2. Further studies should be carried out to increase printing speed without compromising the quality of green and sintered parts, as printing is considered to be the bottleneck step for the metal MEX process.

2.4. Debinding

The debinding step of metal MEX is rather similar to MIM, as the binders are the same or may sometimes be slightly different. This process aims to remove the polymer binder after printing to create a "brown" part, which is a skeleton of metal powders ready for sintering. For the conventional multiple-component binder, the debinding process can be categorised into two steps [149], which are (1) primary debinding step to remove the plasticiser component of binder (low molecular weight polymer) and (2) secondary debinding step to remove the backbone component of the binder (high molecular weight polymer). In the primary debinding step, the plasticiser is removed and an interconnected pore path is created so that the backbone polymer can be easily removed in the secondary debinding step. Traditionally, this primary process can also be categorised into three types depending on which type of the polymer is used as the main binder; solvent debinding to mainly remove wax-based, catalytic debinding to remove POM-based binder (specially designed for Ultrafuse® filament) and water debinding to remove water-soluble binder, e.g., polyethylene glycol [149]. The solvent or water debinding can take 15 h or more depending on the thickness of the parts [149]. To reduce the total debinding time to around 8 h, the combination of solvent (acid) and thermal debinding, which is known as catalytic debinding, has been introduced by BASF, while both heat and acid are simultaneously applied. This requires a specially controlled catalytic debinding furnace. Although the part is primarily debound, it needs the secondary thermal debinding step to completely remove all remaining binder components, especially the backbone polymer, by evaporation in a controlled atmosphere, depending on the metallic powders. In some cases, with specially designed polyacetal-based binder [175], both primary and secondary debinding steps have been combined into only one multi-step 10-h thermal debinding process [134,158]. The benefit of this one multi-step thermal debinding is that it can be in the same continuous thermal cycle with the sintering process. One thermal cycle of debinding and sintering for stainless steel will take only around 24 h. This has been common practice in commercial mass production for MIM in Japan for 20 years [176] and has also been implemented for metal MEX. In early 2021, Desktop Metal Studio System 2.0 has been introduced with a similar concept of no solvent debinding (only printing and sintering units) [177].

The solvent agent that is used to debind the as-printed part depends on the type of binders. The typical solvent agent is a suitable organic compound. As presented in Table 3, heptane, cyclohexane and acetone are commonly utilised. These agents are similar to those used in the MIM process, e.g., heptane, as presented in Table 2. For a water-soluble-based binder, such as polyethylene glycol, heated water can be used as the debinding agent [50] to accelerate the debinding rate. Catalytic debinding was initially designed for the POM-based (polyacetal or polyformaldehyde) binder used in the MIM process [149], which is used in a commercial MIM feedstock known as Catamold® by BASF SE. Ultrafuse® filament was then developed by using a similar POM-based binder, which also needed to be catalytically debound. Catalytic acid vapour, which is nitric acid, with a temperature of 110 to 120 °C, is typically used [45,53,57,66]. The secondary debinding or thermal debinding process aims to thermally remove the backbone or other remaining binders in the printed parts [149]. This process is achieved by slowly heating the parts (1 to 5 °C/min for MIM [178]) to ensure that the backbone or remaining binder will be evaporated without defects. A multi-holding step may be necessary, depending on the remaining binders within the part after primary debinding, as observed in Tables 2 and 3. The debinding temperature depends on the type of the backbone polymer, according to the evaporation points of each type. This temperature can be exactly selected by thermo-gravimetric analysis (TGA) of the feedstock, filament or only binder by itself [149]. However, all binder types should be completely debound within a final temperature range of 450 to 600 °C, as observed for both MIM (Table 2) and metal MEX parts (Table 3). From Figure 10 exhibits C and O content uptake during debinding of Ti-6Al-4V MIM [179]; the C content after 600 °C and longer than 1 h is relatively constant after the binder is completely debound. However, the O content continuously increases with increasing debinding temperature and time. As low as possible debinding temperature and time is suggested to avoid O uptake, especially for Ti and its alloys [179]. In addition, the atmosphere of the furnace should be controlled to avoid any undesirable reaction during debinding. The atmosphere that is commonly used is an inert gas or vacuum depending on the alloys, as observed in Tables 2 and 3. Ar, N_2, H_2 and vacuum atmosphere are used for stainless steel, while Ar or vacuum are for Ti-6Al-4V alloy. Shibo et al. [179] reports that vacuum provides lower O when compared to the Ar flow atmosphere (Figure 11). On the other hand, MIMed Ti alloys can also be successfully debound using the Ar flow atmosphere [180–183].

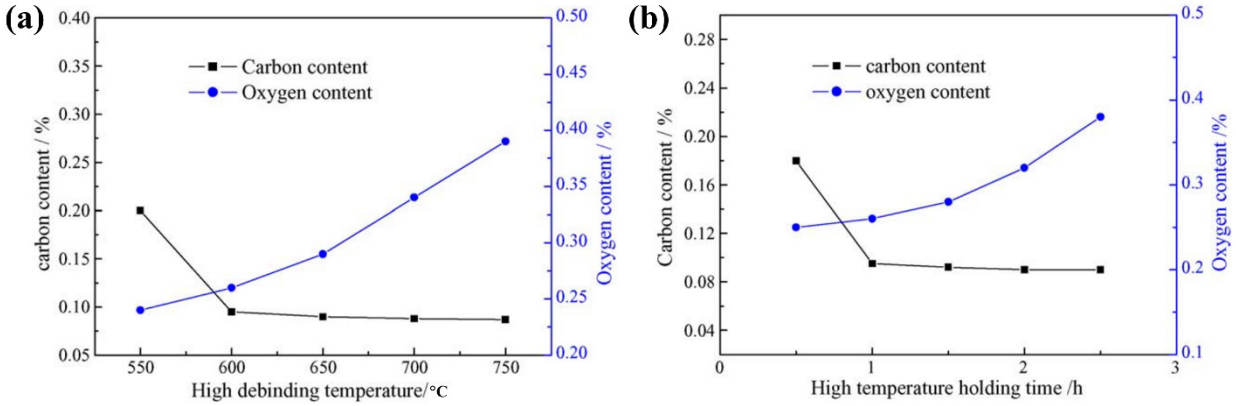

Figure 10. C and O uptake during debinding as a function of (**a**) debinding temperature and (**b**) sintering (holding) time during debinding of Ti-6Al-4V MIM (Reprinted with permission from [179]. Copyright 2006, Journal of Materials Processing Technology, Elsevier).

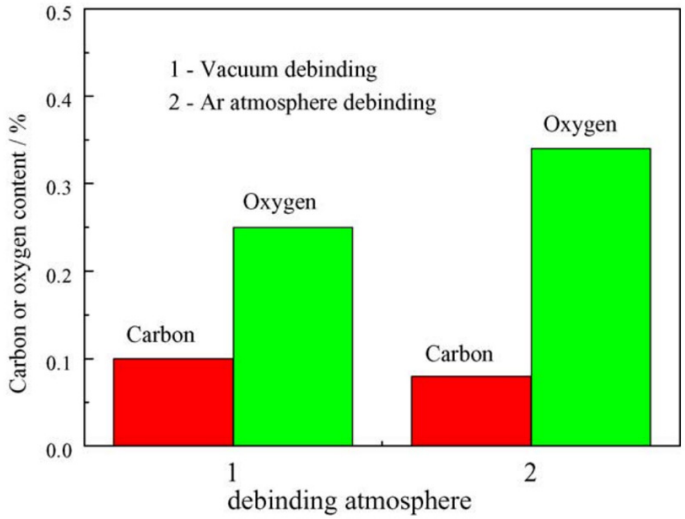

Figure 11. Effect of debinding atmosphere on the C and O uptake during debinding of Ti-6Al-4V MIM (Reprinted with permission from [179]. Copyright 2006, Journal of Materials Processing Technology, Elsevier).

2.5. Sintering

The sintering process is the thermal treatment of the parts to bond the metal powder so that densified components (up to 99%) can be achieved [184]. The mass transport, consisting of evaporation and condensation, surface diffusion and volume diffusion dominate during the initial stages of sintering, and then plastic flow, viscous flow, grain boundary diffusion and volume diffusion dominate after necks are formed between touching powder particles [149]. Shrinkage occurs at this stage in the range of 12% to 20% [127], depending on the material, powder type, size, distribution, solid loading, sintering temperature, sintering time [185] and printing quality. Figure 12 illustrates examples of as-printed and as-sintered Ti-6Al-4V specimens fabricated by the metal MEX process Figure 12a, demonstrating the difference in sizes originating from the shrinkage after sintering, similarly to the MIM process (Figure 12b)

The use of fine powder leads to higher diffusion rate, more shrinkage and hence provides higher relative sintered density when compared to larger powders [78]. Higher sintering temperature and longer sintering time also give more shrinkage and higher relative sintered density of the part [149]. As reported in Figure 13 [78], the relative sintered density of Ti-6Al-4V fabricated by metal MEX increase with increasing sintering temperature and time. However, significant grain growth, which compromises mechanical properties, is commonly observed at a high sintering temperature and time. Therefore, appropriate sintering temperature and time are needed to acquire an optimum combination between high relative sintered density and suitable grain size to achieve the required mechanical properties [124,186]. Although the powder size utilised in metal MEX tends to be smaller than that of MIM, the sintering temperature of the metal MEX and MIM are rather similar, as expressed in Table 5.

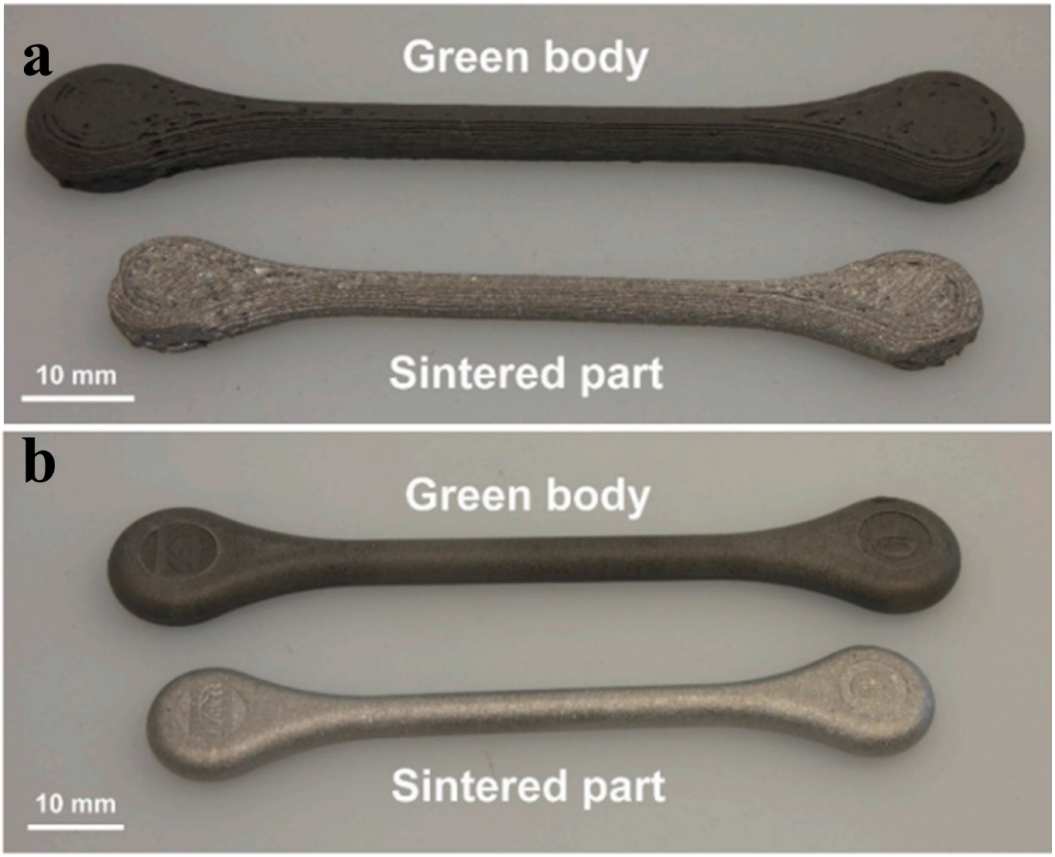

Figure 12. As-printed and as-sintered Ti-6Al-4V specimens fabricated by (**a**) metal MEX process and (**b**) MIM process, demonstrating the difference in sizes due to shrinkage upon sintering (adapted from [91]).

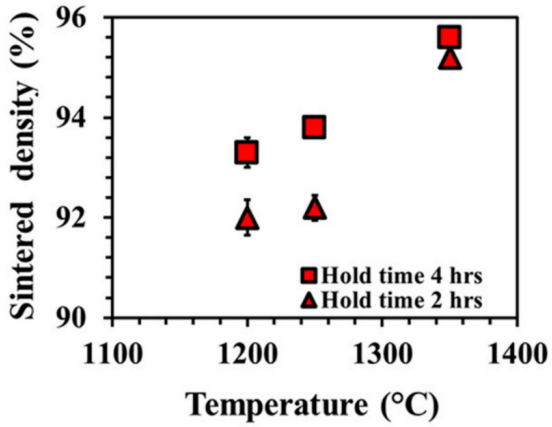

Figure 13. Relative sintered density of Ti-6Al-4V fabricated by metal MEX process sintered using varied sintering temperature and time, demonstrating the dependence of relative sintered density on the sintering temperature and time (Reprinted with permission from [78]. Copyright 2021, Powder Technology, Elsevier).

The typical sintering condition of 17-4PH is in the range of 1200 to 1350 °C for 1 to 3 h, 316L is 1250 to 1380 °C for 1 to 3 h, Ti-6Al-4V is 1200 to 1350 °C for 1.5 to 4 h and CP-Ti is 1150 to 1350 °C for 2 to 5 h. Pre-sintering at 900 to 1000 °C is also applied to stainless steel alloys [49]. It is noted that Ti-6Al-4V alloy is typically sintered in the β phase region. Interestingly, low sintering temperature with an extended sintering time

can also be applied to Ti-6Al-4V in MIM (as presented in Table 5 as 980 °C up to 96 h) to refine grain size [157,159,161,163]. This low sintering temperature within the α + β phase region for an extended time was proven to increase fatigue strength of MIM Ti-6Al-4V. Figure 14 shows the typical microstructure of Ti-6Al-4V fabricated by MIM (Figure 14a–c) and metal MEX (Figure 14d,e) sintered at the conventional sintering temperature (in the β region) and the low sintering temperature (in the α + β region). Grain refinement is clearly observed. In addition, the microstructure of parts fabricated by both processes in both sintering conditions is similar.

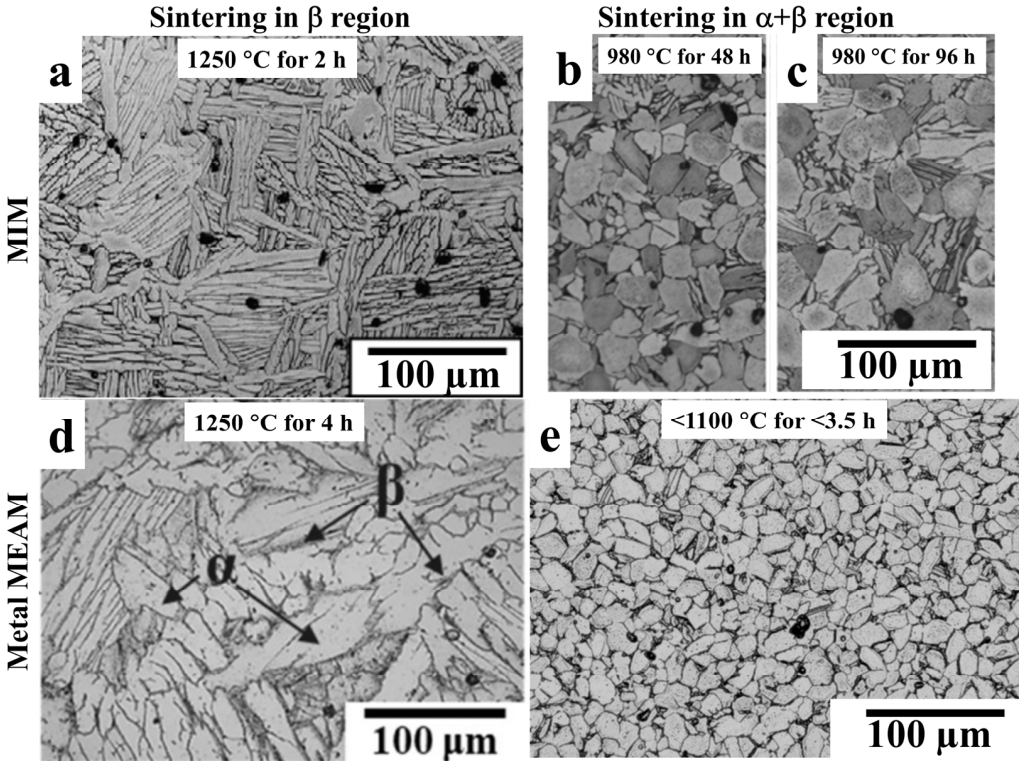

Figure 14. Microstructure comparison of Ti-6Al-4V parts (**a**) fabricated by MIM process sintered in the β region (Reprinted with permission from [171]. Copyright 2009, Materials Science and Engineering: A, Elsevier), (**b**,**c**) fabricated by MIM process sintered in the α + β region (adapted from [163]), (**d**) fabricated by metal MEX process sintered in the β region (Reprinted with permission from [78]. Copyright 2021, Powder Technology, Elsevier). and (**e**) fabricated by metal MEX process sintered in the α + β region for grain refinement (adapted from [109]).

The furnace atmosphere is one of the critical issues in the sintering process that influences the material properties, especially for Ti alloys, which are highly reactive with carbon, oxygen, nitrogen and hydrogen. Excessive impurity pick-up during debinding and sintering reduces elongation [124] owing to the formation α-phase by oxygen picking in CP-Ti [102] and the formation of brittle TiC generated by excessive carbon in beta Ti alloys [11,187,188]. As observed from Table 5, atmospheres suitable for sintering of stainless steel are H_2, N_2, Ar and vacuum, but the atmosphere for the sintering of CP-Ti and Ti-6Al-4V is limited to Ar or vacuum. It has been suggested that Ti sponge material with a high specific area should be placed in the sintering furnace with MIM Ti parts to scavenge any impurities in the furnace atmosphere [124,189].

Table 5. Sintering parameters used in metal MEX and MIM processes classified by alloys (ND is no detail).

Alloys	Sintering Atmosphere	Heating Rate (°C/min)	Sintering Temperature (°C)	Sintering Time (h)	Ref.
17-4PH	H_2	ND	1360	ND	[36]
	96% Ar + 4% H_2	ND	1200	3	[8,110]
	H_2	5	1260	3	[34]
	H_2 + N_2	ND	1350	1	[31,32]
	Ar	ND	1280	2	[64]
	ND	ND	1050	3	[38,43]
	ND	4	1360	3	[92]
	ND	0.15, 4.16	900 (pre-sintering)/1380	1.5/5	[49,92]
MIM 17-4PH	Partial pressure of Ar	ND	1000 (pre-sintering)/ 1350	0.25/2	[157]
	Ar	ND	1325	2	[134]
316L	ND	2.17	1350	1	[68]
	H_2	ND	1250	ND	[29]
	Ar	ND	1280	2	[56]
	Vacuum	20	1250	1.5	[38]
	Ar	5	1100	ND	[48]
	Vacuum	0.2	1330–1360	2	[52]
	H_2	5	1380	3	[45,53,107]
	Ar	5	1380	2	[57]
	Ar	5	1380	3	[66]
	ND	ND	1380	3	[98]
	ND	ND	900 (pre-sintering), 1380	0.75/ND	[70]
	ND	10	1320	2	[81]
	Ar	3	1310–1400	1, 6, 12	[72]
	ND	5	1380	3	[75]
	H_2	10	1250	ND	[83]
	H_2	5	1350	4	[105]
	H_2	5	1360	3	[106]
MIM 316L	Vacuum	ND	1050 (pre-sintering), 1380	0.75/3	[159]
	Ar	ND	1350	1	[160]
		ND	1000 (pre-sintering), 1340, 1360	1	[161]
CP-Ti	Ar and Vacuum	3	1350	5	[102]
MIM CP-Ti	Vacuum	ND	1150	2	[181]
Ti-6Al-4 V	Ar	ND	900, 1000, 1100, 1200, 1340	1.5	[63]
	Vacuum	ND	1200, 1250, 1350	2, 4	[78]
	Partial vacuum	3	1250	4	[79]
	Vacuum	ND	<1100	<3.5	[109]
MIM Ti-6Al-4V	Vacuum	ND	1350	4	[170]
	Vacuum	ND	980	96	[163]
	ND	ND	1250	2	[164,171]
WC-Co	N_2 at specific temperatures	ND	1150, 1430	ND	[50]
Cu	Oxidation	3.24	983	4	[51,89]
Cu	He-4% H_2	4/4	950 (pre-sintering)/1030	3/3	[84,85]
Cu	Ar + 5 vol.% H_2	5	1045	3	[86]
Cu	H_2	2	1050	1	[90]
M2	Vacuum	5	120 to 1280	1	[96]
AZ91	Pure Ar (Ar6.0)	2	605	4	[86,87,190]

3. Effects of Processing Parameters on Physical and Mechanical Properties

The appearance, dimensional accuracy, physical and mechanical properties of metal AM parts are essential requirements for end-user products, especially for assembled engineering parts. In this section, the processing parameters that influence the physical and mechanical properties of sintered metal AM parts will be systematically summarised and the properties of metal AM parts compared with those obtained in typical MIM parts and with the MIM international standards. The parameters include the effects of solid loading of metal MEX feedstock on the shrinkage after sintering, the effects of sintering conditions on the relative sintered density and the effects of printing parameters on physical and mechanical properties. To conclude the discussion, the mechanical properties of 316L, 17-4PH and Ti-6Al-4V MEX (most popular MEX alloys) will be evaluated based on those of MIM parts and MIM international standards. It is noted that there is currently no available metal MEX standard, hence MIM standards have been used for evaluation. The MIM international standards are the Metal Powder Industries Federation (MPIF) Standard 35 Metal Injection Moulding Materials for stainless steels and Japan Powder Metallurgy Association (JPMA) Standard Metal Injection Moulding Materials for Ti-6Al-4V. In addition, the MPIF standard does not cover titanium and titanium alloys. Hence, the JPMA standard is used. Standards for stainless steel are identical for both MPIF and JPMA.

3.1. Effects of Solid Loading of Metal MEX Feedstock on the Shrinkage

The effect of solid loading content on the shrinkage of 17-4PH stainless steel [8,36,44,49,64,127,158] and 316L stainless steel [9,35,37,38,41,44,45,52,53,56,57,66,68,70,75,98,127,159] with different sintering conditions is summarised in Figures 15 and 16, respectively. The solid loading of 17-4PH is in the range of 55% to 79% with measured shrinkage of 12% to 20% [8,36,44,49,64,158], which is similar to the typical shrinkage obtained in MIM (12% to 20% [127]). Generally, it is observed that as the solid loading increases, the shrinkage tends to decrease. The shrinkage depends on several factors, e.g., filament, metal powder, solid loading, sintering conditions and print orientations. For parts with 55% solid loading of 17-4PH stainless steel (orange circular and pink triangular and circular symbols in Figure 15), the dimensional shrinkage ranges from 15% to 20% depending on several variables, such as the measured directions and processing conditions. The shrinkage in the x-y direction is normally lower than that of in the z direction in MIM [73,77,191] and this commonly occurs in 316L stainless steel, where there are more data, as discussed in the next section. Sometimes, the opposite effect is observed in metal MEX [49], which may be due to the effects of printing parameters. The shrinkage in the z direction (the built direction) has the lowest shrinkage (15%), while the shrinkage in the x-y direction is 19% (pink circular and triangular symbols). At the same 60% solid loading for MIM and metal MEX, the measured shrinkage is comparable (purple-rectangular and green edge-circle symbols).

A consistent trend for 17-4PH is observed for 316L stainless steel in Figure 16. Sintered parts with higher solid loading tend to exhibit lower shrinkage. At 55 and 62 vol.% solid loadings of 316L stainless steel, a large variation of shrinkage is observed (14% to 20% and 13% to 25% for 55 and 62 vol.%, respectively). Although it is known that higher sintering temperature provides higher dimensional shrinkage, its effect may be lower when different processing parameters have been utilised, e.g., powder size and its distribution [192] and printing parameters; layer thickness and infill patterns [73]. These effects are observed for 62 vol.% solid loading, even though the same commercial feedstock was used (Ultrafuse filament, UF, represented by centre-dot symbols). The variation of shrinkage (13% to 25%) is wider than that of typical MIM values. It can be noted that most shrinkage values measured in the z direction (the built direction) are higher than those in the x-y direction (perpendicular to the built direction), which corresponds to the studies of Quarto et al. [73] and Ait-Mansour et al. [53], which focused on the shrinkage behaviour of the part. This behaviour can be explained through the combined effects of the higher thermal gradient along the z-direction when compared with the x-y direction, the effect of layer direction, layer thickness and infill pattern during printing [73,77], the friction-free z direction and

gravity [191]. It is also noted that the variation in shrinkage between x-y direction and z direction of MEX is more significant than in MIM, where isostatic pressure is applied. As observed, the shrinkage of metal MEX is varied in a wide range. Zhang et al. [101], therefore, proposed the predictive model of the meal MEX dimensional change using machine learning techniques. It is found that neural network algorithms provide the highest accuracy, which can successfully predict dimensional variations and optimise the printing and sintering process parameters of the metal MEX parts [101].

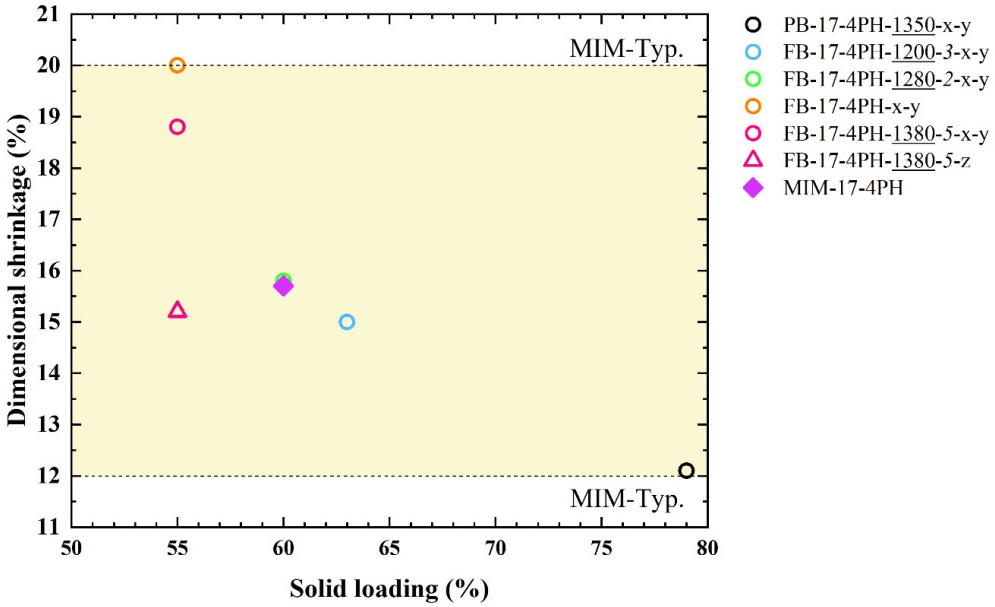

Figure 15. Solid loading vs. dimensional shrinkage map of 17-4PH stainless steel fabricated by metal MEX process with different conditions compared with typical MIM. The underlined number represents sintering temperature (°C); the italic number represents sintering time (h); and x-y (average from length and width) or z (thickness) indicate the direction of shrinkage measurement. Data from [8,36,44,49,64,127,158].

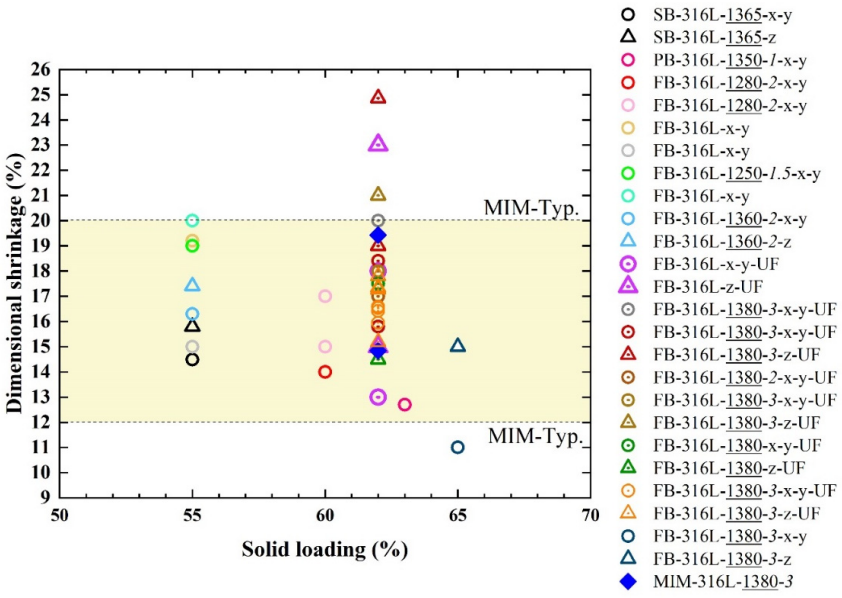

Figure 16. Solid loading vs. dimensional shrinkage map of 316L stainless steel fabricated by the metal MEX process with different conditions comparing with typical MIM. The underlined number

represents sintering temperature (°C) and the italic number represents sintering time (h); x-y (average from length and width) or z (thickness) indicate the direction of shrinkage measurement. Data from [9,35,37,38,41,44,45,52,53,56,57,66,68,70,75,98,127,159].

3.2. Effects of Printing Parameters on Physical and Mechanical Properties

The sintered properties critically depend on the quality of the as-printed parts. If the as-printed part has a high relative density without any defects, the corresponding sintered properties tend to have high physical and mechanical properties, as presented in Figure 17. Therefore, many early investigations were focused only on the effect of printing parameters on the as-printed parts. Among many adjustable printing parameters for the metal MEX process, there are common variables that have been investigated, for example, printing temperature, printing bed temperature, flow rate multiplier, layer thickness, built orientation, infill pattern and infill density.

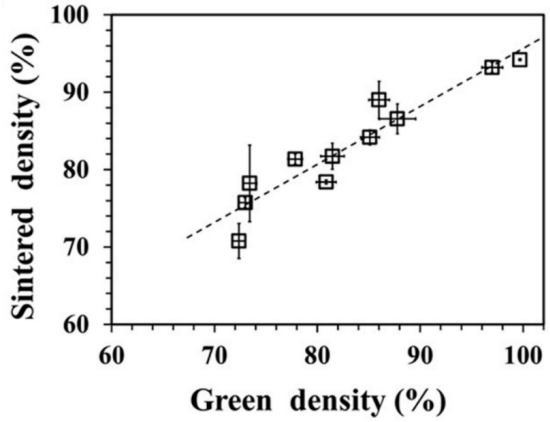

Figure 17. The green vs. sintered density of Ti-6Al-4V fabricated by metal MEX, demonstrating sintered density dependence on the green density (Reprinted with permission from [78]. Copyright 2021, Powder Technology, Elsevier).

Godec et al. report that an increase in the printing temperature significantly increases the as-printed tensile properties [54]. However, a too-high printing temperature can generate high residual stress, leading to warpage and deflection defects after printing, as reported by Singh et al. [76]. Godec et al. also report that an increase in the flow rate multiplier results in significant increases in the as-printed tensile properties [54]. This agrees well with the report of Singh et al. [78], which reports that the higher flowrate multiplier provides the higher relative density of both as-printed and sintered parts. In addition to effects on relative sintered density, Singh et al. reported that an increase in the flow rate multiplier up to 120% could improve the surface quality [84]. However, as reported by Rosnitschek et al. [98], a too-high flow rate multiplier (200%) results in the deformation of the printed parts because of excessive material. Regarding the layer thickness, most studies report that the thinner layer thickness leads to higher properties [56,68,73,84] due to the reduction of voids between the deposited paths. However, Godec et al. report that the increasing layer thickness provides better properties due to the reduction of weak points between the deposited paths [54]. This difference is likely to be because other processing parameters are different or not fully optimised. As reported by Singh et al. [78] and Quarto et al. [73], changes in the layer thickness do not significantly influence the density when enough binder is used and the distance between the nozzle and the deposited layer is carefully controlled. Nonetheless, as reported by Singh et al., a decrease in layer thickness from 0.25 mm down to 0.05 mm can decrease the surface roughness from approximately 18 to 8 μm.

The infill patterns that have been commonly used in metal MEX are rectilinear and concentric, as listed in Table 4. There is only one study reported by Gonzalez-Gutierrez

et al. [90] focusing on the effects of an infill pattern in metal MEX parts. It is found that the diagonal infill pattern and the linear with 0°, 0°/90° and 90° infill pattern have no significant difference on the flexural properties and density. In a polymer FDM investigation, Akhound et al. report that the pattern providing a parallel printed path to the load direction (concentric pattern) exhibits the highest tensile and flexural properties [193]. It is also found that the concentric pattern provides lower void fractions when compared to other infill patterns, e.g., rectilinear, honeycomb and Hilbert curves [193]. This well agrees with Pandzic et al. [194] that the highest tensile properties are obtained from the concentric infill pattern. However, Srinivasan et al. report that the rectilinear pattern provides higher tensile properties than concentric [195]. From the Ultrafuse 316L metal MEX tensile properties reviewed in this work, the rectilinear with 45°/90° pattern with appropriate printing parameters (nozzle size, printing speed, strand width, layer thickness and first layer adjustment) reported by Moritzer et al. [93] provides higher tensile properties than other infill patterns [66,98] and also similar infill patterns [53,57]. As reported by Singh et al. [79], the 0°/90° zigzag infill pattern in metal MEX can also provide comparable tensile properties to MIM parts. Therefore, it can be speculated that in the case of 100% infill with suitable printing parameters to create the fully dense part, the mechanical properties can be at a similar level although the infill patterns are different. However, in the case of low infill density for weight reduction, the mechanical properties could be significantly different, as reported by Gonzalez-Gutierrez [90]. For example, the flexural strength of 50% infill density of specimens printed with diagonal and linear infill patterns is similar but significantly higher than hexagonal. Nonetheless, this issue still needs further systematic investigation to understand the effects of different infill patterns on properties in relation to other metal MEX operating variables. In addition, tensile, compressive and flexural strengths tend to decrease with decreasing the infill density, as reported by Ait-Mansour et al. [53], Gonzalez-Gutierrez [90] and Rosnitschek [98].

The built orientation is an important issue that has been widely studied with three orientations, which are the flat, on-edge and vertical orientations. All available studies report that the vertical built orientation exhibits the lowest tensile properties due to layer delamination [8,53,56,64,68,81]. Figure 18 shows the difference in fracture surface characteristics and related failure mechanism of metal MEX specimen built by the flat (Figure 18a,c) and vertical orientations (Figure 18b,d). It shows that crack originates from the void between the printing paths and the interlayer bonding area, resulting in the low tensile properties of the vertical orientation parts. The difference in mechanical properties of the flat and on-edge orientations is still inconsistent. Kurose et al. [56] and Abe et al. [64] report that the on-edge orientation exhibits higher tensile properties than the flat built orientation, while Ait-Mansour et al. [53] and Suwanpreecha et al. [8] report that the flat orientation provides higher tensile properties than that of the on-edge built orientation. However, as reported by Damon et al. [45] and Caminero et al. [66], there is no significant difference in tensile properties between the flat and on-edge built orientations. As for tensile properties, flexural properties are also orientation dependent as reported by Suwanpreecha and Manonukul [110]. It is found that weak points between two layers can result in layer sliding during bending, leading to the difference in flexural strength and strain [110]. The degree of overhang also influences the mechanical properties, as studied by Alkindi et al. [65]. It is found that 0 to 10° hanging provides higher tensile properties. Furthermore, the printing of scaffold type structure or the supportless part is one of the unique characteristics of 3D printing. The printing parameters need to be carefully modified from the general printing of bulk parts, as reported by Shaikh et al. [88].

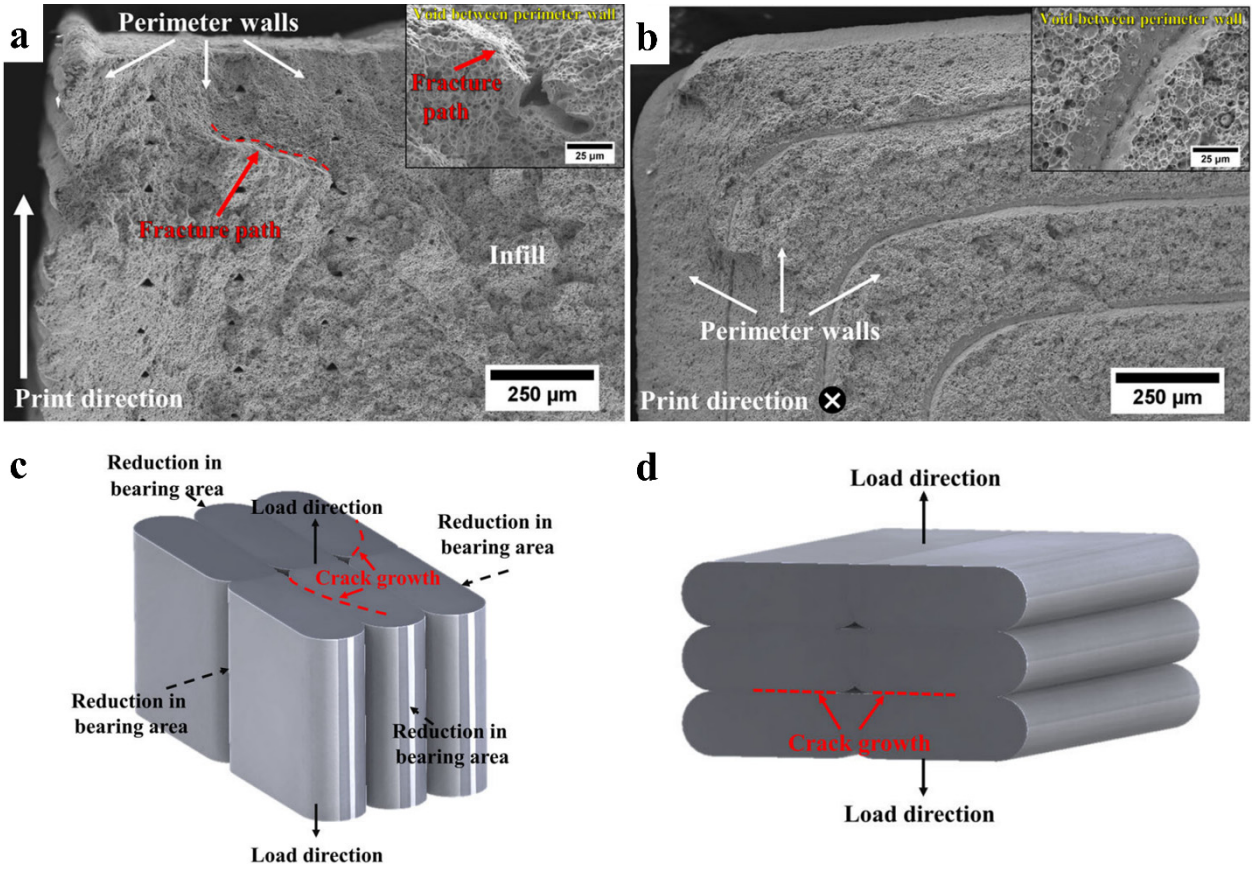

Figure 18. Fracture surface of metal MEX 17-4PH stainless steel specimens built with the (**a**) flat, (**b**) vertical orientations and schematics showing the failure mechanism of specimen built with the (**c**) flat and (**d**) vertical orientations (Reprinted with permission from [8]. Copyright 2021, Metallurgical and Materials Transactions A, Springer).

3.3. Effects of Sintering Conditions on the Relative Sintered Density of Alloys Compared to MIM

If there are no defects present, it is well known that the tensile properties critically vary with the sintered density, depending on sintering conditions [124,186,196]. The higher sintering temperature and longer sintering time provide the highest relative sintered density [149]. The effect of sintering conditions on the relative sintered density of 17-4PH [8,49,64,92,110], 316L [9,41,45,52,53,56,57,66,68,70,72,75,81,98,108] and Ti-6Al-4V [78,79] alloys fabricated by metal MEX, MIM [134,157,159–161,163,164,170,171] and the corresponding MIM international standards [169,172] are graphically compared in Figures 19–21, respectively. Figure 19 shows that most relative sintered densities of MEX 17-4PH alloy, which are in the range of 97% to 99%, meet the minimum value of the MPIF standard 35 for MIM materials (>96.7%). The relative sintered densities of parts sintered at 1200 °C (blue symbols) are comparable to those sintered at 1280 °C (red symbols) for metal MEX. In addition, they are comparable to those MIM sintered at 1350 °C (green symbols). MIM 17-4PH alloy with larger powder size is commonly sintered at a higher temperature than MEX 17-4PH, which has smaller powder size, as reported in Tables 2 and 3. This is expected, as the higher specific surface area associated with smaller powder enhances sintering. It is noted that the part sintered at 1380 °C for 5 h (black square symbol) should have the highest relative density; however, this value was reported in early work in this field [49], and, as such, the low relative sintered density may be the result of poor printing quality.

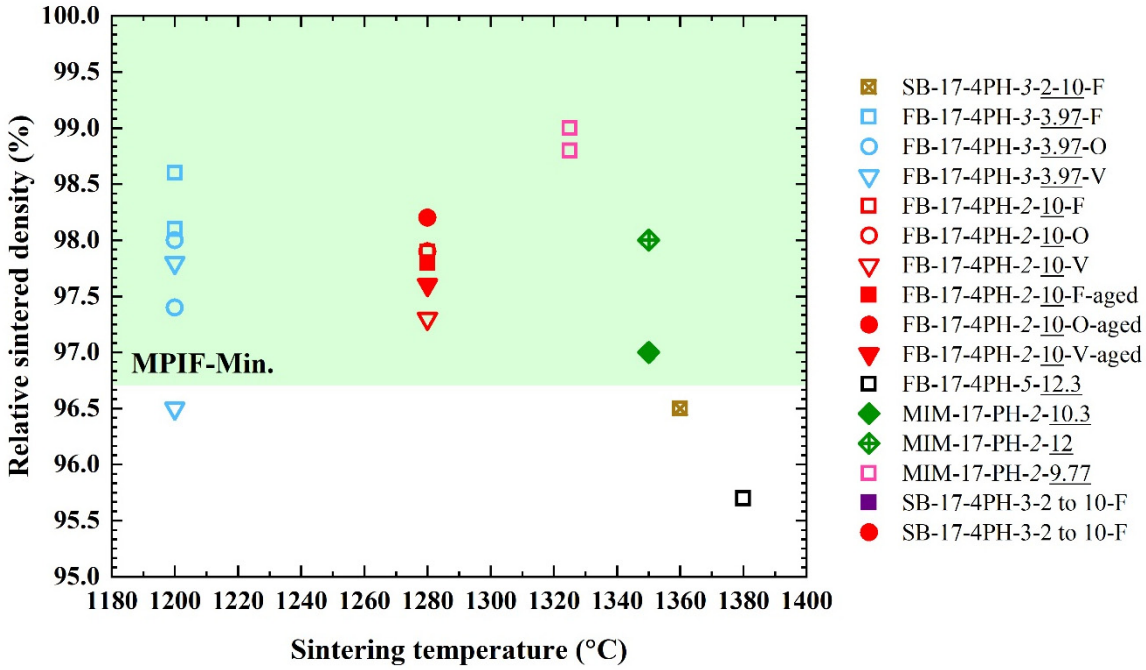

Figure 19. Sintering temperature vs. relative sintered density map of 17-4PH stainless steel fabricated by metal MEX process with different conditions comparing with MPIF standard 35 for MIM materials. The italic number represents sintering time (h) and the underlined number represents powder size (μm). F, O and V represent flat, on-edge and vertical printing orientations, respectively Data from [8,49,64,92,110,134,157,169].

For 316L stainless steel MEX (Figure 20), most reported relative sintered densities are lower than the minimum requirement of MPIF standard 35 for MIM materials (96.6%), and are in a wide range of 72% to 99%. The relative sintered density tends to increase as the sintering temperature increases and is highest at the sintering temperature of 1380 °C, which is comparable to MIM material sintered at 1360 °C. This is because both processes were using similar powder size. The secondary process, i.e., hot isostatic pressing, HIP (rectangular filled purple symbol) can raise the relative sintered density to 99.7% [81]. Interestingly, the effect of infill density has been firstly studied by Rosnitschek et al. [98]. The decrease in infill density tends to significantly decrease the relative sintered density, resulting in weight reduction (red rectangular centre-dotted symbols). It is noted that the relative densities for 50% and 75% infill seems to be inconsistent but there is no explanation in the literature [98].

From both 17-4PH and 316L stainless steel, it is observed that metal MEX parts that are fabricated with the flat and on-edge built orientations (red rectangular and circular symbols in Figures 19 and 20) exhibit higher relative sintered densities than the vertical built orientation (red triangle symbols in Figures 19 and 20) [56,68]. The Ti-6Al-4V alloy (Figure 21), demonstrates similar behaviour, as 17-4PH and 316L in that the relative sintered density tends to increase as the sintering temperature increases. Most available data from literature satisfied the JPMA standard for parts sintered at 1250 °C or above and are close to the data for the equivalent alloy formed by MIM and sintered at similar sintering temperatures, as similar powder size are used for both processes. Moreover, it is clearly observed that the parts produced using larger powder size (circular blue symbols) need to be sintered at a higher sintering temperature when compared to those from smaller sized powders (rectangular blue symbols) [78]. It is noted that although the sintering temperature of <1100 °C was used (to refine grain size), the relative sintered density can be more than 98%. This is attribution to the fine size was utilised.

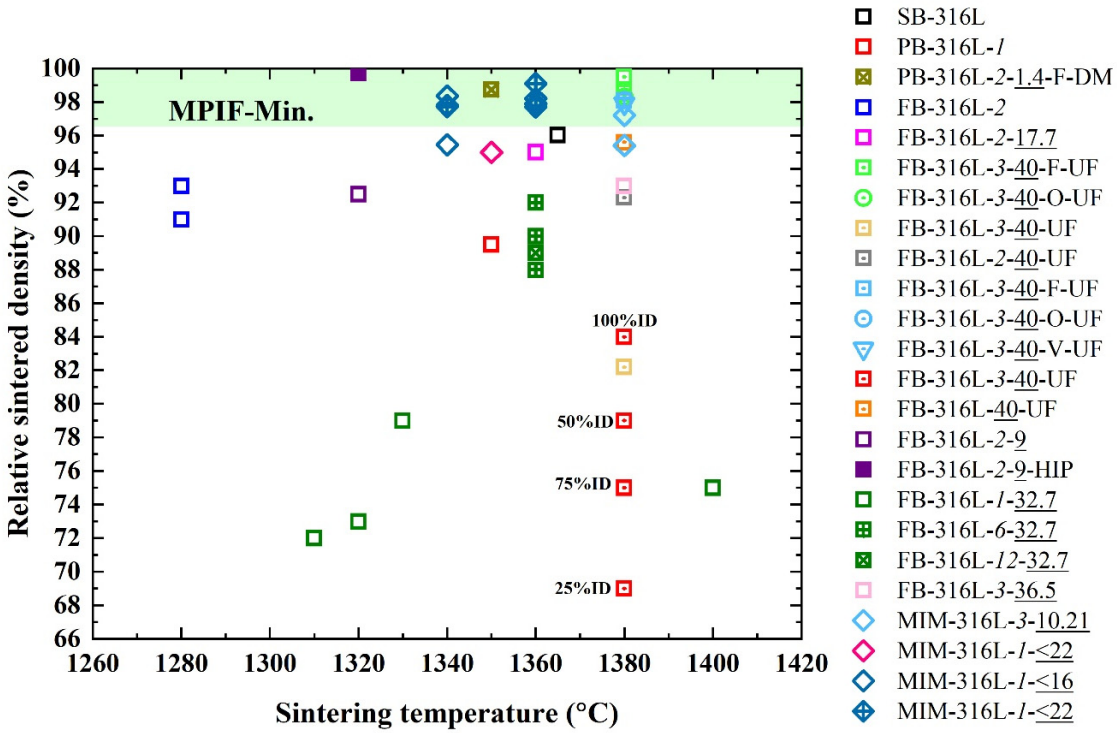

Figure 20. Sintering temperature vs. relative sintered density map of 316L stainless steel fabricated by metal MEX process with different conditions comparing with MPIF standard 35 for MIM materials. The Italic number represents sintering time (h) and the underlined number represents powder size (μm). F, O and V represent flat, on-edge and vertical printing orientations, respectively. ##%ID is the infill density. DM is utilising Desktop Metal system. Data from [9,41,45,52,53,56,57,66,68,70,72,75,81,98,108,159–161,169].

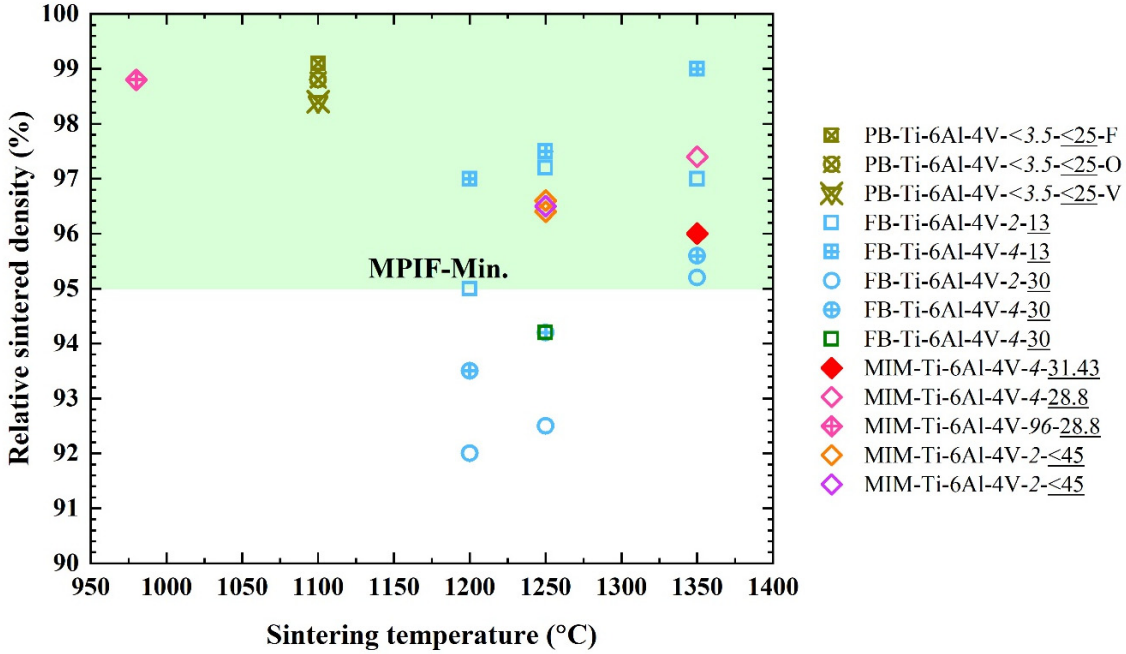

Figure 21. Sintering temperature vs. relative sintered density map of Ti-6Al-4V alloys fabricated by metal MEX process with different conditions comparing with MPIF standard 35 for MIM materials. The italic number represents sintering time (h) and the underlined number represents mean powder size (μm). Data from [78,79,109,163,164,170–172].

3.4. Tensile Properties Evaluation

The tensile properties from the literature of metal MEX, MIM and the corresponding MIM international standards are presented as strength vs. ductility maps for 17-4PH, 316L and Ti-6Al-4V in Figures 22–24, respectively. The data included in these figures are grouped and plotted from the selected data in Table 6. In Figure 22 [8,49,64,92,134,157,158,169], most available 17-4PH parts fabricated by the metal MEX process satisfy the MPIF minimum requirement for both as-sintered and as-aged conditions. However, the mechanical properties of the metal MEX parts are highly build-orientation dependent. Only the flat and on-edge built orientations (black, green and blue rectangular, and circular symbols) can meet the MPIF minimum requirement, while the vertical built orientation cannot (black, green and blue triangle symbols) [8,64]. This is due to the layer delamination effect in the vertical built orientation parts leading to premature failure [8]. Although the strength level of the metal MEX parts can be comparable to MIM, the elongation is slightly lower.

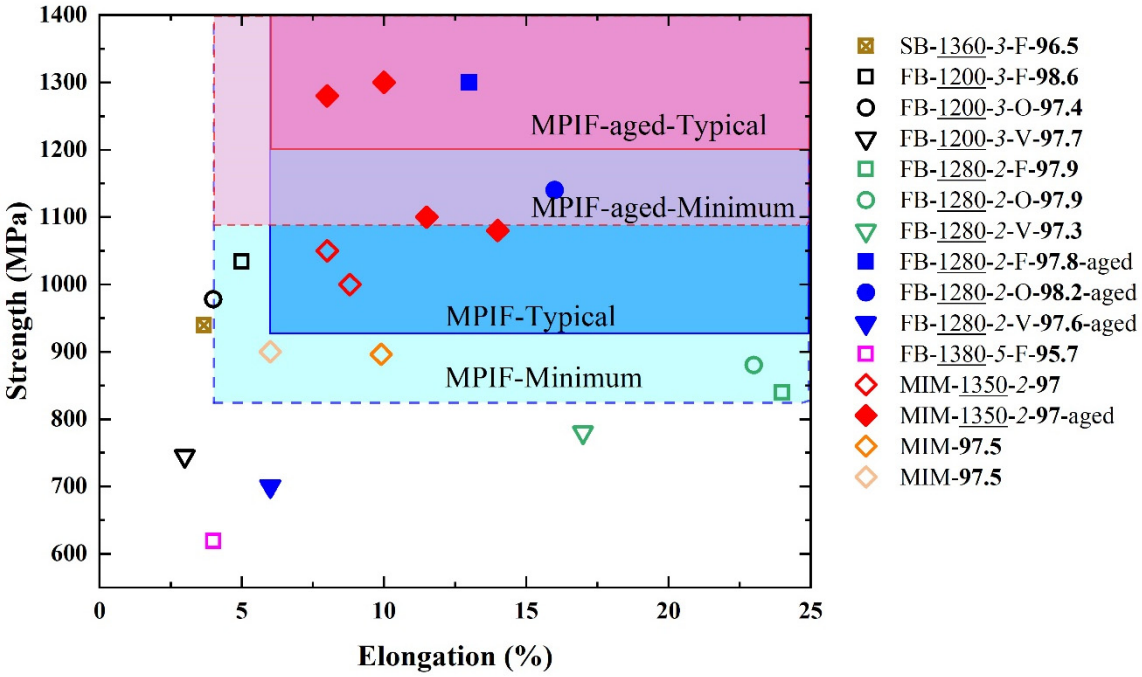

Figure 22. Stress vs. elongation map of 17-4PH stainless steel fabricated by the metal MEX process with different conditions comparing MPIF standard 35 for MIM materials. The underlined number represents sintering temperature (°C), the italic number represents sintering time (h), F, O and V represent flat, on-edge and vertical printing orientations, respectively, and the bold number represents relative sintered density (%). Data from [8,49,64,92,134,157,158,169].

For 316L stainless steel (Figure 23) [9,45,53,56,57,66,68,75,81,93,98,108,160,161,169,171,172], tensile properties of all available parts fabricated by the metal MEX process are lower than for MIM and most of them cannot satisfy the minimum requirement of the MPIF standard. Most tensile properties of MEX 316L vary in the range of 100 to 550 MPa for tensile strength and 3% to 57% for elongation to failure, which reflects the effect of the difference in processing parameters, such as printing and sintering, including the relative sintered density, as previously discussed, resulting in a significant difference in the tensile properties. This is more visible when focusing on the commercial Ultrafuse feedstock reported in many works (centre-dotted symbols). Although the feedstock is the same, the tensile properties are still subjected to wide scatter. The flat and on-edge built orientations provide higher tensile properties than those of the vertical built orientation similar to 17-4PH. Moritzer et al. [93] is the study that the tensile properties meets the MPIF standard. This is because many variables are suitably selected with the Ultrafuse filament, such

as nozzle size, printing speed, printing temperature, layer thickness and strand width, resulting in up to 99% as-printed density. In addition, the part printed by the commercial system, Desktop Metal, can meet the standard with very high elongation, reflecting the high quality of the process [108]. Moreover, for 316L parts that are treated by HIP, the tensile properties of both flat and vertical built orientations are comparable to those of MIM parts and can reach the MPIF standard [81]. This suggests that if the defects during printing can be minimised, metal MEX parts should have tensile properties comparable to those of MIM parts. Interestingly for Ti-6Al-4V alloy, the tensile properties of metal MEX parts meet the minimum requirement of the JPMA standard and are comparable or higher than those for the MIM alloy, as presented in Figure 24. The tensile strength is in the range of 875 to 96 MPa with 5% to 17% elongation. It is noted that the Ti-6Al-4V works were reported by the Singh et al. group [78,79], which has been working on MIM and has extensive knowledge of debinding and sintering. The availability of commercial filament is significantly increasing the accessibility of metal MEX, as in the case of 316L stainless steel. However, the use of non-optimised printing parameters, as well as a lack of debinding and sintering experience, can lead to variations in mechanical properties and can be detrimental to the acceptance to metal MEX when using commercial metal filaments or in-house metal filaments. This issue is being addressed by the availability of user-friendly closed metal MEX systems, which are supplied as complete sets of a printer, solvent debinding unit and controlled atmosphere sintering furnace. Users of such systems are not allowed to use any third-party feedstock and also are not allowed to vary debinding and sintering parameters.

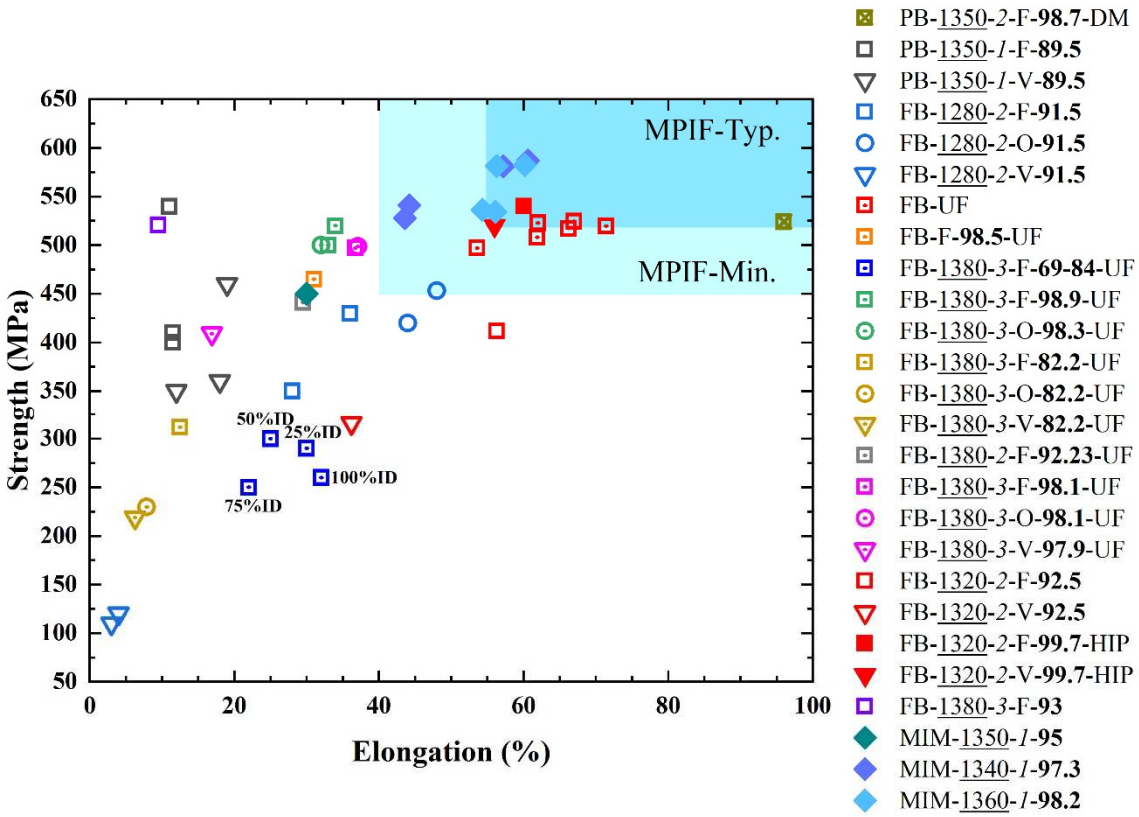

Figure 23. Stress vs. elongation map of 316L stainless steel fabricated by the metal MEX process with different conditions comparing with MPIF standard 35 for MIM materials. The underlined number represents sintering temperature (°C) and the italic number represents sintering time (h). F, O and V represent flat, on-edge and vertical printing orientations, respectively, and the bold number represents relative sintered density (%). ##% ID is the infill density. DM is utilising Desktop Metal system. Data from [9,45,53,56,57,66,68,75,81,93,98,108,160,161,169,171,172].

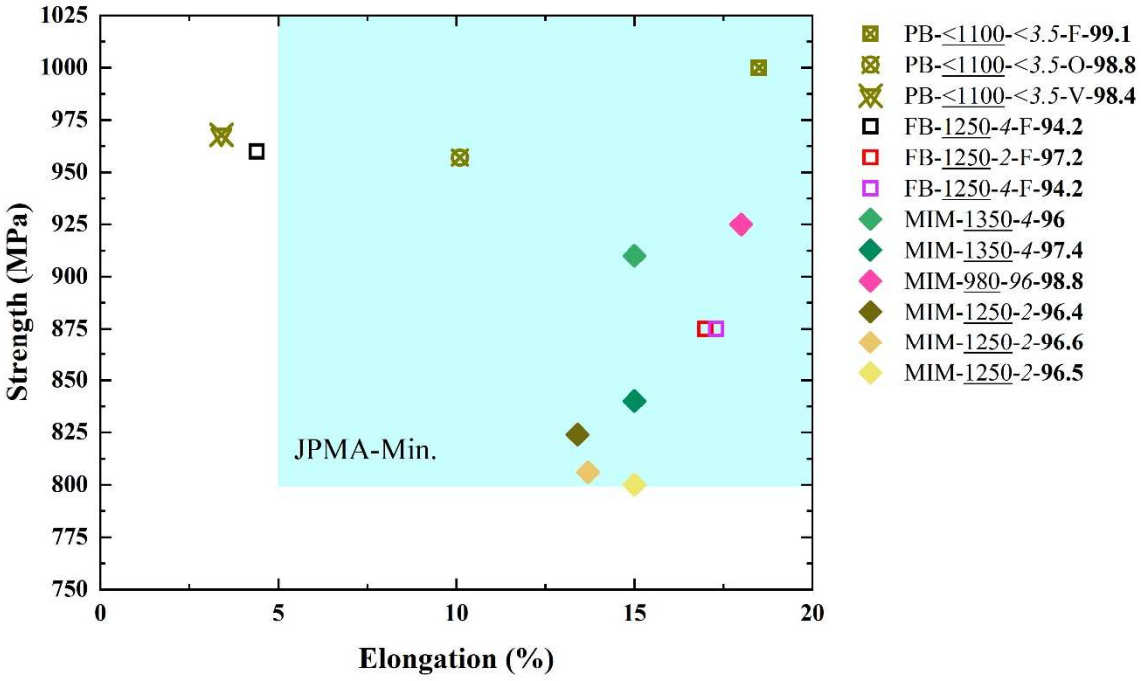

Figure 24. Stress vs. elongation map of Ti-6Al-4V alloy fabricated by the metal MEX process with different conditions comparing with JPMA standard for MIM materials. The underlined number is sintering temperature (°C), the italic number is sintering time (h) and the bold number is relative sintered density (%). Data from [78,79,109,163,164,170].

With respect to mechanical properties of the product, there is still room for improvement in the development of the metal MEX process. At present, MEX 17-4PH and Ti-6Al-4V parts can meet the minimum requirements of MIM standards and be comparable to MIM parts. However, most mechanical properties of MEX 316L cannot yet meet the minimum requirement of the MPIF standards.

Table 6. Effects of sintering temperature on shrinkage density and mechanical properties (ND is no detail; SP is spherical powder; IP is irregular powder) * The value was converted from density to relative sintered density for comparison.

Type of Printing	Alloys	Powder Characteristics	Solid Loading (Vol.%)	Sintering Process	Shrinkage (%)	Relative Sintered Density (%)	UTS, %El	Ref.
Screw-based	17-4PH	SP (2 to 10 μm)	93.5 wt.%	1360 °C, 3 h	14.2%	96.5	939.5 MPa, 3.67%	[92]
Screw-based	316L	ND	55	1365 °C	x-y = 14.49 z = 15.8	96.03	-	[41]
Screw-based	WC-Co	ND	ND	1150 °C and 1430 °C	x-y = 22.6 z = 23.4	-	-	[50]
Plunger-based	17-4PH	ND	79	1360 °C for 15 h (all cycle) in H_2 atmosphere	12.1	-	>320 HV	[36]
Plunger-based	316L	Sandvik Osprey	63	1350 °C for 1 h (HR 130 °C/h)	12.7	89.5 *	$H_{0.3}$ = 410 MPa, 11.5% $H_{0.4}$ = 400 MPa, 11.5% $H_{0.5}$ = 540 MPa, 11% $V_{0.3}$ = 350 MPa, 12% $V_{0.4}$ = 360 MPa, 18% $V_{0.5}$ = 460 MPa, 19%	[68]
Plunger-based	316L	SP (D_{50} = 1.4 μm)	-	1350 °C for 2 h in Ar (~1 °C/min)	-	98.73	524 MPa, 96%	[108]
Plunger-based	Ti-6Al-4V	D_{90} = 19 μm	66	No action	-	-	-	[61]
Plunger-based	Ti-6Al-4V	D_{90} = 19 μm	66	<1100 °C for <3.5 h	x = 12.13 y = 12.67 z = 12.21	F = 99.1 O = 98.8 V = 98.4	F = 1000 MPa, 18.5% O = 957 MPa, 10.1% V = 968 MPa, 3.4%	[109]
Filament-based	17-4PH	D_{50} = 3.97 μm	63	1200 °C for 3 h	15	F=98.6 O=97.4 V=97.7	F = 1034 MPa, 5% O = 978 MPa, 4% V = 745 MPa, 1%	[8]
Filament-based	17-4PH	D_{50} = 3.97 μm	63	1200 °C for 3 h	-	F = 98.1 O = 98.0 V = 96.5	-	[110]

Table 6. *Cont.*

Type of Printing	Alloys	Powder Characteristics	Solid Loading (Vol.%)	Sintering Process	Shrinkage (%)	Relative Sintered Density (%)	UTS, %El	Ref.
Filament-based	17-4PH	SP (22 μm (3.9 to 44 μm)) IP (10 μm (2.8 to 44 μm))	58	1260 °C in H_2 atmosphere (5 °C/min)	-	-	-	[34]
Filament-based	17-4PH	325 mesh size	60	1350 °C for 1 h in H_2 + N_2 atmosphere	-	92–95	-	[31,32]
Filament-based	17-4PH	10 μm	60	1280 °C for 2 h in Ar atmosphere	15.8	F = 97.9 O = 97.9 V = 97.3 F_{aged} = 97.8 O_{aged} = 98.2 V_{aged} = 97.6	F = 840 MPa, 24% O = 880 MPa, 23% V = 780 MPa, 17% F_{aged} = 1100 MPa, 13% O_{aged} = 1140 MPa, 16% V_{aged} = 700 MPa, 6%	[64]
Filament-based	17-4PH	D_{10} = 4.2, D_{50} = 12.3, D_{90} = 28.2 μm, Sandvik Osprey, Ltd.	55	1050 °C for 3 h [197]	-	-	-	[38,43]
Filament-based	17-4PH	SP, D_{50} = 12.3 μm	55	Sintering by OBE Ohnmacht & Baumgaertner GmbH & Co. KG, Ispringen, Germany	20	-	-	[44]
Filament-based	17-4PH	D_{10} = 4.2, D_{50} = 12.3, D_{90} = 28.2 μm, Sandvik Osprey, Ltd.	55	900 °C for 1.5 h and 1380 °C for 5 h (HR = 3 °C/h)	l = 20.3 w = 17.3 t = 15.2	95.7	619 MPa, 4%	[49]
Filament-based	316L	SP, D_{50} = 6.9 μm	50 and 55	1250 °C in H_2 atmosphere	-	89	-	[29]

Table 6. *Cont.*

Type of Printing	Alloys	Powder Characteristics	Solid Loading (Vol.%)	Sintering Process	Shrinkage (%)	Relative Sintered Density (%)	UTS, %El	Ref.
Filament-based	316L	ND	60	1280 °C for 2 h in Ar atmosphere	x-y = 14–15 z = 15–17	91–93	$F_{0.1}$ = 430 MPa, 36% $O_{0.1}$ = 453 MPa, 48% $V_{0.1}$ = 110 MPa, 3% $F_{0.3}$ = 350 MPa, 28% $O_{0.3}$ = 420 MPa, 44% $V_{0.3}$ = 120 MPa, 4%	[56]
Filament-based	316L	ND	55	ND	19.2	97.1 *	-	[35]
Filament-based	316L	Epson-Atmix Corporation	55	ND	15	-	-	[37]
Filament-based	316L	D_{10} = 6.1, D_{50} = 15.1 µm, D_{90} = 25.5, Carpenter Powder Technologies AB	55	1250 °C for 1.5 h in vacuum atmosphere (HR = 20 °C/min) [198]	19	-	-	[38]
Filament-based	316L	SP, D_{50} = 6.05 µm	55	No action	-	-	-	[39]
Filament-based	316L	SP, D_{50} = 8.6 µm	55	Sintering by OBE Ohnmacht & Baumgaertner GmbH & Co. KG	20	-	-	[44]
Filament-based	316L	30–50 µm	83 wt.%	1100 °C in Ar atmosphere (HR = 5 °C/min)	-	-	-	[48]
Filament-based	316L	Mean size = 17.7 µm, Carpenter technologies	55	1330–1360 °C for 2 h in vacuum (HR = 0.2 °C/min)	x-y = 16.3 z = 17.4	>95	Flexural = 1100 MPa, 6%	[52]
Filament-based	316L	30–50 µm	>88 wt.% (62 vol.%)	Sintering in H_2 or vacuum	x-y = 13–18 z = 15–23	98.5	465 MPa, 31% 60 HRB	[9]
Filament-based	316L	30–50 µm	>88 wt.% (62 vol.%)	1380 °C for 3 h in H_2 atmosphere (HR = 5 °C/min)	20	99.5–98.3 HD = 98.5 HL = 98.6 HP = 99.5 VD = 98.3	500–520 MPa, 32-34% HD = 500 MPa, 33% HL = 500 MPa, 33% HP = 520 MPa, 34% VD (O) = 500 MPa, 32%	[45]

Table 6. *Cont.*

Type of Printing	Alloys	Powder Characteristics	Solid Loading (Vol.%)	Sintering Process	Shrinkage (%)	Relative Sintered Density (%)	UTS, %El	Ref.
Filament-based	316L	30–50 µm	80 wt.% (62 vol.%)	1380 °C for 3 h in H_2 atmosphere (HR = 5 °C/min)	x-y = 15.8–18.4 z = 19.2–24.86	82.2	F = 311.8 MPa, 12.5% O = 229.6 MPa, 7.9% V = 218.7 MPa, 6.27%	[53]
Filament-based	316L	30–50 µm	88 wt.% (62 vol.%)	1380 °C for 2 h in Ar atmosphere	17	92.23	441 MPa, 29.5%	[57]
Filament-based	316L	30–50 µm	80 wt.% (62 vol.%)	1380 °C for 3 h in Ar atmosphere	x-y = 18 z = 21	F = 98.1 O = 98.1 V = 97.9	F = 497.1 MPa, 36.7% O = 498.6 MPa, 37.1% V = 409.1 MPa, 16.9%	[66]
Filament-based	316L	30–50 µm	88 wt.% (62 vol.%)	1050 °C for 0.75 h and 1380 °C	x-y = 17.5 z = 14.5	95.6	1.05×10^4 at 120 MPa 1.04×10^5 at 100 MPa $>10^6$ at 80 MPa	[70]
Filament-based	316L	30–50 µm	90 wt.%	ND	x-y = 16.4 z = 20	95	-	[73]
Filament-based	316L	30–50 µm	90 wt.%	ND	-	-	S1-25 = 519.6 MPa, 71.4% S2-25 = 517.3 MPa, 66.2% S3-25 = 508.0 MPa, 61.9% S1-40 = 497.0 MPa, 53.6% S2-40 = 522.9 MPa, 62% S3-40 = 524.6 MPa, 67%	[93]
Filament-based	316L	30–50 µm	90 wt.%	1380 °C for 3 h	25% IDx-y = 16.59 25% ID z = 17.35 50% IDx-y = 16.53 50% ID z = 17.8 75% IDx-y = 15.95 75% ID z = 15.19 100% IDx-y = 16.42 100% ID z = 17.26	25% ID = 69% 50% ID = 79% 75% ID = 75% 100% ID = 84%	25% ID = 290 MPa, 30% 50% ID = 300 MPa, 25% 75% ID = 250 MPa, 22% 100% ID = 260 MPa, 32%	[98]
Filament-based	316L	3–15 µm (AEM, China)	80 wt.%	1320 °C for 2 h (HR = 10 °C/min)	x-y = 16.4 z = 20	92.5 HIP 99.7	H = 412 MPa, 56.3% V = 316 MPa, 36.2% H_{HIP} = 540 MPa, 60% V_{HIP} = 520 MPa, 56%	[81]

Table 6. *Cont.*

Type of Printing	Alloys	Powder Characteristics	Solid Loading (Vol.%)	Sintering Process	Shrinkage (%)	Relative Sintered Density (%)	UTS, %El	Ref.
Filament-based	316L	0.872–76 µm (D_{50} = 32.7 µm)	83.5 wt.%	Sintering in Ar at 1310–1400 °C for 1, 6 and 12 h (HR = 3 °C/min)	-	72–92	160–370HV	[72]
Filament-based	316L	Nitrogen-atomised 20–53 µm, Hoganas (AM 316L)	65	1380 °C for 3 h (HR = 5 °C/min)	x-y = 11 z = 15	93	521 MPa, 9.5% 285.5 HV	[75]
Filament-based	Ti-6Al-4V	SP, D_{50} = 14.97 µm	55	No action	-	-	-	[39]
Filament-based	Ti-6Al-4V	SP, D_{50} = 14.97 µm	55	Sintering by OBE Ohnmacht & Baumgaertner GmbH & Co. KG	20	-	-	[44]
Filament-based	Ti-6Al-4V	Fine SP (D_{10} = 7, D_{50} = 13, D_{90} = 21 µm) Coarse SP (D_{10} = 2, D_{50} = 30, D_{90} = 44 µm)	59	No action	-	-	-	[59,76]
Filament-based	Ti-6Al-4V	D_{10} = 1.8, D_{50} = 6.7, D_{90} = 6.8 µm, American Elements	55-59	900, 1000, 1100, 1200, 1340 °C for 1.5 h in Ar atmosphere (2 L/min)	-	-	-	[63]
Filament-based	Ti-6Al-4V	Fine (F) SP, D_{50} = 13 µm Coarse (C) SP, D_{50} = 30 µm	59	1200, 1250 and 1350 °C for 2 and 4 h in vacuum		C1200, 2 h = 92 C1200, 4 h = 93.5 C1250, 2 h = 92.5 C1250, 4 h = 94.2 C1350, 2 h = 95.2 C1350, 4 h = 95.6 F1200, 2 h = 95 F1200, 4 h = 97 F1250, 2 h = 97.2 F1250, 4 h = 97.5 F1350, 2 h = 97 F1350, 4 h = 99	F = 960 MPa, 4.4% C = 875 MPa, 17%	[78]

Table 6. *Cont.*

Type of Printing	Alloys	Powder Characteristics	Solid Loading (Vol.%)	Sintering Process	Shrinkage (%)	Relative Sintered Density (%)	UTS, %El	Ref.
Filament-based	Ti-6Al-4V	Coarse SP, D_{50} = 30 μm	59	Sintering in partial vacuum of 150 millitorrs at 1250 °C for 4 h with Ar gas shield (HR = 3 °C/min)	x-y = 14.5 z = 15	94.2	875 MPa, 17.3%	[79]
Filament-based	CP-Ti	Mean size = 23.4 μm	55 vol.%	1350 °C for 5 h	15	93.16	300 MPa, 15%	[102]
Filament-based	WC-10% Co	ND	50	1150 °C and 1430 °C	x-y = 21 z = 22	-	-	[50]
Filament-based	WC-Co	ND	< 50	ND	-	-	-	[31,32]
Filament-based	High carbon-Fe	1.45–756 μm (D_{50} = 129 μm)	80 wt.%,	Sintering in Ar at 1310–1400 °C for 1, 6 and 12 h (HR = 3 °C/min)	-	72–92	160–370 HV	[72]
Filament-based	Cu	ND	ND	983 °C for 4 h (HR = 3.24 °C/min)	15.82	90	HRH 44.68	[51]

4. Special Processes to Improve the Properties

Many special processes have been investigated to improve the appearance, density and mechanical properties of polymer and metal MEX parts. In this section, examples of processes that hold promise for improvement of metal MEX parts will be discussed.

During printing, it is commonly known that there are the intrinsic voids between the deposited paths. Additional in situ systems, e.g., magnetic and ultrasonic, can be applied with the printing head or printing bed to successfully improve the quality of metal MEX parts [199] (magnetic) and polymer FDM parts [200] (ultrasonic). Squeezing by the rollers applied with the printing head is also demonstrated to improve the density and mechanical properties of polymer FDM parts [201]. However, the dimensions of the rolled parts needed to be carefully controlled. These systems can be possibly applicable to the meal MEX process to improve the as-printed quality, thus improving mechanical properties.

Metal MEX at the as-printed stage is significantly softer than after sintering. Hence, additional surface finishing of the as-printed parts, such as grinding, shot blasting or laser peening, can be applied to polish the surface [35]. The very high surface quality after sintering can also be achieved. Furthermore, HIP is still the most effective process to obtain fully dense parts; as discussed in the previous section, HIP can increase the relative density very close to 100% and provide tensile properties comparable to those of MIM and its standard [81]. It also reduces the build-orientation dependence of the metal MEX parts.

5. Current, Prospective Applications and Future Direction of Metal MEX Development

At this moment, metal MEX, which uses low-cost equipment, is a successful process to fabricate not only prototypes, but also end-user parts. Many parts in various applications have been developing. The rapid prototype of high wear resistance M2 steel can be fabricated with the in-house built filament, which can be an alternative for establishing a method for MIM part prototyping [96]. In addition, several end-user engineering parts have been commercially fabricated by the user-friendly closed metal MEX system [83,141]. The example of the end-user brake pedal 316L part is presented in Figure 25a. Metal MEX is also promising for the biomedical field [91,95], especially for patient-specific implants. Shaikh et al. [95] can produce Ti-6Al-4V MEX simple standard test pieces that can satisfy the MIM standard. However, when the required shape is complicated, e.g., the Ti-6Al-4V maxillofacial implant prototypes shown in Figure 25b to e, the density up to 94% can be achieved [95], which is below the MIM standard.

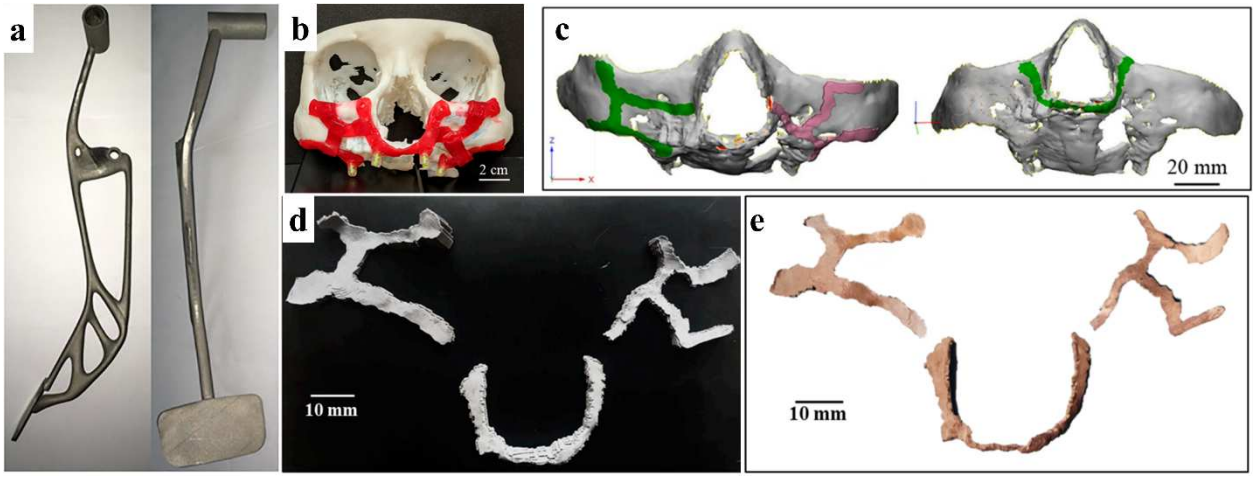

Figure 25. (**a**) 316L MEX brake pedal (Reprinted with permission from ref. [141]. Copyright 2021, Materials Today: Proceedings, Elsevier) and (**b**) maxillofacial implant design, (**c**) maxillofacial implants related to the design, (**d**) as-printed parts following the design and (**e**) as-sintered parts (adapted from [95]).

From the tensile property maps of the alloys, although most 316L MEX is still not comparable to MIM 316L and cannot satisfy the MIM standard, the 17-4PH and Ti-6Al-4V MEX are equivalent to their MIM counterparts. The process parameters still need to be systematically developed to increase the physical and mechanical properties of metal MEX parts to be at least comparable to those of MIM with high repeatability and reliability. This is achievable in the user-friendly commercial closed metal MEX systems, e.g., Studio+ System by Desktop Metal, Inc. and MetalX by Markforged, Inc. Hence, it should be possible for open systems using commercial feedstock suppliers or custom feedstocks and MIM furnaces.

From the research perspective, there is considerable scope in metal MEX to further investigate and develop in areas, such as printing, debinding and sintering with a variety of materials, especially Ti and Ni and their alloys. The printing strategies, including algorithms, also need to be explored to achieve denser parts. Moreover, although CP-Ti has been recently investigated [102], the mechanical properties can still be improved by minimising the impurity during debinding and sintering. In particular, the production of MEX parts in biocompatible and low elastic modulus beta-type Ti alloys, which are well known as challenging alloys for MIM fabrication due to the formation of brittle TiC [11,183,202], still needs to be further developed. Moreover, there is still a lack of investigations regarding the effects of adjustable processing parameters on the properties in more detail, e.g., the effect of infill percentage and infill pattern on the physical and mechanical properties, the printability of complex parts and the stability of complex parts during debinding and sintering. There have been limited studies on multi-material MEX. High carbon iron and 316L could be fabricated with homogeneous structure [72]. Only 91–92% relative sintered density was achieved with the complexity of shrinkage and distortion [72]. Further investigation to minimise the mismatch in shrinkage during co-printing and co-sintering will need to be carried out. Mechanical properties beyond tensile testing still need to be extensively studied, such as bending, compression and especially dynamic properties. The remaining porosity and the large grain size due to the nature of the printing and sintering processes are known to affect the dynamic properties [163,170,203–205]. A very limited number of studies have examined the fatigue properties of metal MEX. For example, there is only one study reporting the fatigue properties of 316L fabricated by FDM using Ultrafuse 316L feedstock [70]. Secondary processes, e.g., surface treatment by shot peening [171,182,206,207] or grain refinement [125,170,205,207], which improves both tensile and fatigue properties in MIM alloys, can also be promising for the metal MEX parts. In addition, the highly stable and precision screw-based printer still needs more development so that conventional MIM feedstock can be fed into an affordable printer. This will be useful to the MIM industry, which produces mass production parts, as metal MEX could create small quantity custom-made parts with short lead times using existing MIM feedstocks and MIM debinding and sintering equipment. In this case, no additional filament preparation is needed and parts can be readily produced without waiting for a metal mould for injection to be made. For the future perspective, the metal MEX process route will need to be covered by a suitable international standard after the technology becomes more mature and there are more manufacturers implementing metal MEX.

6. Summary

The metal MEX received much interest due to its low cost and simplicity, especially after the introduction of Ultrafuse 316L® filament by BASF SE, MetalX system by Markforged, Inc. and Studio+ System by Desktop Metal, Inc. Metal MEX is different from the MIM during the green part fabrication, which utilises layer-by-layer printing instead of injection. The most popular metal MEX printer is the filament-based type. The metal filament should have high flexural strength and stiffness so that the filament can be spooled. As a result, the solid loading is typically lower than MIM feedstock or polymer skin can be introduced to increase the filament flexibility. Special purposed and closed metal printers seem to provide more consistent and better printing quality. At the moment, metal MEX

can fabricate various types of alloys similar to MIM with close or comparable properties to MIM. Metal MEX is more attractive in terms of design freedom and does not require metal mould. Moreover, metal MEX has been used to fabricate end-use parts. However, from the present review, there are still large gaps for development in every step of this process. Many aspects, such as consistency, static, dynamic mechanical properties, geometry, precision and production rates, are still required to be improved and investigated.

Author Contributions: Conceptualisation, C.S. and A.M.; investigation, writing original draft, writing—review and editing, C.S.; funding acquisition, writing—review and editing and supervision, A.M. All authors have read and agreed to the published version of the manuscript.

Funding: This research was funded by the Newton Fund supported by the Royal Academy of Engineering through the Engineering X Transforming Systems through Partnership programme, UK, and the Office of National Higher Education Science Research and Innovation Policy Council (NXPO), Thailand, through the Program Management Unit for Competitiveness (PMUC), under the grant number: TSP2021\100052; and Taisei Kogyo (Thailand) Co., Ltd., under the grant number: P2150585.

Institutional Review Board Statement: Not applicable.

Informed Consent Statement: Not applicable.

Data Availability Statement: Not applicable.

Acknowledgments: The authors would like to sincerely thank John T.H. Pearce, Chiang Mai University, Thailand, for valuable discussions and proofreading.

Conflicts of Interest: The authors declare that they have no known competing financial interest or personal relationships that could have influenced the work reported in this paper.

References

1. *ISO/ASTM 52900:2021*; Standard Terminology for Additive Manufacturing—General Principles—Terminology. ASTM International: West Conshohocken, PA, USA, 2021.
2. Ngo, T.D.; Kashani, A.; Imbalzano, G.; Nguyen, K.T.Q.; Hui, D. Additive manufacturing (3D printing): A review of materials, methods, applications and challenges. *Compos. Part B Eng.* **2018**, *143*, 172–196. [CrossRef]
3. Frazier, W.E. Metal additive manufacturing: A review. *J. Mater. Eng. Perform.* **2014**, *23*, 1917–1928. [CrossRef]
4. Gonzalez-Gutierrez, J.; Cano, S.; Schuschnigg, S.; Kukla, C.; Sapkota, J.; Holzer, C. Additive manufacturing of metallic and ceramic components by the material extrusion of highly-filled polymers: A review and future perspectives. *Materials* **2018**, *11*, 840. [CrossRef] [PubMed]
5. Nurhudan, A.I.; Supriadi, S.; Whulanza, Y.; Saragih, A.S. Additive manufacturing of metallic based on extrusion process: A review. *J. Manuf. Processes* **2021**, *66*, 228–237. [CrossRef]
6. Suryawanshi, J.; Prashanth, K.G.; Ramamurty, U. Mechanical behavior of selective laser melted 316L stainless steel. *Mater. Sci. Eng. A* **2017**, *696*, 113–121. [CrossRef]
7. Murr, L.E.; Martinez, E.; Hernandez, J.; Collins, S.; Amato, K.N.; Gaytan, S.M.; Shindo, P.W. Microstructures and properties of 17-4 PH stainless steel fabricated by Selective Laser Melting. *J. Mater. Res. Technol.* **2012**, *1*, 167–177. [CrossRef]
8. Suwanpreecha, C.; Seensattayawong, P.; Vadhanakovint, V.; Manonukul, A. Influence of specimen layout on 17-4PH (AISI 630) alloys fabricated by low-cost additive manufacturing. *Metall. Mater. Trans. A* **2021**, *52*, 1999–2009. [CrossRef]
9. Gong, H.; Snelling, D.; Kardel, K.; Carrano, A. Comparison of stainless steel 316L parts made by FDM- and SLM-based additive manufacturing processes. *JOM* **2019**, *71*, 880–885. [CrossRef]
10. Barba, D.; Alabort, C.; Tang, Y.T.; Viscasillas, M.J.; Reed, R.C.; Alabort, E. On the size and orientation effect in additive manufactured Ti-6Al-4V. *Mater. Des.* **2020**, *186*, 108235. [CrossRef]
11. Suwanpreecha, C.; Alabort, E.; Tang, Y.T.; Panwisawas, C.; Reed, R.C.; Manonukul, A. A novel low-modulus titanium alloy for biomedical applications: A comparison between selective laser melting and metal injection moulding. *Mater. Sci. Eng. A* **2021**, *812*, 141081. [CrossRef]
12. Brandl, E.; Palm, F.; Michailov, V.; Viehweger, B.; Leyens, C. Mechanical properties of additive manufactured titanium (Ti–6Al–4V) blocks deposited by a solid-state laser and wire. *Mater. Des.* **2011**, *32*, 4665–4675. [CrossRef]
13. Song, B.; Kenel, C.; Dunand, D.C. 3D ink-extrusion printing and sintering of Ti, Ti-TiB and Ti-TiC microlattices. *Addit. Manuf.* **2020**, *35*, 101412. [CrossRef]
14. Trosch, T.; Strößner, J.; Völkl, R.; Glatzel, U. Microstructure and mechanical properties of selective laser melted Inconel 718 compared to forging and casting. *Mater. Lett.* **2016**, *164*, 428–431. [CrossRef]
15. Pleass, C.; Jothi, S. Influence of powder characteristics and additive manufacturing process parameters on the microstructure and mechanical behaviour of Inconel 625 fabricated by Selective Laser Melting. *Addit. Manuf.* **2018**, *24*, 419–431. [CrossRef]

16. Smith, D.H.; Bicknell, J.; Jorgensen, L.; Patterson, B.M.; Cordes, N.L.; Tsukrov, I.; Knezevic, M. Microstructure and mechanical behavior of direct metal laser sintered Inconel alloy 718. *Mater. Charact.* **2016**, *113*, 1–9. [CrossRef]
17. Pérez-Ruiz, J.D.; Marin, F.; Martínez, S.; Lamikiz, A.; Urbikain, G.; López de Lacalle, L.N. Stiffening near-net-shape functional parts of Inconel 718 LPBF considering material anisotropy and subsequent machining issues. *Mech. Syst. Signal Process.* **2022**, *168*, 108675. [CrossRef]
18. Pérez-Ruiz, J.D.; de Lacalle, L.N.L.; Urbikain, G.; Pereira, O.; Martínez, S.; Bris, J. On the relationship between cutting forces and anisotropy features in the milling of LPBF Inconel 718 for near net shape parts. *Int. J. Mach. Tools Manuf.* **2021**, *170*, 103801. [CrossRef]
19. Darvish, K.; Chen, Z.W.; Phan, M.A.L.; Pasang, T. Selective laser melting of Co-29Cr-6Mo alloy with laser power 180–360W: Cellular growth, intercellular spacing and the related thermal condition. *Mater. Charact.* **2018**, *135*, 183–191. [CrossRef]
20. Cloots, M.; Kunze, K.; Uggowitzer, P.J.; Wegener, K. Microstructural characteristics of the nickel-based alloy IN738LC and the cobalt-based alloy Mar-M509 produced by selective laser melting. *Mater. Sci. Eng. A* **2016**, *658*, 68–76. [CrossRef]
21. Glerum, J.A.; Kenel, C.; Sun, T.; Dunand, D.C. Synthesis of precipitation-strengthened Al-Sc, Al-Zr and Al-Sc-Zr alloys via selective laser melting of elemental powder blends. *Addit. Manuf.* **2020**, *36*, 101461. [CrossRef]
22. Griffiths, S.; Rossell, M.D.; Croteau, J.; Vo, N.Q.; Dunand, D.C.; Leinenbach, C. Effect of laser rescanning on the grain microstructure of a selective laser melted Al-Mg-Zr alloy. *Mater. Charact.* **2018**, *143*, 34–42. [CrossRef]
23. Olakanmi, E.O. Selective laser sintering/melting (SLS/SLM) of pure Al, Al–Mg, and Al–Si powders: Effect of processing conditions and powder properties. *J. Mater. Process. Technol.* **2013**, *213*, 1387–1405. [CrossRef]
24. Martin, J.H.; Yahata, B.D.; Hundley, J.M.; Mayer, J.A.; Schaedler, T.A.; Pollock, T.M. 3D printing of high-strength aluminium alloys. *Nature* **2017**, *549*, 365–369. [CrossRef]
25. Michi, R.A.; Plotkowski, A.; Shyam, A.; Dehoff, R.R.; Babu, S.S. Towards high-temperature applications of aluminium alloys enabled by additive manufacturing. *Int. Mater. Rev.* 2021; 1–48, ahead-of-print. [CrossRef]
26. Khorasani, M.; Ghasemi, A.; Rolfe, B.; Gibson, I. Additive manufacturing a powerful tool for the aerospace industry. *Rapid Prototyp. J.* **2021**, *28*, 87–100. [CrossRef]
27. Caffrey, T.; Wohlers, T.; Campbell, I. *Executive Summary of the Wohlers Report 2016*; Loughborough University: Loughborough, UK, 2016.
28. Buchanan, C.; Gardner, L. Metal 3D printing in construction: A review of methods, research, applications, opportunities and challenges. *Eng. Struct.* **2019**, *180*, 332–348. [CrossRef]
29. Riecker, S.; Clouse, J.; Studnitzky, T.; Andersen, O.; Kieback, B. Fused Deposition Modeling-Opportunities for Cheap Metal AM. In Proceedings of the World PM2016 Congress & Exhibition, Hamburg, Germany, 9–13 October 2016.
30. Rane, K.; Strano, M. A comprehensive review of extrusion-based additive manufacturing processes for rapid production of metallic and ceramic parts. *Adv. Manuf.* **2019**, *7*, 155–173. [CrossRef]
31. Agarwala, M.; van Weeren, R.; Bandyopadhyay, A.; Safari, A.; Danforth, S.; Priedeman, W. Filament feed materials for fused deposition processing of ceramics and metals. In *International Solid Freeform Fabrication Symposium Proceedings*; University of Texas: Austin, TX, USA, 1996.
32. Agarwala, M.; van Weeren, R.; Bandyopadhyay, A.; Whalen, P.; Safari, A.; Danforth, S. Fused deposition of ceramics and metals: An overview. In *International Solid Freeform Fabrication Symposium Proceedings*; University of Texas: Austin, TX, USA, 1996.
33. Wu, G.; Langrana, N.A.; Rangarajan, S.; McCuiston, R.; Sadanji, R.; Danforth, S.; Safari, A. Fabrication of metal components using FDMet: Fused deposition of metals. In *International Solid Freeform Fabrication Symposium Proceedings*; University of Texas: Austin, TX, USA, 1996.
34. Wu, G.; Langrana, N.A.; Sadanji, R.; Danforth, S. Solid freeform fabrication of metal components using fused deposition of metals. *Mater. Des.* **2002**, *23*, 97–105. [CrossRef]
35. Burkhardt, C.; Freigassner, P.; Weber, O.; Imgrund, P.; Hampel, S. Fused filament fabrication (FFF) of 316L green parts for the MIM process. In Proceedings of the World PM2016 Congress & Exhibition, Hamburg, Germany, 9–13 October 2016.
36. Giberti, H.; Strano, M.; Annoni, M. An innovative machine for Fused Deposition Modeling of metals and advanced ceramics. In *MATEC Web of Conferences*; EDP Sciences: Les Ulis, France, 2016; Volume 43, p. 03003.
37. Kukla, C.; Duretek, I.; Schuschnigg, S.; Gonzalez-Gutierrez, J.; Holzer, C. Properties for PIM feedstocks used in fused filament fabrication. In Proceedings of the World PM2016 Congress & Exhibition, Hamburg, Germany, 9–13 October 2016.
38. Gonzalez-Gutierrez, J.; Godec, D.; Kukla, C.; Schlauf, T.; Burkhardt, C.; Holzer, C. Shaping, debinding and sintering of steel components via fused filament fabrication. In Proceedings of the 16th International Scientific Conference on Production Engineering CIM 2017, Zadar, Croatia, 8–10 June 2017.
39. Kukla, C.; Gonzalez-Gutierrez, J.; Cano, S.; Hampel, S.; Burkhardt, C.; Moritz, T.; Holzer, C. Fused filament fabricaton (FFF) of PIM feedstocks. In Proceedings of the VI Congreso Nacional de Pulvimetalurgia y I Congreso Iberoamericano de Conference, Ciudad Real, Spain, 7–9 June 2017.
40. Kukla, C.; Gonzalez-Gutierrez, J.; Duretek, I.; Schuschnigg, S.; Holzer, C. Effect of particle size on the properties of highly-filled polymers for fused filament fabrication. In *AIP Conference Proceedings*; AIP Publishing: New York, NY, USA, 2017; Volume 1914, p. 190006.
41. Lieberwirth, C.; Harder, A.; Seitz, H. Extrusion based additive manufacturing of metal parts. *J. Mech. Eng. Autom.* **2017**, *7*, 79–83.

42. Condruz, M.R.; Paraschiv, A.; Puscasu, C. Heat treatment influence on hardness and microstructure of ADAM manufactured 17-4 PH. *Turbo* **2018**, *5*, 39–45.
43. Gonzalez-Gutierez, J.; Godec, D.; Guráň, R.; Spoerk, M.; Kukla, C.; Holzer, C. 3D printing conditions determination for feedstock used in fused filament fabrication (FFF) of 17-4PH stainless steel parts. *Metalurgija* **2018**, *57*, 117–120.
44. Gonzalez-Gutierrez, J.; Cano, S.; Schuschnigg, S.; Holzer, C.; Kukla, C. Highly-filled polymers for fused filament fabrication. *Leobener Kunstst.-Kolloqu.* **2018**, *27*, 93–104.
45. Damon, J.; Dietrich, S.; Gorantla, S.; Popp, U.; Okolo, B.; Schulze, V. Process porosity and mechanical performance of fused filament fabricated 316L stainless steel. *Rapid Prototyp. J.* **2019**, *25*, 1319–1327. [CrossRef]
46. Fidan, S.T.I. Dimensional analysis of metal powder infused filament-low cost metal 3D printing. In *International Solid Freeform Fabrication Symposium Proceedings*; University of Texas: Austin, TX, USA, 2019; pp. 533–541. [CrossRef]
47. Galati, M.; Minetola, P. Analysis of density, roughness, and accuracy of the Atomic Diffusion Additive Manufacturing (ADAM) process for metal parts. *Materials* **2019**, *12*, 4122. [CrossRef] [PubMed]
48. Gante Lokesha Renukaradhya, K. Metal Filament 3D Printing of SS316L: Focusing on the Printing Process. Master Thesis's, KTH Royal Institute of Technology, Stockholm, Sweden, 2019.
49. Gonzalez-Gutierrez, J.; Arbeiter, F.; Schlauf, T.; Kukla, C.; Holzer, C. Tensile properties of sintered 17-4PH stainless steel fabricated by material extrusion additive manufacturing. *Mater. Lett.* **2019**, *248*, 165–168. [CrossRef]
50. Lengauer, W.; Duretek, I.; Fürst, M.; Schwarz, V.; Gonzalez-Gutierrez, J.; Schuschnigg, S.; Kukla, C.; Kitzmantel, M.; Neubauer, E.; Lieberwirth, C.; et al. Fabrication and properties of extrusion-based 3D-printed hardmetal and cermet components. *Int. J. Refract. Met. Hard Mater.* **2019**, *82*, 141–149. [CrossRef]
51. Terry, S.M. *Innovating the Fused Filament Fabrication Process Metal Powder Polylactic Acid Printing*; Tennessee Technological University: Cookeville, TN, USA, 2019.
52. Thompson, Y.; Gonzalez-Gutierrez, J.; Kukla, C.; Felfer, P. Fused filament fabrication, debinding and sintering as a low cost additive manufacturing method of 316L stainless steel. *Addit. Manuf.* **2019**, *30*, 100861. [CrossRef]
53. Ait-Mansour, I.; Kretzschmar, N.; Chekurov, S.; Salmi, M.; Rech, J. Design-dependent shrinkage compensation modeling and mechanical property targeting of metal FFF. *Prog. Addit. Manuf.* **2020**, *5*, 51–57. [CrossRef]
54. Godec, D.; Cano, S.; Holzer, C.; Gonzalez-Gutierrez, J. Optimization of the 3D printing parameters for tensile properties of specimens produced by Fused Filament Fabrication of 17-4PH stainless steel. *Materials* **2020**, *13*, 774. [CrossRef]
55. Korotchenko, A.; Khilkov, D.; Tverskoy, M.; Khilkova, A. Use of additive technologies for metal injection molding. *Eng. Solid Mech.* **2020**, *8*, 143–150. [CrossRef]
56. Kurose, T.; Abe, Y.; Santos, M.V.; Kanaya, Y.; Ishigami, A.; Tanaka, S.; Ito, H. Influence of the layer directions on the properties of 316L stainless steel parts fabricated through fused deposition of metals. *Materials* **2020**, *13*, 2493. [CrossRef] [PubMed]
57. Liu, B.; Wang, Y.; Lin, Z.; Zhang, T. Creating metal parts by Fused Deposition Modeling and sintering. *Mater. Lett.* **2020**, *263*, 127252. [CrossRef]
58. Niemelä, M. Experimental Strength Tests with Metal X. Bachelor's Thesis, Vaasan Ammattikorkeakoulu University of Applied Sciences, Vaasa, Finland, 2020.
59. Singh, P.; Balla, V.K.; Tofangchi, A.; Atre, S.V.; Kate, K.H. Printability studies of Ti-6Al-4V by metal fused filament fabrication (MF3). *Int. J. Refract. Met. Hard Mater.* **2020**, *91*, 105249. [CrossRef]
60. Singh, P.; Shaikh, Q.; Balla, V.K.; Atre, S.V.; Kate, K.H. Estimating powder-polymer material properties used in design for Metal Fused Filament Fabrication (DfMF 3). *JOM* **2020**, *72*, 485–495. [CrossRef]
61. Waalkes, L.; Längerich, J.; Holbe, F.; Emmelmann, C. Feasibility study on piston-based feedstock fabrication with Ti-6Al-4 V metal injection molding feedstock. *Addit. Manuf.* **2020**, *35*, 101207. [CrossRef]
62. Watson, A.; Belding, J.; Ellis, B.D. *Characterization of 17-4 PH Processed via Bound Metal Deposition (BMD)*; Springer International Publishing: Cham, Switzerland, 2020. [CrossRef]
63. Zhang, Y.; Bai, S.; Riede, M.; Garratt, E.; Roch, A. A comprehensive study on Fused Filament Fabrication of Ti-6Al-4V structures. *Addit. Manuf.* **2020**, *34*, 101256. [CrossRef]
64. Abe, Y.; Kurose, T.; Santos, M.V.; Kanaya, Y.; Ishigami, A.; Tanaka, S.; Ito, H. Effect of layer directions on internal structures and tensile properties of 17-4PH stainless steel parts fabricated by Fused Deposition of metals. *Materials* **2021**, *14*, 243. [CrossRef]
65. Alkindi, T.; Alyammahi, M.; Susantyoko, R.A.; Atatreh, S. The effect of varying specimens' printing angles to the bed surface on the tensile strength of 3D-printed 17-4PH stainless-steels via metal FFF additive manufacturing. *MRS Commun.* **2021**, *11*, 1–7. [CrossRef]
66. Caminero, M.Á.; Romero, A.; Chacón, J.M.; Núñez, P.J.; García-Plaza, E.; Rodríguez, G.P. Additive manufacturing of 316L stainless-steel structures using fused filament fabrication technology: Mechanical and geometric properties. *Rapid Prototyp. J.* **2021**, *27*, 583–591. [CrossRef]
67. Costa, J.; Sequeiros, E.; Vieira, M.T.; Vieira, M. Additive manufacturing: Material extrusion of metallic parts. *J. Eng.* **2021**, *7*, 53–69. [CrossRef]
68. Hassan, W.; Farid, M.A.; Tosi, A.; Rane, K.; Strano, M. The effect of printing parameters on sintered properties of extrusion-based additively manufactured stainless steel 316L parts. *Int. J. Adv. Manuf. Technol.* **2021**, *114*, 3057–3067. [CrossRef]
69. Henry, T.C.; Morales, M.A.; Cole, D.P.; Shumeyko, C.M.; Riddick, J.C. Mechanical behavior of 17-4 PH stainless steel processed by atomic diffusion additive manufacturing. *Int. J. Adv. Manuf. Technol.* **2021**, *114*, 2103–2114. [CrossRef]

70. Jiang, D.; Ning, F. Additive manufacturing of 316L stainless steel by a printing-debinding-sintering method: Effects of microstructure on fatigue property. *J. Manuf. Sci. Eng.* **2021**, *143*, 1–30. [CrossRef]
71. Mashekov, S.; Bazarbay, B.; Zhankeldi, A.; Mashekova, A. Development of technological basis of 3D printing with highly filled metal-poly-dimensional compositions for manufacture of metal products of complex shape. *Metalurgija* **2021**, *60*, 355–358.
72. Mousapour, M.; Salmi, M.; Klemettinen, L.; Partanen, J. Feasibility study of producing multi-metal parts by Fused Filament Fabrication (FFF) technique. *J. Manuf. Processes* **2021**, *67*, 438–446. [CrossRef]
73. Quarto, M.; Carminati, M.; D'Urso, G. Density and shrinkage evaluation of AISI 316L parts printed via FDM process. *Mater. Manuf. Processes* **2021**, *36*, 1535–1543. [CrossRef]
74. Quarto, M.; Carminati, M.; D'Urso, G.; Giardini, C.; Maccarini, G. Processability of metal-filament through polymer FDM machine. In Proceedings of the 24th International Conference on Material Forming, Liège, Belgium, 14–16 April 2021. [CrossRef]
75. Sadaf, M.; Bragaglia, M.; Nanni, F. A simple route for additive manufacturing of 316L stainless steel via Fused Filament Fabrication. *J. Manuf. Processes* **2021**, *67*, 141–150. [CrossRef]
76. Shaikh, M.Q.; Lavertu, P.-Y.; Kate, K.H.; Atre, S.V. Process sensitivity and significant parameters investigation in Metal Fused Filament Fabrication of Ti-6Al-4V. *J. Mater. Eng. Perform.* **2021**, *30*, 5118–5134. [CrossRef]
77. Shaikh, M.Q.; Singh, P.; Kate, K.H.; Freese, M.; Atre, S.V. Finite element-based simulation of metal fused filament fabrication process: Distortion Prediction and Experimental Verification. *J. Mater. Eng. Perform.* **2021**, *30*, 5135–5149. [CrossRef]
78. Singh, P.; Balla, V.K.; Atre, S.V.; German, R.M.; Kate, K.H. Factors affecting properties of Ti-6Al-4V alloy additive manufactured by metal fused filament fabrication. *Powder Technol.* **2021**, *386*, 9–19. [CrossRef]
79. Singh, P.; Balla, V.K.; Gokce, A.; Atre, S.V.; Kate, K.H. Additive manufacturing of Ti-6Al-4V alloy by metal fused filament fabrication (MF3): Producing parts comparable to that of metal injection molding. *Prog. Addit. Manuf.* **2021**, *6*, 593–606. [CrossRef]
80. Tosto, C.; Tirillò, J.; Sarasini, F.; Cicala, G. Hybrid metal/polymer filaments for Fused Filament Fabrication (FFF) to print metal parts. *Appl. Sci.* **2021**, *11*, 1444. [CrossRef]
81. Wang, Y.; Zhang, L.; Li, X.; Yan, Z. On hot isostatic pressing sintering of fused filament fabricated 316L stainless steel—Evaluation of microstructure, porosity, and tensile properties. *Mater. Lett.* **2021**, *296*, 129854. [CrossRef]
82. Lu, Z.; Ayeni, O.I.; Yang, X.; Park, H.-Y.; Jung, Y.-G.; Zhang, J. Microstructure and phase analysis of 3d-printed components using bronze metal filament. *J. Mater. Eng. Perform.* **2020**, *29*, 1650–1656. [CrossRef]
83. Cerejo, F.; Gatões, D.; Vieira, M. Optimization of metallic powder filaments for additive manufacturing extrusion (MEX). *Int. J. Adv. Manuf. Technol.* **2021**, *115*, 2449–2464. [CrossRef]
84. Singh, G.; Missiaen, J.-M.; Bouvard, D.; Chaix, J.-M. Copper extrusion 3D printing using metal injection moulding feedstock: Analysis of process parameters for green density and surface roughness optimization. *Addit. Manuf.* **2021**, *38*, 101778. [CrossRef]
85. Singh, G.; Missiaen, J.-M.; Bouvard, D.; Chaix, J.-M. Copper additive manufacturing using MIM feedstock: Adjustment of printing, debinding, and sintering parameters for processing dense and defectless parts. *Int. J. Adv. Manuf. Technol.* **2021**, *115*, 449–462. [CrossRef]
86. Santos, C.; Gatões, D.; Cerejo, F.; Vieira, T. Influence of metallic powder characteristics on extruded feedstock performance for indirect additive manufacturing. *Materials* **2021**, *14*, 7136. [CrossRef]
87. Vishwanath, A.; Rane, K.; Schaper, J.; Strano, M.; Casati, R. Rapid production of AZ91 Mg alloy by extrusion based additive manufacturing process. *Powder Metall.* **2021**, *64*, 370–377. [CrossRef]
88. Shaikh, M.Q.; Graziosi, S.; Atre, S.V. Supportless printing of lattice structures by metal fused filament fabrication (MF3) of Ti-6Al-4V: Design and analysis. *Rapid Prototyp. J.* **2021**, *27*, 1408–1422. [CrossRef]
89. Terry, S.; Fidan, I.; Tantawi, K. Preliminary investigation into metal-material extrusion. *Prog. Addit. Manuf.* **2021**, *6*, 133–141. [CrossRef]
90. Gonzalez-Gutierrez, J.; Cano, S.; Ecker, J.V.; Kitzmantel, M.; Arbeiter, F.; Kukla, C.; Holzer, C. Bending properties of lightweight copper specimens with different infill patterns produced by material extrusion additive manufacturing, solvent debinding and sintering. *Appl. Sci.* **2021**, *11*, 7262. [CrossRef]
91. Gloeckle, C.; Konkol, T.; Jacobs, O.; Limberg, W.; Ebel, T.; Handge, U.A. Processing of highly filled polymer–metal feedstocks for fused filament fabrication and the production of metallic implants. *Materials* **2020**, *13*, 4413. [CrossRef] [PubMed]
92. Singh, G.; Missiaen, J.-M.; Bouvard, D.; Chaix, J.-M. Additive manufacturing of 17-4 PH steel using metal injection moulding feedstock: Analysis of 3D extrusion printing, debinding and sintering. *Addit. Manuf.* **2021**, *47*, 102287. [CrossRef]
93. Moritzer, E.; Elsner, C.L.; Schumacher, C. Investigation of metal-polymer composites manufactured by fused deposition modeling with regard to process parameters. *Polym. Compos.* **2021**, *42*, 6065–6079. [CrossRef]
94. Hasib, A.G.; Niauzorau, S.; Xu, W.; Niverty, S.; Kublik, N.; Williams, J.; Chawla, N.; Song, K.; Azeredo, B. Rheology scaling of spherical metal powders dispersed in thermoplastics and its correlation to the extrudability of filaments for 3D printing. *Addit. Manuf.* **2021**, *41*, 101967. [CrossRef]
95. Shaikh, M.Q.; Nath, S.D.; Akilan, A.A.; Khanjar, S.; Balla, V.K.; Grant, G.T.; Atre, S.V. Investigation of patient-specific maxillofacial implant prototype development by metal fused filament fabrication (MF3) of Ti-6Al-4V. *Dent. J.* **2021**, *9*, 109. [CrossRef]
96. Naranjo, J.A.; Berges, C.; Gallego, A.; Herranz, G. A novel printable high-speed steel filament: Towards the solution for wear-resistant customized tools by AM alternative. *J. Mater. Res. Technol.* **2021**, *11*, 1534–1547. [CrossRef]
97. Dietrich, S.; Englert, L.; Pinter, P. Non-destructive characterization of additively manufactured components using X-Ray micro-computed tomography. In *Solid Freeform Fabrication Symposium*; University of Texas: Austin, TX, USA, 2018.

98. Rosnitschek, T.; Seefeldt, A.; Alber-Laukant, B.; Neumeyer, T.; Altstädt, V.; Tremmel, S. Correlations of geometry and infill degree of extrusion additively manufactured 316L stainless steel components. *Materials* **2021**, *14*, 5173. [CrossRef] [PubMed]
99. Mohammadizadeh, M.; Lu, H.; Fidan, I.; Tantawi, K.; Gupta, A.; Hasanov, S.; Zhang, Z.; Alifui-Segbaya, F.; Rennie, A. Mechanical and thermal analyses of Metal-PLA components fabricated by metal material extrusion. *Inventions* **2020**, *5*, 44. [CrossRef]
100. Jimbo, K.; Tateno, T. Shape contraction in sintering of 3D objects fabricated via metal material extrusion in additive manufacturing. *Int. J. Autom. Technol.* **2019**, *13*, 354–360. [CrossRef]
101. Zhang, Z.; Femi-Oyetoro, J.; Fidan, I.; Ismail, M.; Allen, M. Prediction of dimensional changes of low-cost metal material extrusion fabricated parts using machine learning techniques. *Metals* **2021**, *11*, 690. [CrossRef]
102. Thompson, Y.; Polzer, M.; Gonzalez-Gutierrez, J.; Kasian, O.; Heckl, J.P.; Dalbauer, V.; Kukla, C.; Felfer, P.J. Fused filament fabrication-based additive manufacturing of commercially pure titanium. *Adv. Eng. Mater.* **2021**, *23*, 2100380. [CrossRef]
103. Roshchupkin, S.; Golovin, V.; Kolesov, A.; Tarakhovskiy, A.Y. Extruder for the production of metal-polymer filament for additive technologies. In *IOP Conference Series: Materials Science and Engineering*; IOP Publishing: Bristol, UK, 2020; pp. 1–6.
104. Obadimu, S.O.; McLaughlin, J.; Kourousis, K.I. Immersion ultrasonic testing of artificially induced defects in fused filament fabricated steel 316L. *3D Print. Addit. Manuf.* 2021; in press. [CrossRef]
105. Kan, X.; Yang, D.; Zhao, Z.; Sun, J. 316L FFF binder development and debinding optimization. *Mater. Res. Express* **2021**, *8*, 116515. [CrossRef]
106. Wagner, M.A.; Hadian, A.; Sebastian, T.; Clemens, F.; Schweizer, T.; Rodriguez-Arbaizar, M.; Carreño-Morelli, E.; Spolenak, R. Fused filament fabrication of stainless steel structures—From binder development to sintered properties. *Addit. Manuf.* **2021**, *49*, 102472. [CrossRef]
107. Jiang, D.; Ning, F. Anisotropic deformation of 316 L stainless steel overhang structures built by material extrusion based additive manufacturing. *Addit. Manuf.* **2021**, *50*, 102545. [CrossRef]
108. Santamaria, R.; Salasi, M.; Bakhtiari, S.; Leadbeater, G.; Iannuzzi, M.; Quadir, M.Z. Microstructure and mechanical behaviour of 316L stainless steel produced using sinter-based extrusion additive manufacturing. *J. Mater. Sci.* **2022**, 1–17. [CrossRef]
109. Waalkes, L.; Längerich, J.; Imgrund, P.; Emmelmann, C. Piston-based material extrusion of Ti-6Al-4V feedstock for complementary use in metal injection molding. *Materials* **2022**, *15*, 351. [CrossRef]
110. Suwanpreecha, C.; Manonukul, A. On the build orientation effect in as-printed and as-sintered bending properties of 17-4PH alloy fabricated by metal fused filament fabrication. *Rapid Prototyp. J.* 2022; in press. [CrossRef]
111. Ramazani, H.; Kami, A. Metal FDM, a new extrusion-based additive manufacturing technology for manufacturing of metallic parts: A review. *Prog. Addit. Manuf.* **2022**, 1–18. [CrossRef]
112. Hong, S.; Sanchez, C.; Du, H.; Kim, N. Fabrication of 3D printed metal structures by use of high-viscosity cu paste and a screw extruder. *J. Electron. Mater.* **2015**, *44*, 836–841. [CrossRef]
113. Yan, X.; Hao, L.; Xiong, W.; Tang, D. Research on influencing factors and its optimization of metal powder injection molding without mold via an innovative 3D printing method. *RSC Adv.* **2017**, *7*, 55232–55239. [CrossRef]
114. Rane, K.; Di Landro, L.; Strano, M. Processability of SS316L powder—Binder mixtures for vertical extrusion and deposition on table tests. *Powder Technol.* **2019**, *345*, 553–562. [CrossRef]
115. Rane, K.; Castelli, K.; Strano, M. Rapid surface quality assessment of green 3D printed metal-binder parts. *J. Manuf. Processes* **2019**, *38*, 290–297. [CrossRef]
116. Ren, L.; Zhou, X.; Song, Z.; Zhao, C.; Liu, Q.; Xue, J.; Li, X. Process parameter optimization of extrusion-based 3D metal printing utilizing PW–LDPE–SA binder system. *Materials* **2017**, *10*, 305. [CrossRef] [PubMed]
117. Annoni, M.; Giberti, H.; Strano, M. Feasibility study of an extrusion-based direct metal additive manufacturing technique. *Procedia Manuf.* **2016**, *5*, 916–927. [CrossRef]
118. Rane, K.; Barriere, T.; Strano, M. Role of elongational viscosity of feedstock in extrusion-based additive manufacturing of powder-binder mixtures. *Int. J. Adv. Manuf. Technol.* **2020**, *107*, 4389–4402. [CrossRef]
119. Mishra, A.A.; Momin, A.; Strano, M.; Rane, K. Implementation of viscosity and density models for improved numerical analysis of melt flow dynamics in the nozzle during extrusion-based additive manufacturing. *Prog. Addit. Manuf.* **2022**, *7*, 41–54. [CrossRef]
120. Giberti, H.; Sbaglia, L.; Silvestri, M. Mechatronic design for an extrusion-based additive manufacturing machine. *Machines* **2017**, *5*, 29. [CrossRef]
121. Parenti, P.; Cataldo, S.; Annoni, M. Shape deposition manufacturing of 316L parts via feedstock extrusion and green-state milling. *Manuf. Lett.* **2018**, *18*, 6–11. [CrossRef]
122. Rosnitschek, T.; Glamsch, J.; Lange, C.; Alber-Laukant, B.; Rieg, F. An automated open-source approach for debinding simulation in metal extrusion additive manufacturing. *Designs* **2021**, *5*, 2. [CrossRef]
123. Strano, M.; Rane, K.; Farid, M.A.; Mussi, V.; Zaragoza, V.; Monno, M. Extrusion-based additive manufacturing of forming and molding tools. *Int. J. Adv. Manuf. Technol.* **2021**, *117*, 2059–2071. [CrossRef]
124. Ebel, T. 17—Metal injection molding (MIM) of titanium and titanium alloys. In *Handbook of Metal Injection Molding*; Heaney, D.F., Ed.; Woodhead Publishing: Sawston, UK, 2012; pp. 415–445. [CrossRef]
125. Miura, H.; Osada, T.; Itoh, Y. Metal Injection Molding (Mim) Processing. In *Advances in Metallic Biomaterials: Processing and Applications*; Niinomi, M., Narushima, T., Nakai, M., Eds.; Springer: Berlin/Heidelberg, Germany, 2015; pp. 27–56. [CrossRef]
126. Ebel, T. Titanium MIM for manufacturing of medical implants and devices. In *Titanium in Medical and Dental Applications*; Elsevier: Amsterdam, The Netherlands, 2018; pp. 531–551. [CrossRef]

127. European Powder Metallurgy Association. *Metal Injection Moulding: A Manufacturing Process for Precision Engineering Components*; European Powder Metallurgy Association: Shrewsbury, UK, 2013.
128. Popescu, D.; Zapciu, A.; Amza, C.; Baciu, F.; Marinescu, R. FDM process parameters influence over the mechanical properties of polymer specimens: A review. *Polym. Test.* **2018**, *69*, 157–166. [CrossRef]
129. Samykano, M.; Selvamani, S.K.; Kadirgama, K.; Ngui, W.K.; Kanagaraj, G.; Sudhakar, K. Mechanical property of FDM printed ABS: Influence of printing parameters. *Int. J. Adv. Manuf. Technol.* **2019**, *102*, 2779–2796. [CrossRef]
130. Wickramasinghe, S.; Do, T.; Tran, P. FDM-based 3D printing of polymer and associated composite: A review on mechanical properties, defects and treatments. *Polymers* **2020**, *12*, 1529. [CrossRef]
131. Turner, B.N.; Strong, R.; Gold, S.A. A review of melt extrusion additive manufacturing processes: I. Process design and modeling. *Rapid Prototyp. J.* **2014**, *20*, 192–204. [CrossRef]
132. Valkenaers, H.; Vogeler, F.; Ferraris, E.; Voet, A.; Kruth, J.-P. A novel approach to additive manufacturing: Screw extrusion 3D-printing. In *Proceedings of the 10th International Conference on Multi-Material Micro Manufacture, San Sebastian, Spain, 8–10 October 2013*; Research Publishing: Singapore. [CrossRef]
133. Bellini, A.; Shor, L.; Guceri, S.I. New developments in fused deposition modeling of ceramics. *Rapid Prototyp. J.* **2005**, *11*, 214–220. [CrossRef]
134. Manonukul, A.; Likityingwara, W.; Rungkiatnawin, P.; Muenya, N.; Amoranan, S.; Kittinantapol, W.; Surapunt, S. Study of recycled and virgin compounded metal injection moulded feedstock for stainless steel 630. *J. Solid Mech. Mater. Eng.* **2007**, *1*, 411–420. [CrossRef]
135. AIM3D GmbH Edelstahl. The Next Generation of 3D Printing Advantages of the ExAM 255. Available online: https://www.aim3d.de/en/products/exam-255/ (accessed on 27 October 2021).
136. Pollen, Ltd. PAM: Pellet Additive Manufacturing. Available online: https://www.pollen.am/ (accessed on 27 October 2021).
137. Direct3D, Pellet Extrusion. Available online: https://www.direct3d.it/ (accessed on 27 October 2021).
138. Desktop Metal, Inc. Prototype and Mass Produce with the Same Alloys. Available online: https://www.desktopmetal.com/products/materials/ (accessed on 27 October 2021).
139. Masood, S.H. Advances in fused deposition modeling. In *Comprehensive Materials Processing*; Elsevier: Amsterdam, The Netherlands, 2014; pp. 69–91.
140. Markforged, Inc. Complete Metal Solution. Available online: https://markforged.com/metal-x/ (accessed on 27 October 2021).
141. Sargini, M.I.M.; Masood, S.H.; Palanisamy, S.; Jayamani, E.; Kapoor, A. Additive manufacturing of an automotive brake pedal by metal fused deposition modelling. *Mater. Today Proc.* **2021**, *45*, 4601–4605. [CrossRef]
142. Chen, C.L.; Thomson, R.C. Study on thermal expansion of intermetallics in multicomponent Al–Si alloys by high temperature X-ray diffraction. *Intermetallics* **2010**, *18*, 1750–1757. [CrossRef]
143. Turner, B.N.; Gold, S.A. A review of melt extrusion additive manufacturing processes: II. Materials, dimensional accuracy, and surface roughness. *Rapid Prototyp. J.* **2015**, *21*, 250–261. [CrossRef]
144. Ian Gibson, I.G. *Additive Manufacturing Technologies 3D Printing, Rapid Prototyping, and Direct Digital Manufacturing*; Springer: Berlin/Heidelberg, Germany, 2015.
145. Hwang, S.; Reyes, E.I.; Moon, K.-S.; Rumpf, R.C.; Kim, N.S. Thermo-mechanical characterization of metal/polymer composite filaments and printing parameter study for fused deposition modeling in the 3D printing process. *J. Electron. Mater.* **2015**, *44*, 771–777. [CrossRef]
146. The Virtual Foundry, Printing Pure Metal with FILAMET™. Available online: https://www.thevirtualfoundry.com/help (accessed on 27 October 2021).
147. Ultrafuse 316L. Available online: https://www.ultrafusefff.com/product-category/metal/ultrafuse-316l/ (accessed on 27 October 2021).
148. 316L Metal Filament 1.75 mm. Available online: https://www.anycubic.com/products/316l-metal-filament-1-75mm316L (accessed on 27 October 2021).
149. Heaney, D.F. *Handbook of Metal Injection Molding*; Woodhead Publishing: Sawston, UK, 2018.
150. Ultrafuse 17-4PH. Available online: https://www.basf.com/global/de/who-we-are/organization/group-companies/BASF_New-Business-GmbH/news/press-releases/2020/201202-launch-ultrafuse.html (accessed on 3 February 2022).
151. Dehghan-Manshadi, A.; StJohn, D.; Dargusch, M.; Chen, Y.; Sun, J.F.; Qian, M. Metal injection moulding of non-spherical titanium powders: Processing, microstructure and mechanical properties. *J. Manuf. Processes* **2018**, *31*, 416–423. [CrossRef]
152. Wu, Y.; Wang, R.; Kwon, Y.-S.; Park, S.-J.; German, R.M. Injection molding of HDH titanium powder. *Int. J. Powder Metall.* **2006**, *42*, 59–66.
153. Dehghan-Manshadi, A.; Bermingham, M.J.; Dargusch, M.S.; StJohn, D.H.; Qian, M. Metal injection moulding of titanium and titanium alloys: Challenges and recent development. *Powder Technol.* **2017**, *319*, 289–301. [CrossRef]
154. Gulsoy, H.O.; Pazarlioglu, S.; Gulsoy, N.; Gundede, B.; Mutlu, O. Effect of Zr, Nb and Ti addition on injection molded 316L stainless steel for bio-applications: Mechanical, electrochemical and biocompatibility properties. *J. Mech. Behav. Biomed. Mater.* **2015**, *51*, 215–224. [CrossRef]
155. Bidaux, J.-E.; Pasquier, R.; Rodriguez-Arbaizar, M.; Girard, H.; Carreño-Morelli, E. Low elastic modulus Ti–17Nb processed by powder injection moulding and post-sintering heat treatments. *Powder Metall.* **2014**, *57*, 320–323. [CrossRef]

156. Davies, P.; Dunstan, R.; Howells, R.; Hayward, A. Development of master alloy powders, including nickel-based superalloys, for Metal Injection Molding (MIM). *Adv. Powder Metall. Part. Mater.* 2003.
157. Wu, M.-W.; Huang, Z.-K.; Tseng, C.-F.; Hwang, K.-S. Microstructures, mechanical properties, and fracture behaviors of metal-injection molded 17-4PH stainless steel. *Met. Mater. Int.* **2015**, *21*, 531–537. [CrossRef]
158. Manonukul, A.; Songkuea, S.; Moonchaleanporn, P.; Tange, M. Effect of weld line positions on the tensile deformation of two-component metal injection moulding. *Int. J. Miner. Metall. Mater.* **2017**, *24*, 1384–1393. [CrossRef]
159. Huang, M.-S.; Hsu, H.-C. Effect of backbone polymer on properties of 316L stainless steel MIM compact. *J. Mater. Processing Technol.* **2009**, *209*, 5527–5535. [CrossRef]
160. Castro, L.; Merino, S.; Levenfeld, B.; Várez, A.; Torralba, J.M. Mechanical properties and pitting corrosion behaviour of 316L stainless steel parts obtained by a modified metal injection moulding process. *J. Mater. Processing Technol.* **2003**, *143–144*, 397–402. [CrossRef]
161. Heaney, D.; Mueller, T.; Davies, P. Mechanical properties of metal injection moulded 316L stainless steel using both prealloy and master alloy techniques. *Powder Metall.* **2004**, *47*, 367–373. [CrossRef]
162. Froes, F.H. Getting better: Big boost for titanium MIM prospects. *Met. Powder Rep.* **2006**, *61*, 20–23. [CrossRef]
163. Kudo, K.; Shinagawa, K.; Miura, H. Effect of $\alpha + \beta$ region sintering on the mechanical properties of injection molded Ti-6Al-4V compacts. *Mech. Eng. J.* **2018**, *5*, 17-00686. [CrossRef]
164. Ferri, O.M.; Ebel, T.; Bormann, R. Influence of surface quality and porosity on fatigue behaviour of Ti–6Al–4V components processed by MIM. *Mater. Sci. Eng. A* **2010**, *527*, 1800–1805. [CrossRef]
165. German, R. Progress in titanium metal powder injection molding. *Materials* **2013**, *6*, 3641–3662. [CrossRef]
166. Wen, G.; Cao, P.; Gabbitas, B.; Zhang, D.; Edmonds, N. Development and design of binder systems for titanium metal injection molding: An overview. *Metall. Mater. Trans. A* **2013**, *44*, 1530–1547. [CrossRef]
167. Rhee, B.O.; Chung, C. Effects of the binder characteristics on binder separation in powder injection molding. In Proceedings of the 1992 Powder Injection Molding Symposium, San Francisco, CA, USA, 21–26 June 1992.
168. McNulty, T.F.; Mohammadi, F.; Bandyopadhyay, A.; Shanefield, D.; Danforth, S.; Safari, A. Development of a binder formulation for fused deposition of ceramics. *Rapid Prototyp. J.* **1998**, *4*, 144–150. [CrossRef]
169. MPIF. *Material Standards for Metal Injection Molded Parts*; Metal Powder Industries Federation: Princeton, NJ, USA, 2016.
170. Choe, J.; Osada, T.; Kudo, K.; Tsumori, F.; Miura, H. Effect of minor boron addition on the fatigue strength and high temperature properties of injection molded Ti-6Al-4V compacts. *J. Jpn. Soc. Powder Powder Metall.* **2016**, *63*, 451–456. [CrossRef]
171. Ferri, O.M.; Ebel, T.; Bormann, R. High cycle fatigue behaviour of Ti–6Al–4V fabricated by metal injection moulding technology. *Mater. Sci. Eng. A* **2009**, *504*, 107–113. [CrossRef]
172. *ISO 22068:2012*; Sintered-Metal Injection-Molded Materials—Specification. Japan Powder Metallurgy Association: Tokyo, Japan, 2014.
173. Spoerk, M.; Gonzalez-Gutierrez, J.; Sapkota, J.; Schuschnigg, S.; Holzer, C. Effect of the printing bed temperature on the adhesion of parts produced by fused filament fabrication. *Plast. Rubber Compos.* **2018**, *47*, 17–24. [CrossRef]
174. Singh, K. Experimental study to prevent the warping of 3D models in fused deposition modeling. *Int. J. Plast. Technol.* **2018**, *22*, 177–184. [CrossRef]
175. Kankawa, Y. Metal Powder Injection Moldable Composition, and Injection Molding and Sintering Method Using Such Composition. U.S. Patent US6051184A, 2000.
176. Kankawa, Y. Single step MIM system with polyacetal binder without debinding process. In Proceedings of the World PM2000 Congress & Exhibition, Kyoto, Japan, 12–16 November 2000; pp. 270–273.
177. Desktop Metal, Inc. Studio System™ 2. Available online: https://www.desktopmetal.com/products/studio (accessed on 27 October 2021).
178. Hamidi, M.F.F.A.; Harun, W.S.W.; Samykano, M.; Ghani, S.A.C.; Ghazalli, Z.; Ahmad, F.; Sulong, A.B. A review of biocompatible metal injection moulding process parameters for biomedical applications. *Mater. Sci. Eng. C* **2017**, *78*, 1263–1276. [CrossRef]
179. Shibo, G.; Xuanhui, Q.; Xinbo, H.; Ting, Z.; Bohua, D. Powder injection molding of Ti–6Al–4V alloy. *J. Mater. Process. Technol.* **2006**, *173*, 310–314. [CrossRef]
180. Chalermkarnnon, P.; Manonukul, A.; Muenya, N.; Nakayama, H.; Fujiwara, M. Minimizing contamination in commercial mass production of metal injection molded pure titanium. *J. Manuf. Sci. Eng.* **2011**, *133*, 054502. [CrossRef]
181. Bootchai, S.; Taweejun, N.; Manonukul, A.; Kanchanomai, C. Metal injection molded titanium: Mechanical properties of debinded powder and sintered metal. *J. Mater. Eng. Perform.* **2020**, *29*, 4559–4568. [CrossRef]
182. Ebel, T.; Blawert, C.; Willumeit, R.; Luthringer, B.J.; Ferri, O.M.; Feyerabend, F. Ti–6Al–4V–0.5 B—A modified alloy for implants produced by metal injection molding. *Adv. Eng. Mater.* **2011**, *13*, B440–B453. [CrossRef]
183. Kafkas, F.; Ebel, T. Metallurgical and mechanical properties of Ti–24Nb–4Zr–8Sn alloy fabricated by metal injection molding. *J. Alloys Compd.* **2014**, *617*, 359–366. [CrossRef]
184. German, R.M. *Sintering Theory and Practice*; John Wiley & Sons: New York, NY, USA, 1996.
185. Annicchiarico, D.; Alcock, J.R. Review of factors that affect shrinkage of molded part in injection molding. *Mater. Manuf. Processes* **2014**, *29*, 662–682. [CrossRef]
186. Itoh, Y.; Miura, H.; Uematsu, T.; Sato, K.; Niinomi, M.; Ozawa, T. The commercial potential of MIM titanium alloy. *Met. Powder Rep.* **2009**, *64*, 17–20. [CrossRef]

187. Zhao, D.-p.; Ebel, T.; Yan, M.; Qian, M. Trace carbon in biomedical beta-titanium alloys: Recent progress. *JOM* **2015**, *67*, 2236–2243. [CrossRef]
188. Yan, M.; Qian, M.; Kong, C.; Dargusch, M.S. Impacts of trace carbon on the microstructure of as-sintered biomedical Ti–15Mo alloy and reassessment of the maximum carbon limit. *Acta Biomater.* **2014**, *10*, 1014–1023. [CrossRef]
189. Xu, P.; Pyczak, F.; Yan, M.; Limberg, W.; Willumeit-Römer, R.; Ebel, T. Tensile toughening of powder-injection-molded β Ti-Nb-Zr biomaterials by adjusting TiC particle distribution from aligned to dispersed pattern. *Appl. Mater. Today* **2020**, *19*, 100630. [CrossRef]
190. Schaper, J.G.; Wolff, M.; Wiese, B.; Ebel, T.; Willumeit-Römer, R. Powder metal injection moulding and heat treatment of AZ81 Mg alloy. *J. Mater. Process. Technol.* **2019**, *267*, 241–246. [CrossRef]
191. Olevsky, E.; German, R. Effect of gravity on dimensional change during sintering—I. Shrinkage anisotropy. *Acta Mater.* **2000**, *48*, 1153–1166. [CrossRef]
192. Li, Y.; Li, L.; Khalil, K.A. Effect of powder loading on metal injection molding stainless steels. *J. Mater. Process. Technol.* **2007**, *183*, 432–439. [CrossRef]
193. Akhoundi, B.; Behravesh, A.H. Effect of filling pattern on the tensile and flexural mechanical properties of FDM 3D printed products. *Exp. Mech.* **2019**, *59*, 883–897. [CrossRef]
194. Pandzic, A.; Hodzic, D.; Milovanovic, A. Effect of infill type and density on tensile properties of PLA material for FDM process. *Ann. DAAAM Proc.* **2019**, 545–554. [CrossRef]
195. Srinivasan, R.; Nirmal Kumar, K.; Jenish Ibrahim, A.; Anandu, K.V.; Gurudhevan, R. Impact of fused deposition process parameter (infill pattern) on the strength of PETG part. *Mater. Today Proc.* **2020**, *27*, 1801–1805. [CrossRef]
196. Kato, K. Effect of sintering temperature on density and tensile properties of titanium compacts by matal injection molding. *J. Jpn. Soc. Powder Powder Metall.* **1999**, *46*, 865–869. [CrossRef]
197. Ye, H.; Liu, X.Y.; Hong, H. Sintering of 17-4PH stainless steel feedstock for metal injection molding. *Mater. Lett.* **2008**, *62*, 3334–3336. [CrossRef]
198. Ji, C.H.; Loh, N.H.; Khor, K.A.; Tor, S.B. Sintering study of 316L stainless steel metal injection molding parts using Taguchi method: Final density. *Mater. Sci. Eng. A* **2001**, *311*, 74–82. [CrossRef]
199. Wang, J.; Xie, H.; Wang, L.; Senthil, T.; Wang, R.; Zheng, Y.; Wu, L. Anti-gravitational 3D printing of polycaprolactone-bonded Nd-Fe-B based on fused deposition modeling. *J. Alloys Compd.* **2017**, *715*, 146–153. [CrossRef]
200. Maidin, S.; Muhamad, M.; Pei, E. Feasibility study of ultrasonic frequency application on fdm to improve parts surface finish. *J. Teknol.* **2015**, *77*, 27–35. [CrossRef]
201. Ravoori, D.; Salvi, S.; Prajapati, H.; Qasaimeh, M.; Adnan, A.; Jain, A. Void reduction in fused filament fabrication (FFF) through in situ nozzle-integrated compression rolling of deposited filaments. *Virtual Phys. Prototyp.* **2021**, *16*, 1–14. [CrossRef]
202. Luo, X.; Ebel, T.; Pyczak, F.; Limberg, W.; Lin, Y. Carbide evolution and its potential reduction methods in Ti-22Nb based alloys prepared by metal injection moulding. *Mater. Lett.* **2017**, *193*, 295–298. [CrossRef]
203. Kudo, K.; Ishimitsu, H.; Choe, J.; Osada, T.; Miura, H.; Shinagawa, K. Effect of grain size on the fatigue properties of injection moulded Ti-6Al-4V compacts. In Proceedings of the World PM2016 Congress & Exhibition, Hamburg, Germany, 9–13 October 2016.
204. Kudo, K.; Ishimitsu, H.; Osada, T.; Tsumori, F.; Miura, H. Static and dynamic fracture characteristics of the MIM Ti-6Al-4V alloy compacts using fine powder. *J. Jpn. Soc. Powder Powder Metall.* **2016**, *63*, 445–450. [CrossRef]
205. Ferri, O.M.; Ebel, T.; Bormann, R. The influence of a small boron addition on the microstructure and mechanical properties of Ti-6Al-4V fabricated by metal injection moulding. *Adv. Eng. Mater.* **2011**, *13*, 436–447. [CrossRef]
206. Vieira Muterlle, P. *Microstructural and Mechanical Properties of Co and Ti Alloys for Biomedical Applications Produced by Metal Injection Molding (MIM)*; University of Trento: Trento, Italy, 2010.
207. Suwanpreecha, C.; Manonukul, A. Review: Fatigue properties of Ti-6Al-4V alloys fabricated by metal injection moulding. *SIAM Sci. Innov. Adv. Mater.* **2021**, *1*, 64005.